Precision quantum state preparation and readout of solid state spins.

Von der Fakultät 8 Mathematik und Physik der Universität Stuttgart zur Erlangung der Würde eines Doktors der Naturwissenschaften (Dr. rer. nat.) genehmigte Abhandlung

Vorgelegt von

Gerald Waldherr

aus Überlingen

Hauptberichter:	Prof. Dr. J. Wrachtrup
Mitberichter:	Prof. Dr. T. Pfau

Tag der mündlichen Prüfung: 20.03.2014

3. Physikalisches Institut der Universität Stuttgart

2014

Ehrenwörtliche Erklärung

Ich erkläre, dass ich diese Arbeit selbständig verfaßt und keine anderen als die angegebenen Quellen und Hilfsmittel benutzt habe.

Stuttgart, 04.03.2014 *Gerald Waldherr*

Contents

Zusammenfassung

Einleitung Das Interesse an Quanteninformationsverarbeitung entstand 1985 durch den Vorschlag von D. Deutsch, dass ein Computer, der die Gesetzte der Quantenmechanik ausnutzt, Berechnungsprobleme deutlich effizienter lösen kann als ein klassischer Computer [1]. Diese Idee wurden von anderen Wissenschaftlern weiter untersucht, und in der Tat wurden solche Quanten-Algorithmen gefunden für aktuelle Berechnungsprobleme wie die Primfaktorzerlegung oder Suchalgorithmen [2, 3]. Zusätzlich wurde von Feynman gezeigt, dass man einen Quantencomputer auch dazu benutzen kann, andere Quantensysteme effizient zu simulieren [4], was mit einem klassischen Computer nicht möglich ist. Ein weiteres interessantes, vielversprechendes Gebiet der Quanteninformationsverarbeitung ist Quantenkryptographie [5], bei der fundamentale Sicherheit auf Basis physikalischer Prinzipien gewährleistet wird. Dies ist möglich durch die probabilistische Natur der Quantenmechanik, und die Tatsache, dass ein Quantenzustand durch eine Messung beeinflusst wird. Die große Herausforderung der experimentellen Umsetzung von Quanteninformationsverarbeitung ist die Notwendigkeit, ein hohes Maß an Kontrolle über miteinander wechselwirkende, physikalische Systeme zu haben, die gleichzeitig möglichst keine Wechselwirkung mit ihrer unkontrollierten Umgebung haben. Vielversprechende Systeme sind Photonen [6, 7], Atome in Fallen [8], Kernspinresonanz [9], Supraleiter [10], Quantenpunkte [11], und Spin-Defekte in Festkörpern [12], wie das in dieser Arbeit untersuchte Stickstoff-Fehlstellen-Zentrum in Diamant [13, 14].

Das Stickstoff-Fehlstellen-Zentrum (NV, englisch für nitrogen-vacancy) in Diamant kann man sich wie ein Atom bzw. Molekül vorstellen, das im Diamantkristall gefangen ist. Durch seine hohe Fluoreszenz und seine optische Stabilität kann es beispielsweise als Einzelphotonenquelle benutzt werden [15, 16], oder in Nanodiamanten als Fluoreszenzmarkierung für die Biologie [17, 18, 19]. In einem reinen Diamant stellt der Elektronenspin des negativ geladenen NV, NV^-, ein 'quantenmechanisches Spielzeugsystem' dar, dessen Zustand gemessen und manipuliert werden kann um die quantenmechanische Dynamik einen einzelnen Systems zu beobachten. Die besonderen Eigenschaften von NV^- sind seine spinabhängige Photophysik, wodurch rein optische Initialisierung und Messung des Spinzustands möglich sind [20], kombiniert mit langen Spinkohärenzzeiten im elektronischen Grundzustand [21, 22]. Zudem sind beim NV viele Experimente selbst bei Raumtemperatur möglich, da wegen der hohen Debeye-Temperatur von Diamant verhältnismäßig lange Spinlebenszeiten erreicht werden. Die Energie der Elektronenspinzustände ist abhängig von verschiedenen äußeren Parametern, sodass das NV als Quantensensor mit Nanometer-Auflösung eingesetzt werden kann, z.B. für Magnetfelder

[23, 24, 25, 26, 27], externe Spins [28, 29, 30], elektrische Felder [31] und Temperatur [32, 33, 34, 35]. In dieser Arbeit untersuchen wir die mögliche Anwendbarkeit von NV^- zur Quanteninformationsverarbeitung [13], wobei alle Experimente bei Raumtemperatur durchgeführt werden.

Im speziellen konzentrieren wir uns darauf, Kernspins in der Nähe des NV als weitere Quantenressource zu nutzen, um die Einsatzmöglichkeiten eines einzelnen NV zu erweitern. Durch die Ausnutzung von Kernspins ergibt sich ein natürtliches, heterogenes Spinsystem. Der Vorteil eines solchen heterogenen Systems ist, dass die verschiedenen guten Eigenschaften der Teilsysteme miteinander kombiniert werden können. Im Falle eines Spinssystems aus Elektronen und Kernspins werden die Elektronenspins mit ihrer verhältnismäßig starken Wechselwirkung zur Quantenkontrolle genutzt, und die Kernspins als langlebiger Informationsspeicher. Die kohärente Kontrolle von einzelnen ^{13}C Kernspins mit dem NV wurde erstmals in [36] demonstriert. Das Potential von Kernspins als Quantenregister wurde weiter untersucht, indem die Speicherung von Informationen auf Kernspins und deren Kohärenzeigenschaften analysiert wurden [37, 38, 39], und Verschränkung von zwei ^{13}C Kernspin demonstriert wurde [40]. Eine wichtige Grundlage für diese Arbeit ist die nicht-destruktive Messung von Kernspins mit dem NV [41, 42]. Dadurch kann eine direkte Zustandsmessung des Kernspins auf Basis von wiederholten Messung gemacht werden, d.h. das Messergebnis ist quantisiert mit den Eigenzuständen des Systems, das sich nach der Messung im zum Messergebnis zugehörenden Eigenzustand befinden (eine sogenannte projektive, "single-shot" Messung).

Aufbau dieser Arbeit In Kapitel 1 werden die physikalischen Grundlagen dieser Arbeit bezüglich Quanteninformationsverarbeitung, theoretische und praktische Aspekte des NV, und die Dynamik von Spins zusammengefasst. In Kapitel 2 untersuchen wir die Photoionisation des NV. Dort zeigen wir den Nachweis von NV^0 über NMR, eine Methode zur Ladungszustandmessung in Echtzeit, mit der die Dynamik des Ladungszustands untersucht wird, und die Verbesserung der Elekronenspinpolarisation. In Kapitel 3 sind verschiedene Grundlagenexperimente auf Basis der direkten Zustandsmessung des ^{14}N Kernspin gezeigt. Dabei handelt es sich um die Verletzung einer zeitlichen Bellschen Ungleichung, die Unterscheidung von nicht-orthogonalen Zuständen, und ein Algorithmus zur Quantenphasenabschätzung für Magnetfeldmessung mit hohem Dynamikumfang. In Kapitel 4 wird ein Quantenregister aus dem Elektronenspin und drei Kernspins vorgestellt. Gezeigt werden die Initialisierung und das Auslesen der Kernspins, die Implementierung von nicht-lokalen Kernspinoperationen mit optimaler Kontrolle und schließlich Quantenfehlerkorrektur. Zudem untersuchen wir die Nutzbarkeit von sogenannten schwach gekoppelten Kernspins.

Ergebnisse dieser Arbeit Nach der Entwicklung der direkten Zustandsmessung des ^{14}N Kerspins [41] wurde entdeckt, dass Kernspinoperationen nur mit $\approx 70\,\%$ Wahrscheinlichkeit funktionieren. Der Grund für dieses Verhalten ist photoinduzierte Ionisation

und Rekombination des NV, wie wir in dieser Arbeit herausgefunden haben. Dadurch befindet sich das NV nach dem optischen Initialisieren und Auslesen in einem gemischten Zustand von NV^- und NV^0, wobei maximal 75 % der Population in NV^- ist. Dabei kann nur der negative Ladungszustand NV^- sinnvoll genutzt werden, da die Spinkohärenzzeiten in NV^0 zu kurz sind. Diese Ionisations- und Rekombinationsdynamik haben wir untersucht in Abhängigkeit der Wellenlänge und Leistung des anregenden Lasers. Dadurch wurde ein wichtiger Beitrag zum Verständnis des NV geliefert. Mit der richtigen Wahl der Laserwellenlänge und Leistung haben wir eine neue Methode entwickelt, mit der der momentane Ladungszustand eines einzelnen NV direkt, zerstörungsfrei gemessen wird, womit die Echtzeitdynamik des Ladungszustands beobachtet werden kann. Mithilfe dieser Messmethode ist es uns gelungen, die Ionisierungsenergie (2.6 eV) und Rekombinationsenergie (2.94 eV) von NV^- zu bestimmen. Zudem konnten wir mit dem neu gewonnen Wissen die optische Polarisation des Elektronenspins von zuvor $\approx$ 91.8 % auf $\approx$ 97.2 % verbessern. Mit der neuen Methode zur Messung des Ladungszustands kann man diesen auch initialisieren. Zusätzlich haben wir einen weiter Ansatz entwickelt zur Nachselektion von Messergebnissen, die bei einem bestimmten Ladungszustand entstanden sind. Dabei wird effektiv der Ladungszustand auf den ^{14}N Kernspin übertragen, und kann wegen dessen langer Lebenszeit nach einem experimentellen Durchlauf mittels direkter Zustandsmessung ausgelesen werden. Die Kontrolle des Ladungszustand wird besonders für zukünftige skalierbare NV-Systeme wichtig sein.

Auf Basis der direkten Zustandsmessung des ^{14}N Kernspins kombiniert mit den neu entwickelten Methoden zur Initialisierung des Ladungszustands haben wir mehrere fundamentale Grundlagenexperimente durchgeführt. So ist es gelungen, einen Algorithmus zur Quantenphasenabschätzung mit quantenlimitierter Messgenauigkeit einzusetzen, um Magnetfeldmessungen mit hohem Dynamikumfang zu realisieren. Im Vergleich zum herkömmlichen Ansatz der Phasen- und Magnetfeldmessung kann man mit diesem Algorithmus entweder die Messsensitivität bei gegebenem maximalen Magnetfeldbereich erhöhen, oder den maximalen Magnetfeldbereich bei gleichbleibender Sensitivität vergrößern. Diese Methode ist nicht beschränkt auf Magnetfeldmessungen, sondern kann generell für die Messung von Energiedifferenzen zwischen den Zuständen eines quantenmechanischen Systems auf Basis der Lamorfrequenz angewandt werden.

Mit einer hohen Messgenauigkeit von Kernspin und Ladungszustand konnten wir die Verletzung von zeitlichen Bellschen Ungleichungen demonstrieren. Zeitlichen Bellschen Ungleichungen berechnen sich aus zeitlichen Korrelationen der Dynamik eines einzelnen Systems, und durch Einführung der *Realismus*-Annahme. Diese besagt, dass der Zustand eines Systems (im Sinne des Messresultats) jederzeit definierbar sein muss, d.h. dass es immer möglich ist, dem Zustand eines Systems eines seiner Zustandsmessresultate zuzuweisen. Die *Realismus*-Annahme impliziert, dass die Dynamik des Systems deterministisch ist. Solche Ungleichungen werden von der Quantenmechanik verletzt, und die experimentelle Implementierung zeigt, dass die Quantenmechanik in der der Tat eine vollständige Theorie darstellt, die nicht-deterministisch ist. Diese Eigenschaft

der Quantenmechanik ist besonders wichtig für die Quantenkryptographie.

Ein weiteres Experiment dieser Arbeit beschäftigt sich mit der experimentellen Unterscheidbarkeit von nicht-orthogonalen Zuständen. Nach den Regeln der Quantenmechanik ist diese Unterscheidung nicht perfekt möglich. Allerdings lassen sich solche Messungen mithilfe einer verallgemeinerten Messtheorie (bei der die Messoperatoren nicht orthogonal sein müssen) bezüglich unterschiedlicher Anforderungen optimieren. Hier haben wir die Unterscheidung von nicht-orthogonalen Zuständen einerseits mit der minimaler Fehlermessung und andererseits mit eindeutiger Zustandsbestimmung durchgeführt und verglichen. Dabei wurden die drei Zustände des ^{14}N Kernspins ausgenutzt. Solche Messmethoden können für Quantenkryptographie und Quantenteleportation ausgenutzt werden.

Eine wichtige Aufgabe zur praktischen Anwendung von Quanteninformationsverarbeitung ist die Vergößerung des verfügbaren Quantenregisters. Dazu haben wir die Methode zur direkten Zustandsmessung auf mehrere ^{13}C Kernspins erweitert. Eine Initialisierungswarscheinlichkeit des Kernspinregisters von 99 % wurde über eine Kombination aus Polarisationsübertrag vom Elektronenspin und direkter Zustandsmessung erreicht. Zudem wurde eine neue Operation entwickelt, um nicht-lokale Zustandsmanipulationen zwischen Kernspins, die selbst keine direkte Wechselwirkung zeigen, über die Hyperfeinwechselwirkung zu realisieren. Diese Operationen wurden mittels optimaler Kontrollmethoden implementiert, womit die vergleichsweise schnelle Dekohärenz des Elektronenspins teilweise vermieden werden kann. Dadurch wurde die Verschränkung von drei Kernspins mit hoher Genauigkeit von > 85 % erreicht, die mit Zustandstomographie nachgewiesen wurde. In diesem Register wurden die Vorteile seiner heterogenen Natur ausgenutzt, indem nur die Kernspins als Informationsspeicher genutzt wurden, während Kontrolle, Initialisierung und Auslesen über den Elektronenspin erfolgten. Mit der hier erreichten Kontrolle konnten wir Quantenfehlerkorrektur realisieren, ein wichtige Methode für skalierbare Quanteninformationsverarbeitung. Zudem haben wir theoretisch untersucht, wie die durschnittliche Anzahl nutzbarer ^{13}C Kernspins pro NV von der Kontrollmethode der Kernspins und dem äußeren Magnetfeld abhängt. Durch Ausnutzung sogenannter schwach gekoppelter Kernspins sollten an jedem NV mehrere nutzbare Kernspins detektierbar sein. Eine Methode zur Detektion solcher Kernspins bei hohem Magnetfeld wurde vorgestellt und für einen Kernspin erfolgreich experimentell implementiert.

Die Ergebnisse dieser Arbeit wurden publiziert in [43, 44, 45, 46, 47, 48].

Fazit In dieser Arbeit wurden die potentiellen Anwendungsmöglichkeiten des NV für Quanteninformationsverarbeitung untersucht, besonders in Hinblick auf die Ausnutzung von umliegenden Kernspins. Ein wichtiger Aspekt hierbei ist die Verbesserung der Kontrolle über diese Kernspins. Die Grundlage dazu bildet das neu gewonnene Verständnis über die Photoionisierung, auf deren Basis die Genauigkeit von Zustandsmanipulationen deutlich verbessert werden konnte. Anhand verschiedener Experimente zu zeitlichen

Bellschen Ungleichungen, der Unterscheidung von nicht-orthogonalen Zuständen und einem Algorithmus für Quantenphasenabschätzung konnte diese Kontrolle und Anwendungsmöglichkeiten demonstriert werden. Zudem haben wir das verfügbare Quantenregister aus Kernspins vergrößert, wobei selektive, direkte Zustandsmessung aller Systeme und universelle Quantenkontrolle gegeben war. Unter Ausnutzung des heterogenen Systems und dem Einsatz von optimalen Kontrollmethoden gelang die Verschränkung von drei Kernspins und Quantenfehlerkorrektur mit hoher Genauigkeit.

In Zukunft kann dieses hier demonstrierte Quantenregister noch weiter ausgebaut werden. Besonders durch die Ausnutzung von schwach gekoppelten Kernspins wird es deutlich wahrscheinlicher, mehrere nutzbare Kernspins an einem einzelnen NV zu finden. Allerdings ist auch diese Methode limitiert durch die Hyperfeinwechselwirkung, ein wirklich skalierbares System mit einem NV und Kernspins ist nicht machbar. Dazu benötigt man die Kopplung von einzelnen NVs, z.B. durch direkte Dipol-Dipol Wechselwirkung [49] oder über Photonen [50], was mit den hier gezeigten Methoden zur Kernspinkontrolle kombiniert werden kann. Aber auch das hier benutzte Register aus drei Kernspins kann neue Grundlagenexperimente ermöglichen, z.B. die Demonstration von Quantensimulationen oder von sogenannten schwachen Messungen und schwachen Werten [51, 52].

Die Experimente in dieser Arbeit wurden am Stickstoff-Fehlstellenzentrum in Diamant durchgeführt, demonstrieren aber darüber hinaus das Potential von Spinsystemen basierend auf Defektstellen in Festkörpern. Andere solche Defektstellen die bisher untersucht wurden sind beispielsweise Phosphor in Silizium [12, 53, 54, 55], verschiedene Defekte in Siliziumcarbid [56], oder Seltene Erden Ionen in Kristallen [57, 58]. Während sich diese System in der Initialisierung und Auslesemethode des Elektronenspins vom NV teilweise unterscheiden, sind die Mechanismen zur Elektronen- und Kernspinkontrolle über magnetische Wechselfelder und die Hyperfeinwechselwirkung die gleichen.

Summary

Introduction Interest in quantum information processing arose since 1985, when D. Deutsch proposed in [1] that by building a computer which exploits the laws of quantum mechanics, computational problems could be solved much more efficiently than by using a classical computer. This idea was picked up by other scientists, and indeed, this was found the be the case for real-world computational problems like prime factorization or search algorithms [2, 3]. Furthermore, it was pointed out by Feynman that quantum computers could be used to efficiently simulate quantum mechanical systems [4]. Another promising application of QIP is quantum cryptography [5], as quantum mechanics allows for transmission of information with fundamental, physical security. This is provided by the probabilistic nature of quantum mechanics, and because a quantum state is influenced by its measurement. The daunting challenge for the experimental realization of quantum information processing is the requirement of achieving a high degree of control over interacting, physical systems, which should at the same time have only very weak interactions with their uncontrolled environment. Among systems like photons [6, 7], trapped atoms [8], nuclear magnetic resonance [9], superconductors [10] and quantum dots [11], defects in solids [12] like the NV [13, 14] are promising candidates for QIP [59].

The NV can be thought of as an atom / molecule trapped inside the diamond crystal. It can be used as a single photon source due to its optical stability and high fluorescence [15, 16]. NVs in nanodiamonds can also be used as fluorescence markers [17, 18, 19]. Within a clean enough diamond, the electronic spin of the negatively charged NV, NV^-, provides a single quantum mechanical toy model, whose state can be measured and manipulated to observe quantum mechanical dynamics of a single quantum system. The distinct feature of NV^- is its spin dependent photo-physics, which allows purely optical initialization and readout of the spin state [20], combined with long spin coherence times in the electronic ground state [21, 22]. Furthermore, many experiments with the NV can be carried out at room temperature, due to the high Debeye temperature of diamond, which leads to relatively long spin lifetimes. The energy splitting of its electron spin depends on many environmental parameters, such that the NV can be used as a quantum sensor with nanometer resolution of magnetic fields [23, 24, 25, 26, 27] including external spins [28, 29, 30], electric fields [31], and temperature [32, 33, 34, 35]. Here, we investigate the potential applicability of NV^- for QIP [13], while all experiments of this work were performed at room temperatur.

Specifically, we focus on using nuclear spins surrounding the NV as quantum resources to increase the versatility of a single NV. This results in a natural heterogeneous spin

system. The advantage of such a system is that the desired features of the different subsystem species can be combined. In the case of a spin system consisting of electron and nuclear spins, the electron spin can be used for quantum control due to its comparatively strong interaction, and the nuclear spins can be used as a long lived quantum memory. Coherent control of a single ^{13}C nuclear spin nearby an NV was first demonstrated in [36]. The potential of using these nuclear spins as a quantum register was further investigated [37, 38, 39], analysing the storage and retrieval of information on ^{13}C nuclear spins and their coherence properties, and entanglement of two ^{13}C nuclear spins was achieved [40]. This thesis is strongly based on quantum non-demolition measurement of nuclear spins with the NV, which enables projective, single shot readout [41, 42].

Thesis outline In chapter 1 the physical basics of this work regarding quantum information processing, theoretical and practical aspects of the NV and the dynamics of spins are summarized. In chapter 2 we investigate the photo-ionization of the NV. There we show the proof of NV^0 via NMR, a method for real-time measurement of the charge state, which is also applied to analyze the charge state dynamics, and the improvement of the electron spin polarization. In chapter 3 several proof-of-principle experiments on the basis of ^{14}N single shot readout are shown. These are violation of a temporal Bell inequality, distinguishing between non-orthogonal quantum states, and a quantum phase estimation algorithm for high dynamic range magnetometry. In chapter 4 a quantum register based on the NV electron spin and three nuclear spins is presented. We show initialization and readout of the nuclear spins, implementation of non-local gates with optimal control, and finally three-qubit entanglement and quantum error correction. Additionally, we investigate the usability of so called weakly coupled nuclear spins.

Results of this work After the development of single shot readout of the ^{14}N nuclear spin associated with the NV [41], it was found that nuclear spin operations seem to be only ≈ 70 % efficient. In this thesis, we investigated this behavior, and found that the reason is photo-induced ionization and recombination of the NV, leaving it in a mixture of NV^- and NV^0, with at most 75 % population in NV^-. Thereby, only NV^- can be used for our experiments, as the spin coherence times in NV^0 are too short. The ionization and recombination dynamics was thoroughly investigated depending on illumination wavelength and power, which yielded an important contribution to the understanding of the NV. By properly choosing the excitation wavelength and power, a novel method for non-destructive, single shot charge state detection is presented, which allows for real-time observation of the charge state dynamics. The observed dynamics allowed the determination of the NV^- ionization (2.6 eV) and recombination energy (2.94 eV) and thus its ground state energy relative to the diamond band gap. Furthermore, the obtained understanding of this process allows us to improve the optical polarization of the NV electron spin from previously ≈ 91.8 % to ≈ 97.2 %. This new method for non-destructive, single shot charge state detection also allows for initialization of the charge

state. In addition to this method, another approach for charge state post-selection was developed, which is based on effectively mapping the charge state onto the ^{14}N nuclear spin, and final detection by nuclear single shot readout. In future applications of the NV for QIP, charge state control will be crucial for a scalable system.

Nuclear single shot readout combined with these new methods for charge state initialization and post-selection enabled several fundamental, proof-of-principle experiments. We achieved implementation of a quantum phase estimation algorithm with quantum limited accuracy, which allowed for magnetic field sensing with high dynamic range. Compared to the standard approach, this new method can be used to increase the sensitivity for a given maximum magnetic field range, or to increase the accessible magnetic field range with constant sensitivity. This algorithm is not limited to magnetic field sensing, but can be applied generally to the measurement of energy differences of a quantum mechanical system via the Lamor frequency.

With high fidelity initialization and readout of nuclear spin and charge state we could demonstrate violation of a temporal Bell inequality. Temporal Bell inequalities are obtained by calculating temporal correlations of the dynamics of a single system, and by imposing the *realism* assumption, which states that the state of a system (in the sense of a measurement result) can always be defined. This implied that the dynamics of the system are deterministic. This type of inequalities is violated by quantum mechanics, and the experimental implementation shows that quantum mechanics can be considered a complete theory which is non-deterministic. This behavior of quantum mechanics is important e.g. for quantum cryptography.

A further experiment in this work is about experimental distinguishing between non-orthogonal quantum states. According to quantum mechanics, this is not possible perfectly due to the partial overlap of the states. However, on the theoretical basis of generalized measurements (with non-orthogonal measurement operators), such measurements can be optimized with respect to different requirements. Here, we performed and compared distinguishing between non-orthogonal quantum states on the one hand with the minimum error measurement, and on the other hand with unambiguous state discrimination. This was achieved by utilizing the triplet character of the ^{14}N nuclear spin.

An important task for practical application of quantum information processing is increasing the size of the available quantum register. Therefore, we extended projective, single-shot readout of the ^{14}N nuclear spin onto several ^{13}C nuclear spins with a single NV. An initialization fidelity of 99 % of the nuclear register was reached by a combination of swap-gates with the electron spin and projective readout. Additionally, we developed a new method for non-local operations between nuclear spins, which show no direct interaction, via the hyperfine interaction with the electron spin. These operations were implemented by optimal control, which allows for partially avoiding the fast decoherence of the electron spin. Thereby, we achieved high fidelity entanglement (> 85 %) of three nuclear spins, which was observed by state tomography. In this register, the advantages of its heterogeneous nature were exploited, by using only the nuclear spins for information storage, and the electron spin was merely used for control, initialization

and readout. With the achieved high degree of control, we were able to realize quantum error correction, an important tool for scalable quantum information processing. Furthermore, we analyzed theoretically the average number of usable ^{13}C nuclear spins per NV depending on the control method of nuclear spins and the external magnetic field. By including so-called weakly coupled nuclear spins, several such spins should be usable per NV. A method for detection of weakly coupled nuclear spins is presented and implemented experimentally for one such nuclear spin.

The results of this thesis were published in [43, 44, 45, 46, 47, 48].

Conclusion In this work the potential application of the NV for quantum information processing was investigated, especially regarding the use of surrounding nuclear spins. An important aspect for this goal is improving the control of these nuclear spins. A fundamental result was the new understanding of the NV photo-ionization, which allowed to improve the fidelity of gate operations considerably. With several experiments, namely violation of a temporal Bell inequality, distinguishing between non-orthogonal quantum states and implementation of a quantum phase estimation algorithm, this control and the potential of the NV could be demonstrated. Furthermore, we increased the available nuclear spin quantum register, with projective, single-shot readout of all qubits and universal quantum control (i.e. that any unitary operation can be realized). By exploiting the advantages of the heterogeneous system and the application of optimal control we achieved three-qubit entanglement and quantum error correction with high fidelity.

In the future, the quantum register demonstrated here could be further improved. Especially by using weakly detected nuclear spins, it becomes likely to find more usable nuclear spin at a single NV. However, the size of the register using this method is limited by the range of the hyperfine interaction, such that a truly scalable system cannot be realized with a single NV and nuclear spins. Such a scalable system can be achieved by coupling of NV centers, e.g. via direct dipole-dipole interaction [49] or via photons [50], which can be combined with the control methods for nuclear spins demonstrated in this work. But even the register presented here can be used for new proof-of-principle experiments, e.g. demonstration of quantum simulations and of weak measurements and weak values [51, 52].

The experiments presented in this work were performed with the nitrogen-vacancy defect, however, they also demonstrate the potential of spin based solid state defects in general. Other such defect centers which were investigated so far are phosphorus in silica [12, 53, 54, 55], various defects in silicon carbide [56], and rare-earth ions in solid [57, 58]. While these systems partially differ in electron spin initialization and readout methods, the mechanisms for electron and nuclear spin control via time dependent magnetic fields and the hyperfine interaction are the same.

List of Figures

List of Tables

Acronyms

DD dynamical decoupling

DOS density of states

DPSS diode pumped solid state

FID free induction decay

FWHM full width at half maximum

GRAPE gradient ascent pulse engineering

hf hyperfine

NMR nuclear magnetic resonance

NV nitrogen-vacancy center

mw microwave

odmr optically detected magnetic resonance

rf radio frequency

SIL solid immersion lens

SQUID superconducting quantum interference device

TBI temporal Bell inequality

QEC quantum error correction

QIP quantum information processing

QM quantum mechanics

QPEA quantum phase estimation algorithm

1. Introduction to physical basics

In this chapter, the current state of knowledge which is necessary for the motivation and understanding of the work presented in this thesis is reviewed. We will start with a short introduction to quantum information processing (section 1.1), which motivates this work on the Nitrogen-Vacancy defect (NV). The NV is introduced in section 1.2, which gives an overview over the physical properties of the NV, its level structure, the spin Hamiltonian, and the experimental setup. Furthermore, we will focus on the interaction of the NV with surrounding nuclear spins, which can greatly increase the versatility of single NVs for QIP. Finally, the dynamics and manipulation of spin states by time-dependent magnetic fields is discussed in section 1.3.

1.1. Quantum information processing

Quantum information processing (QIP) describes the processing of information (computation, communication), by exploiting the laws of quantum mechanics. Most of the contents of this introduction to QIP can be found in the book by Nielsen and Chuang [60]. QIP can offer unique advantages over classical computation and communication. For solving a computational problem, an important question is how much resources are needed to solve the problem. Here, two so-called complexity classes are important for our considerations: The **P** complexity class, which refers to problems that can be solved efficiently on a classical computer, where 'efficiently' usually indicates that the number of computational steps scales polynomially with the size of the problem. The **NP** class is defined by computational problems, for which a possible solution can be efficiently checked on a classical computer. Much interest arose in QIP when quantum algorithms were proposed, which offer unique computational advantages compared to classical algorithms, and can even solve certain classical **NP** problems efficiently. One of the first quantum algorithms proposed was the Deutsch algorithm [1], which also beautifully illustrates how quantum mechanical features lead to improved computation. One the hand, the superposition principle (i.e. coherences for a single qubit or entanglement of multiple qubits) leads to *quantum parallelism*, where a single operation is applied to several input parameters (quantum states) at the same time. However, this is not directly useful, as a final measurement will project the system into one of its states, removing all superposition. In addition to this *quantum parallelism*, exploiting *interference* of the states can be used to extract general information of different possible results at once. In

the case of the Deutsch algorithm, this allows to determine if a function has the property $f(0) = f(1)$ by a single application of the function f. While this algorithm is of little practical use, the are other quantum algorithms like the quantum Fourier transform or quantum search that can be applied to real-world problems, providing substantial advantages in computational effort compared to their classical implementations.

Another interesting application is quantum simulation, which cannot be implemented efficiently on a classical computer. The reason is that in order to describe a quantum mechanical system, not only the states of the individual sub-systems are needed, but also possible coherences and entanglement between these systems. The classical memory required to describe a quantum state increases exponentially with the size of the quantum systems. On the other hand, simulation of a quantum mechanical system on a quantum computer can be done efficiently, thus being an important application for other fields of physics or chemistry.

Apart from quantum computation, communication based on quantum mechanics also offers unique benefits over classical communication. The most important application in this field is probably quantum cryptography [5], which is also believed to be the potentially first application of QIP. The basic principle of quantum cryptography is that eavesdropping is theoretically impossible, as quantum measurements will perturb (project) the system, and quantum states cannot be cloned. Therefore, if information is sent from some point A to another point B, any measurements in between can be revealed. One exclusion of this principle are measurements that are performed in the same basis as the information is stored, such that the projection of the state does not actually perturb it. To avoid this possibility of eavesdropping, the quantum states have to be sent either with random basis, or by using non-orthogonal states for the transmission.

1.1.1. Physical implementation

As we have seen, QIP has potential, powerful applications. However, physical implementation of quantum computation is very challenging. The necessary requirements for a quantum computer were first introduced by DiVincenzo [61], which were re-formulated in [59]:

1. "A scalable physical system with well characterized qubits." This requirement leads to the possibility of increasing the Hilbert space of the system exponentially, with the theoretical linear effort of adding qubits to the system. In a physical system, the effort to add a qubit usually scales with the size of the system. This lead to the re-formulation of this requirement for a scalable system [59], that the effort (time, space, energy etc.) of adding a qubit must scale less than exponential.

2. "The ability to initialize the state of the qubits to a simple fiducial state, such as $|000...\rangle$." It is important to note here that this initialization of qubits must not only be performed at the start of the computation, but also while the computation

is running. This is necessary for scalable QIP, in order to perform quantum error correction and remove the entropy generated by errors from the system.

3. "Long relevant decoherence times, much longer than the gate operation time." This is important for high-fidelity implementation of quantum gates. The figure of merit for the fidelity is given by the threshold theorem for quantum error correction (see below), and depends on the architecture of the quantum computer [62].

4. "A 'universal' set of quantum gates." In a newer formulation [59], this requirement is termed "Universal logic", meaning that the whole Hilbert space must somehow be accessible, without exponential increase in effort. A common example is the combination of arbitrary rotation gates on single qubits, and one two-qubit gate, e.g. a CNOT gate. Other approaches are adiabatic quantum computation [63], or measurement based quantum computation which requires preparation of the system in so-called cluster states [64].

5. "A qubit-specific measurement capability." After a quantum computation, it is necessary to read out the final, resulting state. This measurement most not necessarily be projective with fidelities approaching 100 %, however, these strong measurements can be helpful for initialization and error correction.

Note that in the explanation of these requirement by DiVincenzo, the importance for quantum error correction is emphasized. Indeed, in a newer formulation [59], quantum error correction is even termed a requirement on its own, replacing some of DiVincenzo's criteria.

Each of these requirements, on its own, is not impossible with nowadays technology. What makes scalable QIP such a daunting challenge is their combination, as they partly contradict each other. On the one hand, the required long coherence times means that the systems must be very well-isolated from their (uncontrolled) environment. On the other hand, the high amount of control necessary for fast, universal gates, initialization and readout requires strong enough interactions with some sort of control apparatus.

So far, there are several physical systems which are possible candidates for QIP [59], like photons, trapped atoms, nuclear magnetic resonance (NMR), superconducting quantum interference device (SQUIDS) and quantum dots / defects in solids. In this thesis, we investigate a defect in solid, namely the nitrogen-vacancy centre (NV) in diamond.

1.1.2. Quantum error correction

An import concept for scalable QIP is quantum error correction (QEC), as it presents a method to overcome the inevitable decoherence of quantum systems. A mile-stone theoretical work is fault tolerant quantum computation [65, 66, 67, 68] on the basis of concatenated QEC, yielding the threshold theorem [69, 70]. The threshold theorem

states that the error of any quantum algorithm can be made arbitrarily small, if concatenated QEC is applied and the probability of a single error is below a certain threshold (which depends on the actual physical architecture of the quantum computer). Error correction is well known for classical computation. There, information can be stored via redundancy, such that the relevant information can be restored if parts of the full information are corrupted. Consider the storage (encoding) of one bit of information $\{0, 1\}$ onto three bits $\{000, 111\}$. If one bit of the encoded information is changed, the original one bit of relevant information can be restored by majority vote.

For quantum information, there are a few obstacles to this approach, however, which are all solvable:

1. The no-cloning theorem. It is impossible to copy a quantum state. Still, we can create an encoded, entangled state of multiple qubits, such that all qubits will be found in the same state as the original single qubit. Note that the coherences of the original qubit, however, are then not stored on each qubit individually, but only once in the multi-qubit entanglement. Nevertheless, we will see that this is enough to employ a majority-vote principle.

2. Quantum state errors are continuous; measurements destroy quantum coherences. Here the latter actually cancels out the former. On the one hand, the state of a qubit is an analogue state offering infinite error possibilities, which seems to require infinite precision for correction. Furthermore, measurements destroy the coherence information by projecting the system onto a state corresponding to the measurement result. However, this is only the case if we measure the actual information carried by the system, and can be used to our advantage. By designing the measurement such that it probes whether an error occurred, only coherences between the error-free states and the erroneous states are destroyed by projecting the system onto one of these two cases, whereas the coherences carrying the quantum information are not affected. Due to this projection, we are left with the two possibilities of having an error or not having an error, and the continuous aspect of the error is removed.

3. There are two types of errors for quantum information: bit flip and phase flip error. As the name suggests, bit flip errors are defined by the operation $|0\rangle \leftrightarrow |1\rangle$, whereas phase flip errors are $\alpha|0\rangle + \beta|1\rangle \leftrightarrow \alpha|0\rangle - \beta|1\rangle$, which is equivalent to $|x_+\rangle \leftrightarrow |x_-\rangle$, $|y_+\rangle \leftrightarrow |y_-\rangle$ (where $|x_\pm\rangle = (|0\rangle \pm |1\rangle)/\sqrt{2}$, $|y_\pm\rangle = (|0\rangle \pm \mathrm{i}\,|1\rangle)/\sqrt{2}$). Written in the latter form, phase flip errors have the same effect as bit flips, just in a different basis. Changing the basis the information is stored in can be done by only local $\pi/2$ rotations. Thus, bit flip and phase flip correction is implemented in effectively the same way, only differing by these local $\pi/2$ rotations. Nevertheless, the possibility of two types of errors means that more storage qubits are needed for full QEC. In experimental implementations, however, the rate of phase flip errors is usually much larger than the rate of bit flip errors. In our case, where the qubit

is defined by two orientations of a spin, these two errors types have a different physical origin. The bit flip errors correspond to T_1 decay, which is caused by energy exchange with the environment (relaxation). Phase flip errors are induced by the energy splitting of the two levels, which depends on the environmental state, yielding an uncontrollable phase accumulation due to changes of the Lamor frequency.

Here, we will illustrate the basic mechanism for three qubit phase flip error correction. The first step is to encode the information $|\psi\rangle = \alpha|0\rangle + \beta|1\rangle$ into two logical states of the three qubits as $\alpha|000\rangle + \beta|111\rangle$, and then change the basis where this information is stored to e.g. $\alpha|x_+x_+x_+\rangle + \beta|x_-x_-x_-\rangle$ by a $(\pi/2)_y$-rotation (we could also store in the y-basis). Note that this state is not affected by $|y_+\rangle \leftrightarrow |y_-\rangle$ errors. The encoding can also be written in terms of the logical qubit states $|0_\mathrm{L}\rangle$, $|1_\mathrm{L}\rangle$ as $|0\rangle \rightarrow |0_\mathrm{L}\rangle = |x_+x_+x_+\rangle$, $|1\rangle \rightarrow |1_\mathrm{L}\rangle = |x_-x_-x_-\rangle$. After a possible phase flip error $|x_+\rangle \leftrightarrow |x_-\rangle$, the basis is changed back to the eigenbasis by a $(-\pi/2)_y$-rotation, such that these errors effectively appear as bit flip errors. For example, for an error on the first qubit $\alpha|x_-x_+x_+\rangle + \beta|x_+x_-x_-\rangle \rightarrow \alpha|100\rangle + \beta|011\rangle$. As mentioned above, the errors are continuous, i.e. the system will generally be in a mixture of having no error, having an error on each qubit and having multiple errors. This entropy can be removed by so-called syndrome measurements. We can detect possible errors by measuring if the system is in the Hilbert-subspace corresponding to a certain error. Ideally, this measurement will project the state onto either the subspace corresponding to the error, or on the remaining part of the Hilbert space, without destroying the coherences within these subspaces. E.g. if the system is found in subspace $\{|100\rangle, |011\rangle\}$, we assume that a single error occurred on qubit 1, and can thus correct this error by flipping qubit 1. In the same way, errors on the other qubits can be detected and corrected. Of course, we could also find the system in subspace $\{|100\rangle, |011\rangle\}$ if two errors on the other qubits occurred, which means that these multiple errors inevitably destroy the information. If the probability p of an error is the same for each qubit, then a lower bound on the probability of successful error correction is $1 - 3p^2 + 2p^3$.

In a physical implementation of the syndrome measurement, coherences within the subspaces might not be preserved, due to the strong influence of the measurement onto the system. This measurement can also be replaced by using an ancillary qubit. For this approach, the syndrome is mapped onto the ancillary qubit by a flip of this qubit conditional of the system being in a subspace corresponding to a certain error. Then, the possible error is corrected by a flip of the system conditional on the state of the ancillary qubit. Thus, the entropy generated by the error in the system is transferred to the ancillary qubit. After each correction step, the state of this qubit has to be re-initialized to remove this entropy. A third approach, which we experimentally implement in this work, does not even need an ancillary qubit [71]. The scheme corrects possible errors for only a single qubit of the system, transferring any error onto the other qubits, see section 4.5 for details. To remove the entropy, these other qubits then have to be reset.

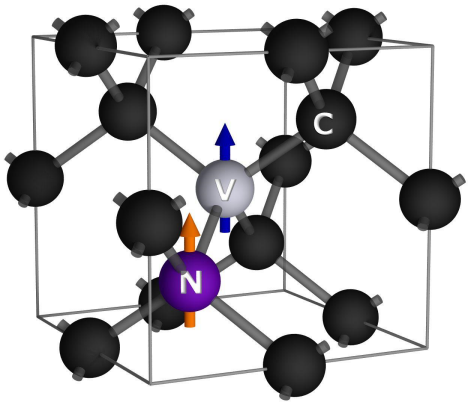

Figure 1.1.: Physical structure of the NV. Blue arrow: Illustration of the electron spin, which is located close to the vacancy in the NV^- ground state. Orange arrow: Illustration of the nitrogen nuclear spin.

1.2. The Nitrogen-Vacancy defect in diamond

All the experiments presented in this thesis are based on the Nitrogen-Vacancy defect (NV) in diamond. The NV is a point defect consisting of a substitutional nitrogen atom and an adjacent lattice carbon vacancy, as illustrated in fig. 1.1. It can occur naturally in diamond, or for instance can be created by nitrogen implantation, electron irradiation and annealing [72, 20, 73, 74]. The diamond host is either natural diamond, or can be produced artificially by high pressure high temperature (HPTP) or chemical vapour deposition (CVD) [75]. In this section, the basic properties of the NV at room temperature are introduced, with focus on its negative charge state NV^-. We will discuss its electronic structure, leading to the optical spin polarization and readout. The basic experimental setup which was used for this work is presented. We will specifically focus on nuclear spins which are hyperfine coupled to the NV, in order to understand the necessary requirements for nuclear spin single shot readout.

1.2.1. Electronic structure and photophysics

Several studies have investigated the electronic structure of the NV, yet detailed understanding of all energy levels and transitions has to be obtained by future work. We will focus on established knowledge based on a recent review by M. Doherty [14], with effective descriptions relevant for this work. Depending on the local Fermi level, both the neutral charge state NV^0 and the negative charge state NV^- can be stable [76]. The electronic structure of the NV is formed by the three dangling bonds of the carbon atoms neighbouring the vacancy, two electrons from the nitrogen atom, and one additional electron for the negative charge state. These electrons fill the orbitals $a_1(1)$, $a_1(2)$, $e_{x,y}$, with energy ordering $a_1(1) < a_1(2) < e_{x,y}$ [77, 78]. Here, we will only consider the

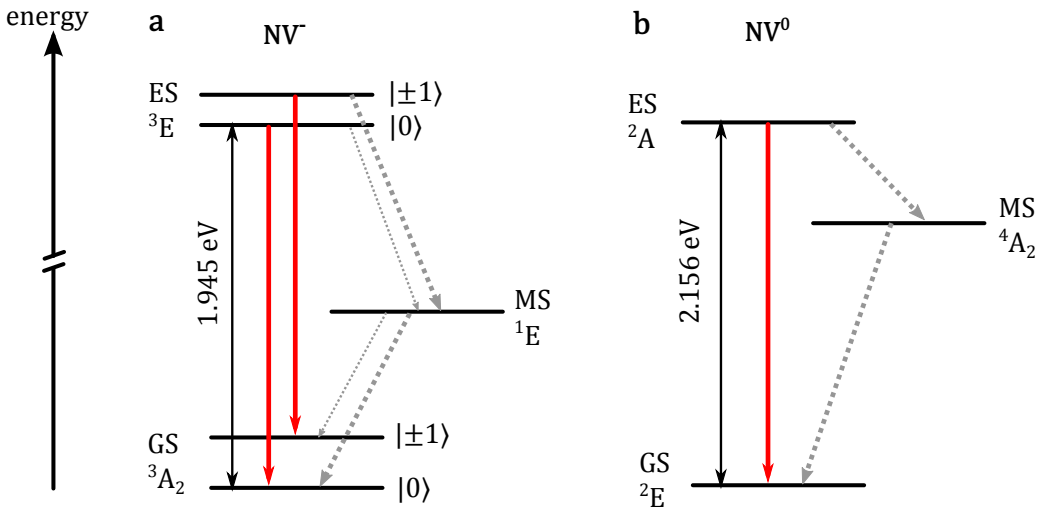

Figure 1.2.: Effective energy level scheme of NV^- and NV^0. GS: ground state, ES: excited state, MS: metastable state. Red lines indicate radiative decay, grey dotted lines non-radiative decay (the width of the grey lines indicates relative decay rate). **a**, NV^-. **b**, NV^0.

$a_1(2)$ and $e_{x,y}$ orbitals, as the $a_1(1)$ is filled for all relevant states.

NV^- For the six electrons of NV^-, fig. 1.2a shows the energy level scheme of the ${}^3A_2$ ground state triplet with configuration a^2e^2, the ${}^1E$ metastable singlet state (also a^2e^2), and the ${}^3E$ excited state triplet (a^1e^3). The zero-phonon line of the ${}^3A_2$ ground state to ${}^3E$ excited state is 1.945 eV. Fig. 1.2a also shows the possible decay channels. In bulk diamond, the excited state lifetimes are $\approx$ 12 ns for the $m_S = 0$ spin state, and $\approx$ 7.8 ns for $m_S = \pm 1$ [79]. This difference is an important feature of NV^-, and is due to spin-state dependant inter-system crossing. From the excited state, there are two decay channels: The radiative decay back into the ground state, and non-radiative decay into the metastable singlet state by phonon assisted inter-system crossing. The former transition ${}^3A_2 \leftrightarrow {}^3E$ is spin conserving. The latter non-radiative decay is spin state dependant, such that the decay rate is higher for the $m_S = \pm 1$ states compared to $m_S = 0$. In addition to this, the non-radiative decay rate from the metastable state is higher into the $m_S = 0$ state than into the $m_S = \pm 1$ state. The lifetime of the metastable state is $\approx$ 250 ns [80]. These two effects lead to optical spin polarization and readout. On the one hand, the fluorescence of the $m_S = \pm 1$ states is reduced due to trapping in the metastable state. On the other hand, the preferential inter-system crossing for $m_S = \pm 1$ and the preferential decay from the singlet state into the $m_S = 0$ ground state results in optical polarization into $m_S = 0$ by illumination.

NV^0 Fig. 1.2b shows the energy level scheme of NV^0, with the doublet ground state ^2E (a^2e^1), doublet excited state ^2A (a^1e^2) and quartet metastable state $^4A_2$ (a^1e^2). The zero-phonon line is 2.156 eV. Much less is known about the photophysics of NV^0 compared to NV$^-$, however, it also seems to exhibit spin state dependant inter-system crossing [81].

1.2.2. Experimental setup

The experimental setup is illustrated in fig. 1.3. The laser (mostly a 532 nm, 300 mW diode-pumped solid state laser, or other lasers as indicated in the experiments) is sent through an acousto-optical modulator (AOM) for pulse generation with length > 10 ns. Other laser sources can be combined via a beam splitter before the photonic crystal fiber (PCF). The detection of single NV's is realized via a confocal microscope. The excitation laser hits a beam splitter (BS) and is reflected into a microscope objective, which focuses the light onto a diffraction limited spot inside the diamond. The objective is mounted to a piezo scanner for position control. If an NV is in this spot, it will be excited and emit fluorescence, which is partly collected by the objective. Then, the fluorescence passes the beam splitter and is filtered by a long pass filter to block the excitation laser. For lateral resolution, the fluorescence light is focused onto a pinhole. If the origin of the fluorescence is not within the focal plane of the objective, it will also not be focused onto the pinhole and is therefore blocked. Finally, the fluorescence photons are detected via avalanche photo diodes (APD). A confocal scan of a diamond showing single NVs is shown in fig. 1.3b, and a $g^2(\tau)$ correlation function in fig. 1.3c. The mw and rf signals are applied via a micro coplanar waveguide structure created by photo-lithography either on a glass cover-slide or directly on the diamond.

As mentioned in section 1.2.1, the fluorescence of the NV depends on its electronic spin state. Fig. 1.3d shows the average NV fluorescence for the initial states $m_S = 0$ and $m_S = \pm 1$. The difference of these two curves is the effective readout signal, which decays over time due to the polarization of the NV under illumination. A typical measurement sequence with the NV electron spin is illustrated in fig. 1.3e. After the first laser pulse, the electron spin is initialized into $m_S = 0$. Then, a control sequence is applied, typically consisting of mw signals for electron spin manipulation [21]. E.g. for measuring the electron spin resonance spectrum, the mw frequency is varied, and for Rabi oscillations, the mw pulse duration is varied while being in resonance to an electron spin transition. Finally, a second laser pulse reads out and re-initializes the electron spin. The readout signal is obtained by summation of all photons detected within the first ≈ 300 ns of the laser pulse. For bulk diamond and using an oil immersion objective, up to on average 0.1 photons per laser pulse can be detected. Fig. 1.3f shows an optically detected magnetic resonance (ODMR) spectrum within a small magnetic field (≈ 2 Gauss) oriented parallel to the NV axis, revealing the two electron spin transitions $m_S = 0 \leftrightarrow \pm 1$ with hyperfine (hf) splitting to the three ^{14}N nuclear spin states. Optically detected Rabi oscillations of the electron spin are shown in fig. 1.3g.

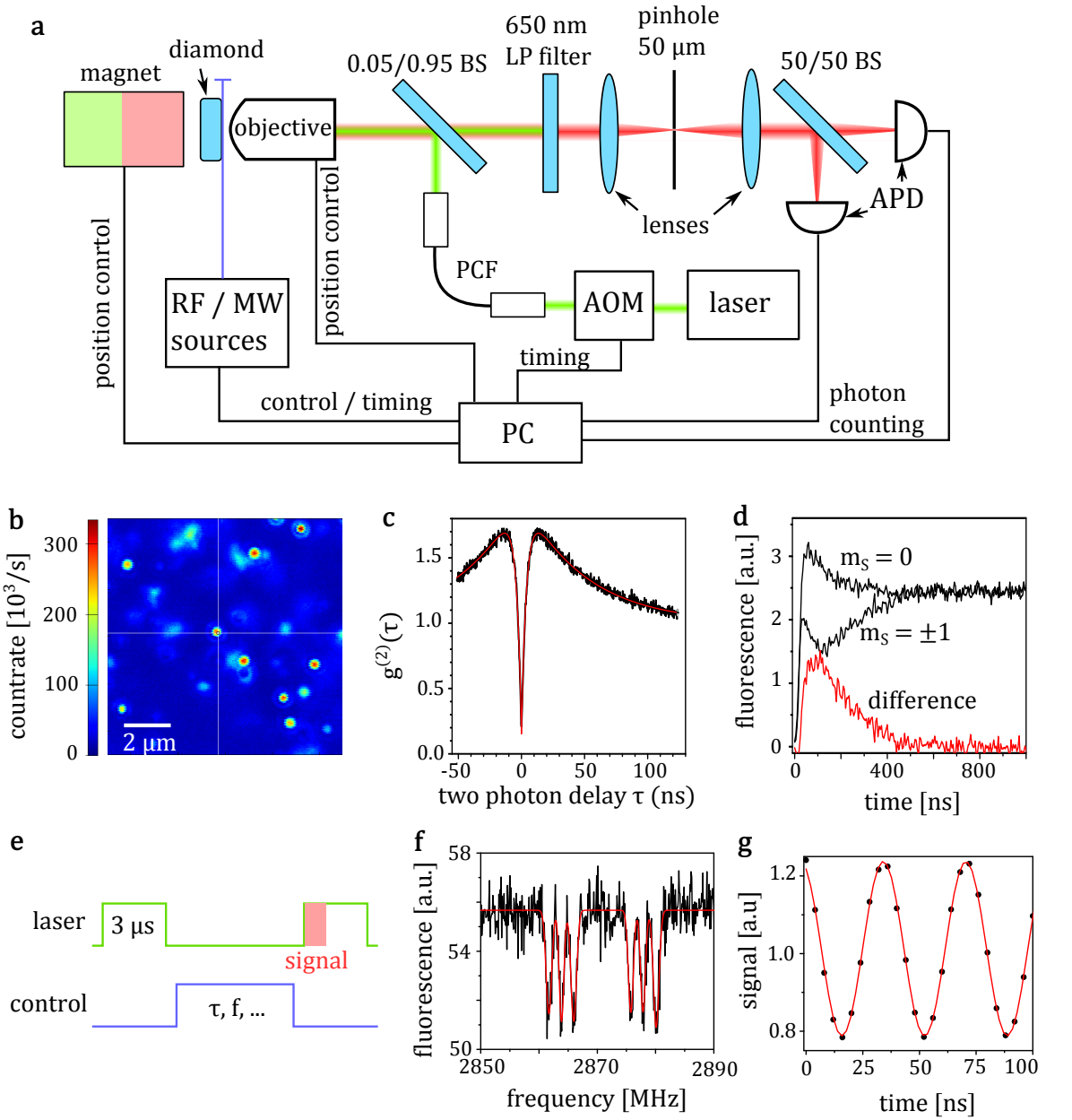

Figure 1.3.: Experimental setup and measurement techniques. **a**, Experimental setup, see text for description. **b**, Confocal scan image of natural bulk diamond. **c**, $g^2(\tau)$ correlation function of a single NV. **d**, Fluorescence of the NV during a green laser pulse after preparation in different m_S states. **e**, Basic measurement sequence. **f**, ODMR spectrum. **g**, Rabi oscillation of the electron spin.

1.2.3. Spin Hamiltonian: Electron and nuclear spins

The Hamiltonian of the NV^- electron spin coupled to nuclear spins is given by the sum of the electron spin Hamiltonian $\hat{H}_\mathrm{e}$, the nuclear spin Hamiltonian $\hat{H}_\mathrm{n}$ and the hyperfine Hamiltonian $\hat{H}_\mathrm{hf}$

$$\hat{H} = \hat{H}_\mathrm{e} + \hat{H}_\mathrm{n} + \hat{H}_\mathrm{hf}. \tag{1.1}$$

Because the electron spin is formed by two unpaired electrons, there is a zero-field splitting due to spin-spin interaction $\underline{\hat{S}}\mathbf{D}\underline{\hat{S}}$, where $\underline{\hat{S}}$ is the spin operator and $\mathbf{D}$ the interaction tensor. With the z-direction oriented along the NV axis, this interaction can be expressed as

$$\hat{H}_\mathrm{ZF} = D\hat{S}_z^2 + E(\hat{S}_x^2 + \hat{S}_y^2), \tag{1.2}$$

with the zero-field splitting $D = 2.87$ GHz in the ground state, and E results from deviations of the rotational symmetry, e.g. for strain or external electric fields. For the samples used in this work, E is small and can be ignored for these experiments. In addition to this, an external magnetic field $\underline{B}$ leads to a Zeeman splitting

$$\hat{H}_\mathrm{Z} = -\gamma_\mathrm{e}\underline{\hat{S}} \cdot \underline{B}, \tag{1.3}$$

with the gyromagnetic ratio $\gamma_\mathrm{e} = 28.03$ GHz/T of the electron spin.

For the ^{14}N nuclear spin $I = 1$, there will also be a zero-field splitting

$$\hat{H}_\mathrm{nZF} = Q\hat{I}_z^2, \tag{1.4}$$

with $Q = -4.945$ MHz for the ground state. All nuclear spins show a Zeeman splitting

$$\hat{H}_\mathrm{nZ} = \gamma_\mathrm{n}\underline{\hat{I}} \cdot \underline{B}, \tag{1.5}$$

where the gyromagnetic ratio γ_n depends on the type of nucleus: For ^{14}N $\gamma_\mathrm{n} = 3.0766$ MHz/T, for ^{15}N $\gamma_\mathrm{n} = -4.3156$ MHz/T, and for ^{13}C $\gamma_\mathrm{n} = 10.705$ MHz/T.

The hyperfine interaction originates from two terms, the isotropic Fermi contact interaction

$$\hat{H}_\mathrm{F} = a_\mathrm{iso}\underline{\hat{S}} \cdot \underline{\hat{I}}, \tag{1.6}$$

with interaction strength a_iso depending on the electron spin density at the location of the nucleus, and the anisotropic dipole-dipole interaction (given here for point dipole approximation)

$$\hat{H}_\mathrm{dd} = \frac{\mu_0}{4\pi}\gamma_\mathrm{e}\gamma_\mathrm{n}h\frac{\underline{\hat{S}} \cdot \underline{\hat{I}} - 3\left(\underline{\hat{S}} \cdot \underline{e}_r\right)\left(\underline{\hat{I}} \cdot \underline{e}_r\right)}{r^3}, \tag{1.7}$$

where μ_0 is the vacuum permeability, r the distance between electron and nuclear spin and $\underline{e}_r$ the unit vector connecting the two spins. The combined hyperfine interaction can be written as

$$\hat{H}_\mathrm{hf} = \underline{\hat{S}}\mathbf{A}\underline{\hat{I}}, \tag{1.8}$$

with hyperfine tensor $\mathbf{A}$.

The total Hamiltonian of the NV with a ^{14}N nuclear spin is given by

$$\hat{H} = D\hat{S}_z^2 + E(\hat{S}_x^2 + \hat{S}_y^2) - \gamma_e \underline{\hat{S}} \cdot \underline{B} + Q\hat{I}_z^2 + \gamma_n \underline{\hat{I}} \cdot \underline{B} + \underline{\hat{S}}\mathbf{A}\underline{\hat{I}}. \tag{1.9}$$

1.2.4. Single shot readout of nuclear spins

As we have seen in section 1.2.2, the optical readout of the electron spin also destroys its state due to polarization. The detected signal is the relative fluorescence rate, which only yields qualitative information on the electron spin state. Here, we will discuss optical single shot readout of nuclear spins [82, 41, 42], and the influence of the electronic dynamics during readout onto the nuclear spin.

Readout of nuclear spins is achieved by correlating the electron spin state with the nuclear spin, and optical readout of the electron spin [36]. For strongly coupled nuclear spins, where the hyperfine splitting is larger than the linewidth of the electron spin transition, this correlation is created by a frequency selective electron spin π pulse. This pulse flips the state of the electron spin conditional on the nuclear spin state, which is a C_nNOT_e gate. The quantum logic readout sequence is shown in fig. 1.4c. It is important to note that for the readout laser pulse, the number of detected photons is either according to the distribution for $m_S = 0$ (bright distribution) or for $m_S = \pm 1$ (dark distribution), and the wavefunction of the nuclear spin collapses onto the corresponding eigenstate. The average number of detected photons $\langle n \rangle$ per readout pulse is up to $\langle n \rangle \approx 0.1$ for $m_S = 0$ and $\langle n \rangle \approx 0.07$ for $m_S = \pm 1$, with a standard deviation $\sigma = \sqrt{\langle n \rangle}$ according to the Poisson distribution. This means that there is a large overlap of the two distributions, such that state determination after one readout pulse is not possible. While the electron spin state is destroyed during readout, we will see below that for an appropriate external magnetic field and position of the nucleus relative to the NV the nuclear spin eigenstates can be robust against the optical readout of the electron spin. In this case, the nuclear spin state survives the readout process, and stays in its initial state, while the electron spin is re-initialized into $m_S = 0$. Therefore, another application of the nuclear readout sequence will yield a number of detected photons with the same statistical distribution (bright or dark) as for the first readout step. By applying repetitive readout of the nuclear spin, the random numbers of detected photons with always the same distribution are summed up. Consequently, the relative standard deviation $\sigma / \langle n \rangle$ is reduced, such that eventually the dark and bright distributions are well separated and single shot state determination is possible.

Fig. 1.4a shows a fluorescence time trace of the NV during repetitive readout of the ^{14}N nuclear spin within a magnetic field of ≈ 0.62 T. There, low fluorescence corresponds to the $m_I = +1$ nuclear spin state, and high fluorescence to $m_I = 0, -1$. As we can

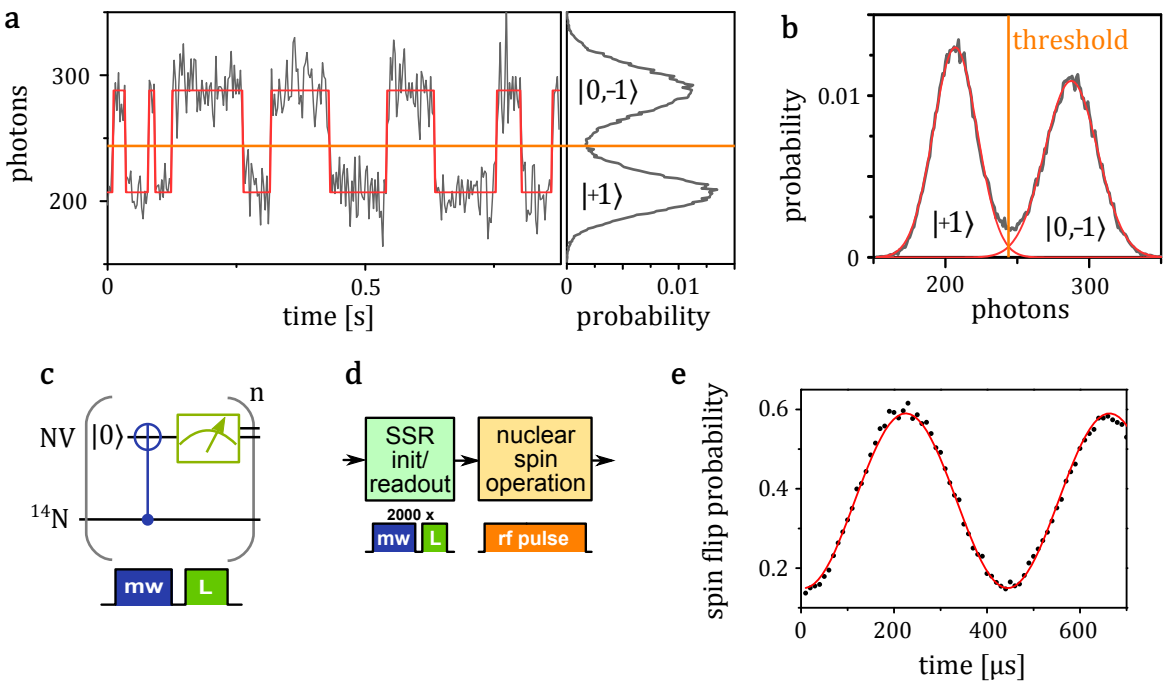

Figure 1.4.: Nuclear spin single shot readout. **a**, Fluorescence time trace of the NV during repetitive readout of the ^{14}N nuclear spin and corresponding histogram. These measurements were performed with a solid immersion lens, increasing the detected fluorescence by a factor of ≈ 3 (see section 4.2). The red line is the most likely state evolution obtained by a hidden Markov model [83]. The orange line shows the threshold for single shot readout. **b**, Histogram of the fluorescence time trace. The red lines are Gaussian fits. **c**, Measurement sequence for nuclear spin readout. **d**, Measurement sequence for nuclear spin operations with single shot readout. **e**, Rabi oscillation of the ^{14}N nuclear spin measured by single shot readout.

see, the lifetime of the nuclear spin states is much longer than the time needed for state determination, which enables single shot readout. Fig. 1.4b shows a histogram of measurement results for this time trace. The two peaks correspond to the two nuclear spin states $m_\mathrm{I} = +1$ and $m_\mathrm{I} \neq +1$ (i.e. $m_\mathrm{I} = 0, -1$). Placing a threshold between these two peaks allows for state determination of a single measurement point in the time trace, by checking whether the number of photons is below or above this threshold. Due to the overlap of the two distributions, the readout fidelity F will be limited, here it is $F = 0.958$. This projective, single shot readout is also used for initialization of the nuclear spin. Thereby, the initialization fidelity can be increased by shifting the threshold to lower photon count numbers. This will remove results which are likely wrong (cf. fig. 1.4b), at the expense of successful initialization events. A typical measurement sequence for Rabi oscillation of the nuclear spin is shown in fig. 1.4d. Two consecutive single shot measurements are correlated by taking the average result of the second measurement, if the first measurement yielded e.g. state $m_\mathrm{I} = +1$. Thereby, the effect of the rf pulse in between these two measurements is obtained. Fig. 1.4d shows the spin flip probability of the ^{14}N nuclear spin during resonant rf irradiation measured by single shot readout.

The lifetime of nuclear spins during optical readout is limited by interactions with the electron spin. The hyperfine interaction can be split into two parts, which lead to two different flipping mechanisms of the nuclear spin. The first part are A_{xx} and A_{yy} terms of the hyperfine tensor in (1.8), which leads to S_+I_+, S_+I_-, S_-I_+, S_-I_- terms in the Hamiltonian. These lead to mixing of electron and nuclear spin states, i.e. if we consider the $m_\mathrm{S} = 0, -1$ electron spin states and a nuclear spin 1/2 with states $m_\mathrm{I} = -, +$, the eigenstates can be written as $\alpha_i \left|m_\mathrm{S} = 0, m_\mathrm{I} = \pm\right\rangle + \beta_i \left|m_\mathrm{S} = -1, m_\mathrm{I} = \pm\right\rangle$, with different prefactors α_i, β_i for each eigenstate. After each readout laser pulse, the electron spin is polarized into $m_\mathrm{S} = 0$, which is not an eigenstate due to the mixing. Thus, the electron and nuclear spin states will coherently evolve, effectively destroying the nuclear spin state. The flipping rate r_1 due to this mechanism scales inversely quadratically with the electron Zeeman splitting $\gamma_e B$ [41, 42],

$$r_1 \propto \approx \frac{2A_\perp^2}{2A_\perp^2 + (D_i - \gamma_e B)^2}, \tag{1.10}$$

where $A_\perp = (A_{xx} + A_{yy})/2$, D_i the electron zero-field splitting for ground state or excited state, and B the magnetic field aligned along the NV axis. The second part are the A_{zx} and A_{zy} terms of the hyperfine tensor. These terms lead to nuclear spin eigenstates which depend on the electron spin state. Thus, whenever the electron spin flips, the nuclear spin will start to evolve in the new eigenbasis, effectively destroying its state. The flipping rate r_2 due to this mechanism will scale inversely quadratically with the nuclear Zeeman splitting $\gamma_n B$ [42],

$$r_2 \propto \approx \frac{A_{zx}^2 + A_{zy}^2}{A_{zx}^2 + A_{zy}^2 + (A_{zz} - \gamma_n B)^2}. \tag{1.11}$$

Usually, the flipping rate r_2 will be the dominant one, as it scales with the nuclear Zeeman splitting, contrary to r_1 which scales with the much larger electron Zeeman splitting. However, the A_{zx} and A_{zy} terms are highly position dependent. Specifically, these terms are zero for nuclear spin positions on the axis of the NV and for positions on the equatorial plane of the electron spin. Thus, for the ^{14}N nuclear spin, the dominant flipping mechanism is spin state mixing [41].

1.3. Spin dynamics

The spin is an intrinsic angular momentum of a particle, which results from relativistic quantum mechanics [84]. Associated with the spin is a magnetic moment

$$\underline{\mu} = g_{\mathrm{S}} \frac{q}{2m} \underline{S}, \tag{1.12}$$

where $\underline{S}$ is the particle's spin, q its charge, m its mass, and g_{S} the so called spin g-factor. Due to this magnetic moment, the spin states interact with magnetic fields, see section 1.2.3. Besides the energy splitting within a static magnetic field, time-dependant fields perpendicular to the spin orientation lead to spin rotations. For a spin oriented in z direction and an oscillating field $B_x \cos(\omega t)$ in x direction the Hamiltonian reads

$$\hat{H} = -\gamma_e B_z \hat{S}_z - \gamma_e B_x \cos(\omega t) \hat{S}_x. \tag{1.13}$$

By setting the Lamor frequency $\omega_{\mathrm{L}} = -\gamma_e B_z$, the detuning $\Delta = \omega_{\mathrm{L}} - \omega$ and the Rabi frequency $\Omega_{\mathrm{R}} = -\gamma_e B_x$, we rewrite the Hamiltonian as

$$\hat{H} = \underbrace{\omega \hat{S}_z}_{\hat{H}_0} + \underbrace{\Delta \hat{S}_z + \frac{\Omega_{\mathrm{R}}}{2} (\mathrm{e}^{\mathrm{i}\omega t} + \mathrm{e}^{-\mathrm{i}\omega t}) \hat{S}_x}_{\hat{H}_1}, \tag{1.14}$$

where we used $\cos(\omega t) = \mathrm{e}^{\mathrm{i}\omega t} + \mathrm{e}^{-\mathrm{i}\omega t}$. This is transformed from the Schrödinger picture $|\psi_{\mathrm{S}}\rangle$ into the interaction picture $|\psi_{\mathrm{I}}\rangle$ by $|\psi_{\mathrm{S}}\rangle = \hat{U} |\psi_{\mathrm{I}}\rangle$ with $\hat{U} = \exp(\mathrm{i}\omega \hat{S}_z)$. The effective Hamiltonian in the interaction picture is $\hat{W} = \hat{U}^\dagger \hat{H}_1 \hat{U}$, which yields in matrix representation

$$\hat{W} = \frac{1}{2} \begin{pmatrix} \Delta & \Omega_{\mathrm{R}} \\ \Omega_{\mathrm{R}} & -\Delta \end{pmatrix} + \frac{1}{2} \begin{pmatrix} 0 & \Omega_{\mathrm{R}} \mathrm{e}^{2\mathrm{i}\omega t} \\ \Omega_{\mathrm{R}} \mathrm{e}^{-2\mathrm{i}\omega t} & 0 \end{pmatrix}, \tag{1.15}$$

where the last term is neglected in the rotating wave approximation. In the resonant case, $\Delta = 0$, the Hamiltonian $\hat{W}$ (1.15) leads to rotations between the two spin states around the x-axis on the Bloch sphere with frequency Ω_{R}. This mechanism is used for the implementation of quantum gates, e.g. a NOT gate corresponds to a π rotation, and a Hadamard gate to a $\pi/2$ rotation. Note that these rotations will also induce additional, yet insignificant phase factors compared to the ideal gate operation. The rotation axis can also be changed by adjusting the phase ϕ of the field $B_x \cos(\omega t + \phi)$, leading to a rotation around the axis $(x, y, z) = (\cos(\phi), \sin(\phi), 0)$. In this work, the total rotation is denoted by θ_ϕ, where θ is the rotation angle and ϕ the rotation axis. In the case of off-resonant driving, $\Delta \neq 0$, the rotation axis becomes $(x, y, z) = (\Omega_{\mathrm{R}}, 0, \Delta)$, and the effective Rabi frequency $\Omega'_{\mathrm{R}} = \sqrt{\Omega_{\mathrm{R}}^2 + \Delta^2}$.

1.3.1. Spin decoherence

The destructive effect of the environment onto a quantum state can be split into the two parts, longitudinal relaxation and transversal relaxation [85]. The longitudinal relaxation refers the relaxation of the state populations (i.e. the diagonal elements of the density operator) into an equilibrium state, which is accompanied by energy exchange with the environment. It can be measured by initialization of the system and observation of the subsequent decay, and the timescale of the decay is denoted as the T_1 time. For NV^- in bulk diamond at room temperature, the T_1 of the electron spin is typically several ms.

Transversal relaxation, which leads to dephasing, refers to relaxation of coherences (i.e. off-diagonal elements of the density operator) towards zero. It is generated by interactions with the environment which either influence the energy levels of the system or create entanglement. We distinguish between inhomogeneous dephasing and homogeneous dephasing. Inhomogeneous dephasing is caused by quasi-static changes of the energy levels, which differ for separate experimental runs, but are static during one experimental run. Note that here, we consider the signal of a single system averaged over time / many experimental runs, i.e. a so called temporal ensemble. This leads to inhomogeneous line broadening in the resonance spectrum, cf. fig. 1.3d. This dephasing can be measured by a free induction decay, also called Ramsey interferometry, and is referred to as the T_2^* time. The measurement sequence is shown in fig. 1.5a. An initial $\pi/2$ pulse creates coherences, which then evolve during the free evolution time. In the rotating frame of the control field, the evolution frequency is the detuning. The second $\pi/2$ pulse maps the accumulated phase onto state population for readout. An example experiment is shown in fig. 1.5b. Here, the electron spin is hyperfine coupled to the ^{14}N nuclear spin (spin $I = 1$, coupling strength 2.165 MHz) and an additional ^{13}C nuclear spin (spin $I = \frac{1}{2}$, coupling strength 0.75 MHz), leading to a beating of six frequencies in the interferometry signal. A fast Fourier transformation unravels the six lines, and the linewidth corresponds to the T_2^* time.

For Ramsey interferometry the dephasing is caused by the quasi-static fluctuations of the detuning, which leads to fluctuations in the phase accumulation. The unknown phase can be re-focused by application of a π pulse in the middle of the free evolution time of the Ramsey sequence. The control sequence of this so-called Hahn echo is shown in fig. 1.6a. Effectively, this π pulse changes the phase ϕ_1 accumulated so far to $\phi' = \pi - \phi_1$. If the detuning stays constant, another phase $\phi_2 = \phi_1$ is accumulated, leading to a total phase of π, which is independent of ϕ, and therefore independent of the detuning. However, if the energy levels of the system are time-dependent due to fluctuations of the environment (on the timescale of the experiment), then $\phi_2 \neq \phi_1$, thus resulting in dephasing. Another effect for decoherence is entanglement of the system with the environment when the environmental dynamics depend on the state of the system, effectively measuring its state [86]. An example Hahn echo experiment is shown in fig. 1.6b. This field of phase refocussing techniques is called dynamical decoupling, i.e.

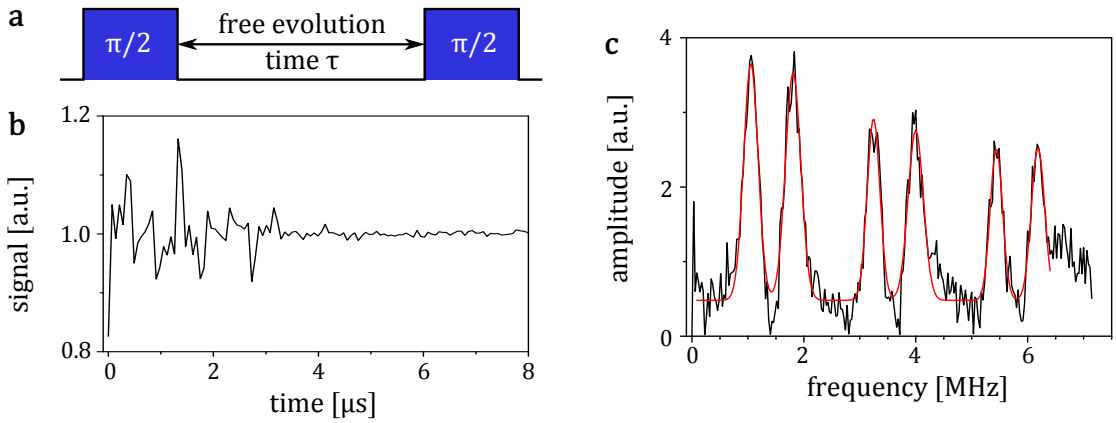

Figure 1.5.: Ramsey interferometry. **a**, Experimental sequence for electron spin control. Note that electron spin initialization and readout is performed via illumination and fluorescence, see fig. 1.3c. **b**, Ramsey interferometry of the electron spin for a natural NV in natural type IIa diamond. The Rabi frequency for the control pulses is $\approx$ 11 MHz. The frequency of the control field was set to 1 MHz besides the spectrum. **c**, Fast Fourier transformation of the signal shown in b. The red line is a multi-peak Gaussian fit. The linewidth (full width half maximum) is 303 kHz.

decoupling the dynamics of a system from its environment. Higher order decoupling can be achieved by e.g. implementing more π pulses or more complex refocussing sequences [87, 88, 89, 90].

1.3.2. Optimal control

As we have seen in the previous section, well designed control sequences on a quantum system can effectively decouple its dynamics from fluctuations of the environment. A more general approach for such a task is optimal control [91, 92]. In optimal control, the control sequence applied to the system is optimized numerically for a given task. This task can be defined very broadly, however, one needs a figure of merit (a so-called quality function) for how well the task is implemented by a control sequence. Typical examples would be to reach a desired final state, or to implement a certain gate operation, and the figure of merit for these tasks would be the fidelity between actual and ideal implementation. Environmental fluctuations are included by appropriate variables in the Hamiltonian or master equation of the system. By optimizing the task for a certain range of these variables, robustness with respect to the corresponding fluctuation can be achieved.

For example, we want to implement the operation $\hat{U}_{\text{ideal}}$ robust against the detuning (inhomogeneous line broadening) and fluctuations of the control field strength. First, we need to define the Hamiltonian or master equation describing the dynamics of the system. The control sequence is described by control terms/operators B_i with discretized

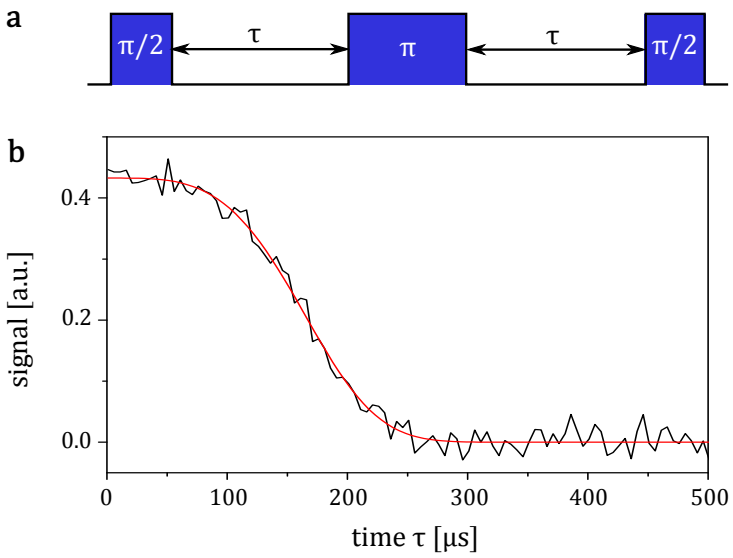

Figure 1.6.: Hahn echo. **a**, Experimental sequence for electron spin control. Here, readout was performed via single shot readout of the ^{14}N nuclear spin, cf. section 1.2.4. **b**, Hahn echo of the electron spin at a magnetic field of $\approx$ 6000 Gauss, thus suppressing ^{13}C collapses [37]. The measurement were performed in diamond created by chemical vapor deposition with an NV created by electron irradiation and annealing. The Rabi frequency for electron spin control was 1.88 MHz, the ^{14}N nuclear spin was polarized. Here, for each τ two measurements were performed, with final $(\pi/2)_0$ and $(\pi/2)_\pi$ pulse, and the results subtracted. The red fit is the function $A*\exp(-(\tau/T_2)^p)$, with $T_2 = 179$ μs, $p = 3.7$, $A = 0.43$.

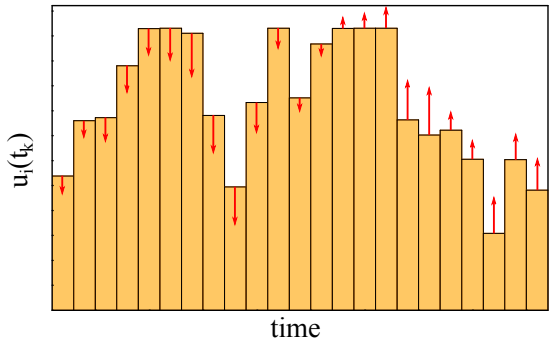

Figure 1.7.: Illustration of optimal control and update step for optimization. A possible update step for the $u_i(t_k)$ is indicated by the red arrows.

evolution of control strength $u_i(t_k)$ for duration τ_k, cf. fig. 1.7. Additionally, experimental restrictions regarding e.g. the control strength u_i are implemented. Then, the range of the detuning and control field strength, for which the operation should be implemented optimally, is defined. The quality function is the fidelity F, which is summed over the defined range of the fluctuating variables, with $F = \mathrm{Tr}(\hat{U}^{\dagger}_{\mathrm{ideal}}\hat{U})$, where $\hat{U}$ is the actual operation calculated from the control sequence and the Hamiltonian. At the heart of optimal control is the optimization of the quality function with the controls $u_i(t_k)$. There are different approaches for optimizing the fidelity [91, 92, 93]. In this work, we use gradient ascent pulse engineering (GRAPE) [91, 92]. There, the fidelity for a certain control sequence is calculated by the forward and backward evolution of the system, and optimized by calculating the gradient of the fidelity with respect to the control strengths $u_i(t_k)$. For GRAPE, the update steps are concurrent, i.e. all $u_i(t_k)$ are updated simultaneously, see fig. 1.7.

2. Photo-ionization of the NV

After the invention of single shot readout with the NV [41], it was for the first time possible to directly measure occupation probabilities of different NV states, while previously only indirect state measurement via the NV's fluorescence rate was possible. In [41], Rabi oscillations of the ^{14}N nuclear spins were driven, and the spin flip probability measured by single shot readout. However, the maximally measured flip probability was only around 67 %. This indicated that the electronic state of the NV is not always initialized: Because the transition frequency of the nuclear spin depends on the electronic state of the NV (due to hyperfine interaction), state manipulations of the nuclear spin with radio frequency (rf) fields are usually conditional on the electronic state. Only if the current transition frequency is in resonance with the rf, the nuclear spin will be rotated. In section 2.1, we will show that due to photo-ionization, the NV is in its desired negative charge state with only ≈ 75 % probability for typical measurement conditions.

Previous studies have shown that photo-ionization of the NV between its negative and neutral charge state can occur [94, 95, 96, 97, 98]. In these studies, the charge state occupations were only measured indirectly via spectrally resolving the NV's fluorescence, and cannot explain the above described reduced Rabi contrast. In section 2.2, we will introduce a new method for single shot, projective charge state detection of a single NV. With this method, we perform detailed studies of the ionization and recombination dynamics, and their dependency on illumination wavelength and power, see section 2.3. These results allow us to obtain the absorption spectrum of the NV (section 2.3.1), the population of NV^- depending on the illumination wavelength (section 2.3.2), and the energy of the NV^- ground state within the diamond band gap (section 2.3.3). By exploiting this new knowledge of the NV's photo-physics, we can improve the optical polarization of the NV^- electron spin (section 2.4).

The results of sections 2.1, 2.2, 2.3 are published in [43, 47].

2.1. Detection of NV^0 via single shot NMR

As explained in the introduction, the transition frequency of the ^{14}N nuclear spin depends on the electronic state. By applying frequency selective rf pulses, the state of the nuclear spin can be changed conditional on the electronic state. We can therefore probe the occupation probabilities of different electronic states, by using single shot readout of the nuclear spin. Note that the nuclear spin readout mechanism only works in NV^-.

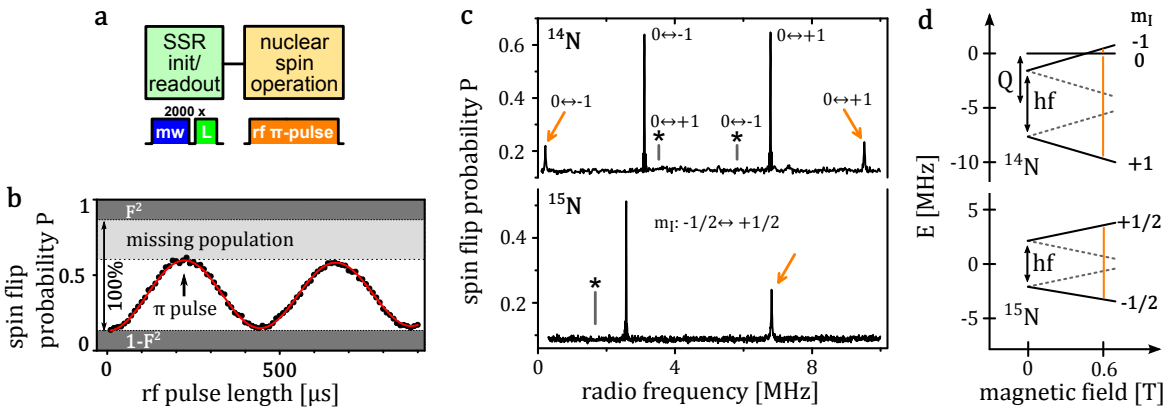

Figure 2.1.: NMR based electronic state detection. **a**, Measurement sequence (see text). **b**, Rabi oscillations of the ^{14}N nuclear spin, conditional on the $m_S = 0$ NV$^-$ ground state. The contrast is reduced symmetrically due to the limited single shot readout fidelity F. **c**, NMR spectra of the ^{14}N and ^{15}N nuclear spins, within a magnetic field of around 6000 Gauss. The stars indicate the expected, but missing lines. **d**, Energy level scheme of the ^{14}N and ^{15}N nuclear spins in NV^0. The solid lines and the dashed lines are for different m_S states.

As we will see later, probing of other charge states is nevertheless possible, because the green readout laser pulse induces rapid charge state switching. Whenever the NV is in the negative charge state, the nuclear spin readout will work. Additionally, the possibility of performing nuclear spin single shot readout shows that the nuclear spin state is robust against ionization of the NV. Fig. 2.1a shows the sequence used for these measurements. First, a projective single shot measurement initializes the nuclear spin. Then, the frequency selective rf π-pulse is applied, and a second single shot measurement (which also initializes the next measurement repetition) is used to determine if the spin was flipped. Fig. 2.1b shows Rabi oscillations of the ^{14}N nuclear spin, conditional on the $m_S = 0$ NV$^-$ ground state. Taking into account the reduced contrast due to the limited readout fidelity, we can estimate the population of the $m_S = 0$ NV$^-$ ground state to ≈ 70 %. This indicates that the NV is with ≈ 30 % probability in a different state, which we refer to as "missing population".

Detection of unknown state with NMR To gain more knowledge of the missing population of the NV, we measured broad range NMR spectra, for both ^{14}N and ^{15}N , which are shown in fig. 2.1c. For ^{14}N , the spin was initialized in $m_I = 0$, to see both transitions $m_I = 0 \leftrightarrow -1$ and $m_I = 0 \leftrightarrow +1$. The large peaks correspond to transitions in the $m_S = 0$ NV$^-$ ground state. There are no peaks at the transition frequencies corresponding to the $m_S = -1, +1$ states, indicating a high degree of spin polarization in the NV$^-$ ground state. Note that the intensity of these peaks could also be reduced due to differing hyperfine enhancement of the different m_S states. Therefore,

Rabi oscillations at these frequencies were measured separately and showed, indeed, small population < 5 % for each of these states, cf. section 2.4. However, we find new peaks corresponding to yet unknown electronic states (orange arrows in fig. 2.1c). By initializing ^{14}N into $m_I = +1$ or -1, we can assign the two possible transitions mentioned above to the two peaks. The Hamiltonian for the nuclear spin is

$$\hat{H}_n = Q\hat{I}_z^2 + \underline{B} \cdot \underline{\hat{I}} + \hat{H}_{hf}, \tag{2.1}$$

with three terms for the quadrupole splitting ($Q\hat{I}_z^2$, zero for spin $\frac{1}{2}$), nuclear Zeeman interaction ($\underline{B} \cdot \underline{\hat{I}}$), and hyperfine interaction ($\hat{H}_{hf}$). The quadrupole splitting depends on the NV's electronic charge state and wave function, and the hyperfine interaction on the electron wave function and spin state. The Zeeman interaction only depends on the external field, which is known. From the new peaks in fig. 2.1c, we can calculate both the quadrupole splitting Q and the hyperfine interaction for both ^{14}N and ^{15}N , see fig. 2.1d. For ^{14}N , the observed hyperfine splitting is $\Delta_{14N} = 3.03$ MHz and the quadrupole splitting is $Q = -4.654$ MHz. For ^{15}N , we find $\Delta_{15N} = 4.242$ MHz. In the case of $|m_S| = \frac{1}{2}$, the hyperfine coupling constants a with $\Delta = a m_S m_I$ are $|a_{14N}| = 6.06$ MHz for ^{14}N and $|a_{15N}| = 8.484$ MHz for ^{15}N . Most interestingly, only nuclear spin transitions corresponding to one orientation of the electron spin in the unknown NV state can be observed, even though the unknown state is not $S = 0$, because of the observed hyperfine interaction. Recent experiments indicate that this is not due to polarization of the electron spin, but due to some unknown mechanism that prevents driving Rabi oscillations of the nitrogen nuclear spin on these transitions, and that this mechanism is magnetic field dependent. However, this behavior needs to be analyzed in more detail.

Optical pumping into unknown state Recently, a long-lived dark state of the NV was discovered [99]. By applying red illumination (637 nm), initial fluorescence of the NV will decay, pumping the NV into a dark state, see fig. 2.2a. Here, we show that this dark state is the same as the above discovered new unknown state. We measure the population of the $m_S = 0$ NV^- ground state and of the unknown state, while pumping the NV into the dark state by red illumination. For this, we monitor the NMR transitions lines of both states (cf. fig. 2.1c), after applying red laser pulses with varying length. Fig. 2.2c shows that red illumination pumps the NV into the unknown state, which is, in fact, the dark state. From the spectra shown in fig. 2.2c, we can also see that the transition corresponding to the $m_S = 0$ NV^- ground state exhibits a typical Fourier transformed line shape due to the rectangular rf π-pulse, whereas the transition of the unknown state has a broad Lorentzian shape (full width at half maximum (FWHM) of ≈ 33 kHz), indicating very short nuclear spin coherence times. Indeed, fig. 2.2e shows Rabi oscillations of the nuclear spin in the unknown state, with very short coherence time of $T_2 = T_2^* \approx 6\mu$s due to homogeneous dephasing. Homogeneous dephasing can be deduced from the fact that the spin flip probability converges to 0.5 independent of

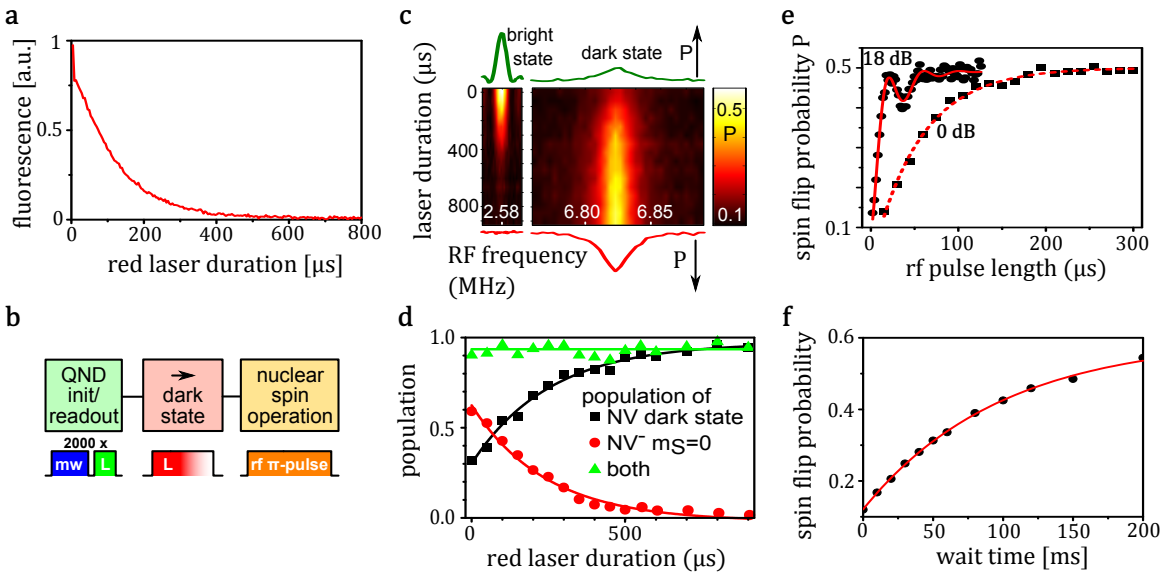

Figure 2.2.: Pumping into unknown dark state. **a**, NV fluorescence during red illumination (637 nm). Before the start of each red pulse, a green laser pulse (532 nm) was used to restore the initial state. **b**, Pulse sequence for characterizing pumping into unknown state (c, d, e). After initialization of the nuclear spin, a red pulse with variable length pumps into dark state. With the NMR operation, the populations of the $m_S = 0$ NV^- ground state and of the unknown state are probed. **c**, Intensity of NMR transition lines in the $m_S = 0$ NV^- ground state and in the unknown state, depending on the duration of the red pump laser. **d**, Calculated populations (see text) of the $m_S = 0$ NV^- ground state and the unknown state from the data shown in c. The red and black lines are exponential fits, and the green line is the mean value of the green data points. **e**, Rabi oscillations with different rf powers (18 dB difference) of the nuclear spin in the unknown state. Red lines show fits with homogeneous dephasing. **f**, Nuclear spin flip probability after pumping into the unknown state, with exponential fit. The sequence is similar as shown in b, but instead of the nuclear spin operation, a variable waiting time was introduced.

the driving Rabi frequency, which cannot be explained by inhomogeneous dephasing. The mechanism of this dephasing can be explained by fluctuations of the transition frequency during one experimental run (i.e. homogeneous fluctuations). Therefore, the nuclear spin flip probability converges to 50% of the electronic state population. A possible exception could be homogeneous dephasing due to electron spin flips in the unknown state. In either case, to calculate the population of the unknown state, the measured intensity of the NMR transition line in the unknown state has to be multiplied by a factor of 2, whereas the population of the different spin states in the unknown state cannot be determined. Taking this into account, we can calculate the electronic state populations p from fig. 2.2c with

$$p = \frac{y - F^2}{1 - 2F^2}, \tag{2.2}$$

where y is the measured spin flip probability (multiplied by an additional factor of 2 for the unknown state) and F the single shot readout fidelity (cf. fig. 2.1b). The populations are shown in fig. 2.2d. We can see that nearly all of the population is either in the $m_S = 0$ NV^- ground state or in the unknown state. In addition to the very short nuclear spin coherence time in the unknown state, also the nuclear spin T_1 time (≈ 90 ms, see fig. 2.2f) is much shorter than in the NV^- ground state ($T_1 \approx 800$ ms, [41]). In the same manner, also the lifetime of the unknown electronic state can be measured, by initializing the NV in the unknown state, and measuring the intensity of the NMR transition after a waiting time. Even for a waiting time of 50 ms, no decay of the intensity was visible, meaning that the lifetime of the unknown state is $\gg 50$ ms.

In the following, we will further investigate the pumping process into the unknown state, to gain more knowledge about it. For this, we studied the power dependence of both the pumping rate into the unknown state under red illumination (637 nm), and the repumping rate into the NV^- ground state under green illumination (532 nm). The pumping rate into the unknown state is measured via the exponential decay of the NV fluorescence during a red laser pulse (cf. fig. 2.2a). Similar to this, the NV fluorescence shows an increase during a green laser pulse, if it is initially in the unknown state. Fig. 2.3a shows the pumping and repumping rate in dependence of the red and green laser power, respectively. For low laser powers, the rates increase quadratically with the applied laser power, indicating two-photon processes. For high laser powers, the rates increase linearly with the applied laser power. This behavior can be explained by pumping and repumping processes via excited states. For such a model, the interconversion rate r is given by the product of the population p_e of the corresponding excited state, and the applied laser power I,

$$r \propto p_e I = \frac{I^2}{I + I_0}, \tag{2.3}$$

where $p_e = \frac{I}{I+I_0}$ describes the saturation of the excitation process with increasing laser power. The measured rates can be explained by eq. (2.3), which is used to fit the data

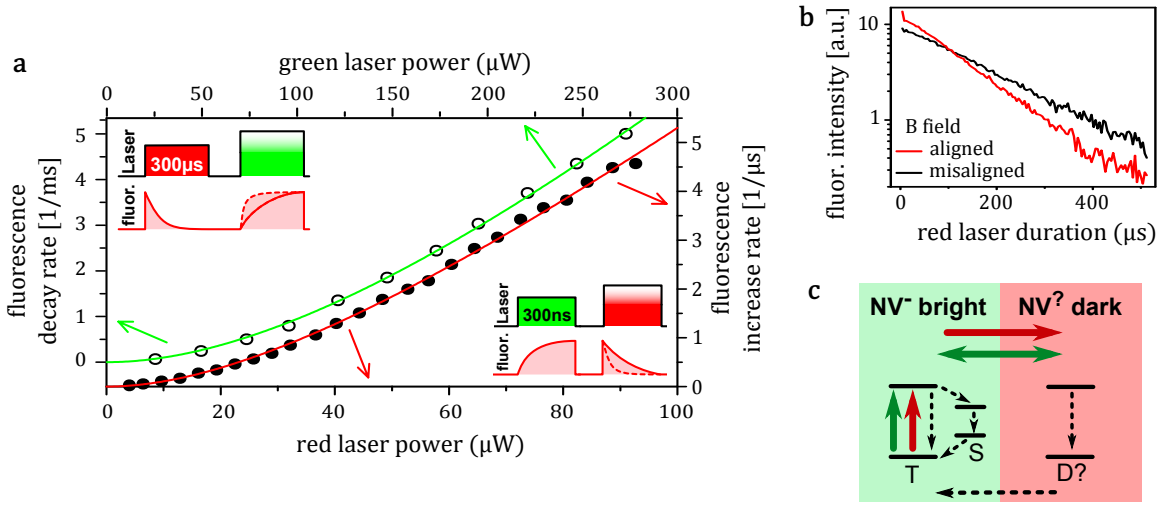

Figure 2.3.: Model for pumping process. **a**, Power dependence for pumping into unknown state under red illumination, and repumping into NV^- ground state under green illumination. The insets show the pulse sequences: First a red or green laser pumps initializes the NV in the unknown state or the NV^- ground state, and pumping and repumping rates are obtained from the fluorescence evolution during the following green or red laser pulse with variable power. The solid lines show fits, see text. **b**, Fluorescence decay during red illumination with aligned and misaligned magnetic field. **c**, Model of the interconversion between NV^- ground state and unknown state. To pump the NV into the unknown state, NV^- has to be excited first. For the repumping into the NV^- ground state, a similar process occurs: First the unknown state has to be excited, and can then be brought to the NV^- ground state by a second photon.

in fig. 2.3a.

Further evidence that the repumping process goes via the NV^- excited state can be obtained by exploiting the spin state dependent inter-system crossing of NV^-. Due to this inter-system crossing, the steady-state population of the excited state depends on the electron spin state. However, the optical cycle of the NV leads to polarization of the electron spin. Therefore, to change the steady-state population of the excited state via the inter-system crossing, continuous changing of the electron spin state is required. This can be achieved by applying a misaligned magnetic field, which mixes the spin states, and leads to constant evolution between the states (cf. section 1.2.4) [100]. Fig. 2.3b shows the fluorescence decay during red illumination (i.e. pumping from NV^- ground state to unknown state), for an aligned and for a misaligned magnetic field. For the misaligned magnetic field, the pumping rate is reduced, which can be explained with eq. (2.3) by the reduced population of the excited state. Note that is analysis is only for the pumping process from NV^- ground state into the unknown state. In section 2.3 we will gain further insight into the repumping process. A schematic model for the interconversion between the two states is shown in fig. 2.3c.

Unknown state is NV^0 The data presented so far already provides strong indication that the unknown state is the ground state of the neutral charge state NV^0. The hyperfine coupling constants of the unknown state are similar to the hyperfine coupling constants in the NV^- ground state, indicating that the observed spin of the unknown state is in $e_{x,y}$ orbitals [81, 101]. In contrast, an unpaired electron spin in the $a_1(2)$ orbital would lead to an about one order of magnitude larger hyperfine interaction [102]. Additionally, the long lifetime of the unknown state indicates that it is not an excited state. Therefore, possible states are the NV^{2-} ground state or the NV^0 ground state, which both are $S = \frac{1}{2}$ states. The observed optical pumping into the unknown state can be explained by photo-ionization of NV^- via the NV^- excited state. The NV^- excited state is located ≈ 0.6 eV below the conduction band, such that red light (1.95 eV) would be enough to ionize this state [97]. Furthermore, photo-interconversion between NV^- and NV^0 has already been observed. These facts indicate that the unknown state is NV^0. However, in our case of a single NV, no spectral evidence of NV^0 could be detected.

Here, we will show further evidence that the unknown state is, indeed, NV^0. We find that illumination with blue light (440 nm) leads to NV^0 fluorescence, while suppressing fluorescence of NV^- (see fig. 2.4a). In section 2.3.3 we will see that this is due to one-photon ionization of NV^-. Again, we can use single shot NMR to probe the electronic state of NV^0. The sequence is shown in fig. 2.4b. For the laser pulse we either apply red illumination to pump into the unknown state or blue illumination to pump into NV^0, and for reference green illumination (532 nm, fig. 2.4c), As can be seen in fig. 2.4d, both red illumination and blue illumination populate the unknown state, showing that it is NV^0.

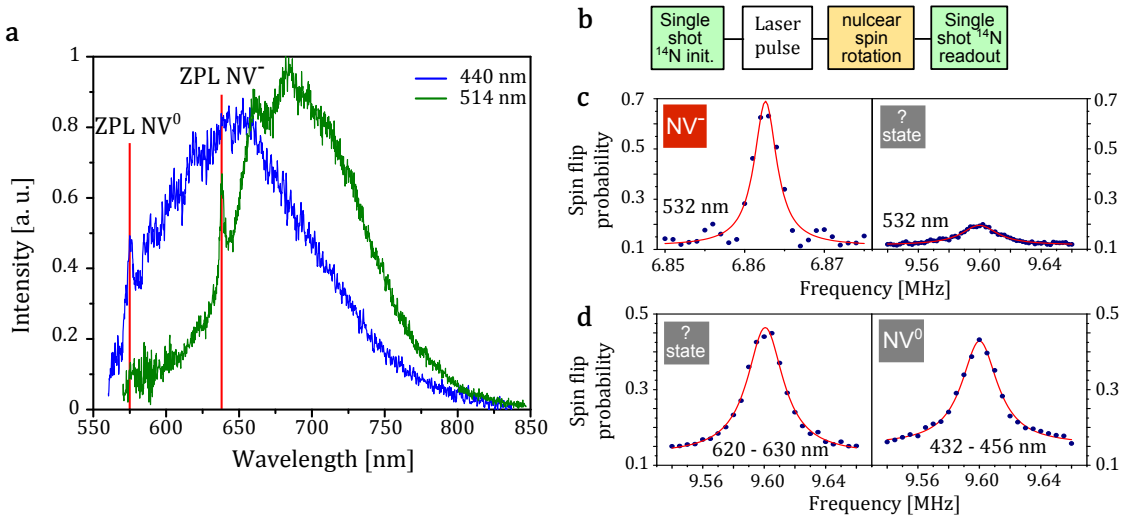

Figure 2.4.: Unknown state = NV^0. **a**, Spectrum of the NV fluorescence by excitation with green and with blue light. **b**, Pulse sequence for single shot NMR, used for c and d. **c**, NMR spectra of frequencies corresponding to NV$^-$ ground state and unknown state, with typically used green laser pulse (532 nm). The spectra here and in d are for the $m_I = 0 \leftrightarrow +1$ transition. **d**, NMR spectra for unknown state with red (620 - 630 nm, left side) and with blue (432 - 456 nm, right side) laser pulse. For 620 - 630 nm, the laser power was 20 μW and the pulse length 2 ms. For 432 - 456 nm, it was 20 μW for 10 ms. The red lines are Lorentzian fits.

2.2. Single shot charge state detection

In the previous section, we have seen that illumination of the NV leads to photo-induced ionization and recombination between NV$^-$ and NV^0. Additionally, the dark lifetime of NV^0 is very long ($\approx$ 150 s [99]), such that it can be considered as stable for most experiments. Under typical measurement conditions with green illumination, the NV is in its negative charge state NV$^-$ only with around 70% probability. In this section, we will present a new method to determine the current charge state of an NV with a single, projective measurement, which allows for pre-selection of experimental runs in NV$^-$. This method will also allow us to perform real-time monitoring of the NVs' charge state.

By illuminating the NV with laser light with less photon energy than the zero-phonon line of NV^0 (2.16 eV $\hat{=}$ 575 nm), NV^0 will hardly be excited (only due to thermal broadening) and does not seem to fluoresce. If, on the other hand, the photon energy is higher than the zero-phonon line of NV$^-$ (1.95 eV $\hat{=}$ 637 nm), fluorescence from NV$^-$ can detected. Therefore, under these conditions, detection of fluorescence indicates that the NV was, at some time during the illumination, in NV$^-$. Additionally, a long-pass

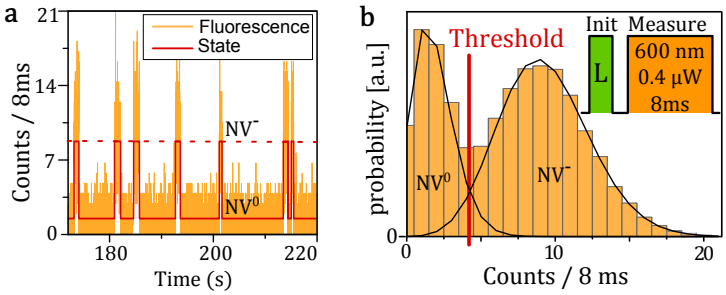

Figure 2.5.: Single shot charge state detection. **a**, Fluorescence time trace of the NV with orange (600 nm), 0.4 μW illumination. A hidden Markov model [83] was applied for the state fit, which shows the most likely fluorescence level evolution. For these conditions, the lifetime of NV^- is $\approx$ 600 ms. The steady state charge state population is around 0.9 : 0.1 for NV^0 : NV^- **b**, Histogram of measurement results for charge state detection under typical measurement conditions with the NV. The two peaks correspond to NV^0 and NV^-. As for single shot readout of the ^{14}N nuclear spin (see section 1.2.4), a threshold is placed between the two peaks for single shot charge state detection. The inset shows the measurement sequence: First, a green laser pulse creates the typical steady state distribution of around 0.3 : 0.7 for NV^0 : NV^-, and the NV fluorescence is measured during a second low power orange pulse (0.4 μW, 8 ms).

filter at 650 nm ensures that mainly fluorescence of NV^- can be detected. As we have seen in eq. (2.3), for low illumination power the ionization and recombination rates (r_{ion} and r_{re}, respectively) for the NV are quadratic to the applied laser power I,

$$r_{\text{ion}}, r_{\text{re}} \propto I^2. \tag{2.4}$$

On the other hand, the fluorescence rate r_{fl} of the NV is proportional to the population of the excited state, which is linear to the applied laser power (for low power),

$$r_{\text{fl}} \propto I. \tag{2.5}$$

The average number of photons, which we can detect from NV^- before it is ionized, i.e. the photons per burst n_{ppb}), is the product of the NV^- fluorescence rate with the lifetime $T_{\text{ion}} = \frac{1}{r_{\text{ion}}}$ of NV^- during illumination,

$$n_{\text{ppb}} \propto \frac{r_{\text{fl}}}{r_{\text{ion}}} \propto \frac{1}{I}, \tag{2.6}$$

i.e. n_{ppb} increases inversely with decreasing illumination power. Therefore, for very low illumination power it can be possible to obtain enough fluorescence from the NV to determine its charge state, before the current charge state is destroyed, which allows for real-time charge state monitoring and single shot charge state detection.

For these experiments we use a laser with 600 nm wavelength. Fig. 2.5a shows a fluorescence time trace of the NV during orange (600 nm), 0.4 μW laser illumination. The

two distinct fluorescence levels corresponding to NV^- (high fluorescence) and NV^0 (low fluorescence) are clearly distinguishable, i.e. the time needed to determine the current charge state is shorter than the lifetime. Therefore, real-time monitoring of the charge state is possible, and we can apply a hidden Markov model to the fluorescence data, to obtain the most likely charge state evolution [83], see 2.5a. Additionally, this allows us to perform single shot charge state detection, to measure e.g. the charge state populations under typical measurement conditions (532 nm illumination), see fig. 2.5b.

Optimal wavelength The maximum fidelity for single shot charge state detection is given by the number of photons per burst n_{ppb}, see eq. (2.6), which depends on the fluorescence of NV^- (higher is better), and the lifetime (longer is better). By reducing the excitation power, n_{ppb} can be increased. However, reducing the excitation power also decreases the fluorescence, which in turn increases the measurement time and is therefore limited by photon count noise (e.g. "dark counts"). This means that experimentally, not only n_{ppb} is important, but also the actual fluorescence rate r_{fl}. As can be seen from eq. (2.6) and eq. (2.5), any increase of n_{ppb} leads to a decrease of r_{fl}. Another possible parameter to change besides the excitation power is the excitation wavelength: Because of different dependencies on the excitation wavelength of the absorption cross-section of NV^- and of the cross-section for ionization, we can search for an optimal wavelength for charge state detection. This can be done using the data presented in section 2.3.1. The figure of merit c for charge state detection is then given by the product of n_{ppb} with r_{fl},

$$c = n_{\mathrm{ppb}} r_{\mathrm{fl}} = \frac{r_{\mathrm{fl}}^2}{r_{\mathrm{ion}}}. \tag{2.7}$$

For a given desired number of photons per burst n_{ppb}, the measurement time t can be determined by $t \propto n_{\mathrm{ppb}}/c$, i.e. high values for c are preferred. Note that c is power-independent for low illumination intensities. The wavelength dependence of c is shown in fig. 2.6. The maximum of c is at around 585 to 590 nm. For the following experiments with charge state detection, we will mostly use 595 nm light for the excitation, from a commercially available diode pumped solid state (DPSS) laser.

2.3. Wavelength dependent ionization dynamics

Recently, new studies were performed with single NVs at cryogenic temperatures, which provided new insight into the recombination process [103, 104]. It was shown that for the recombination process, first NV^0 is excited, and then a second photon captures an electron from the valence band to form NV^-. In the following, we will discuss the current understanding of the full cycle of two-photon ionization and recombination (see fig. 2.7). As shown in section 2.3.3, the one-photon ionization and recombination energies are

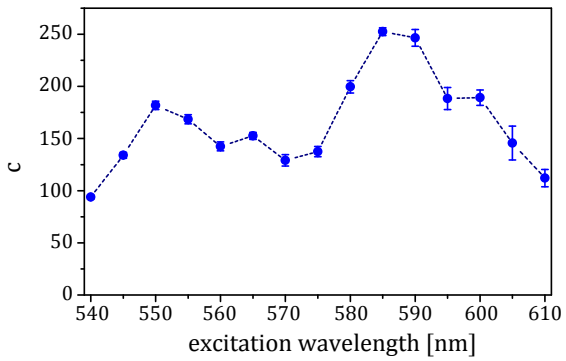

Figure 2.6.: Optimal wavelength for charge state detection. Wavelength dependence of figure of merit c as calculated from the data in fig. 2.9c, see text for description.

$\Delta_{\mathrm{ion},0} \approx 2.6$ eV and $\Delta_{\mathrm{re},0} \approx 2.94$ eV, respectively, i.e. here we only consider photon energies below 2.6 eV.

1. One photon excites NV^- into the excited state, which is $E_{\mathrm{NV-,ex}} = 1.95$ eV above the ground state, from where it can also decay to the ^{1}E metastable state.

2. A second photon excites one electron from the NV^- excited state into the conduction band, ionizing NV^- and forming NV^0. Another possibility is ionization from the NV^- ^{1}E metastable state, if the photon energy is high enough. The energy of this state is believed to be close to, but less than $E_{\mathrm{NV-,ms}} \lesssim 0.76$ eV above the ground state of NV^-[105, 80, 106, 77]. This leads to an ionization energy for the ^{1}E metastable state of $\gtrsim \Delta_{\mathrm{ion},0} - E_{\mathrm{NV-,ms}} = 1.84$ eV, i.e. this process could, in principle, happen. Another question is the state of NV^0 after the ionization of NV^-. The configuration of the NV^- excited state is a^1e^3, and removing one electron from the highest energy orbital (e) would lead to a a^1e^2 configuration, which is an excited state of NV^0. However, the remaining ionization energy of the NV^- excited state is $\approx \Delta_{\mathrm{ion},0} - E_{\mathrm{NV-,ex}} = 0.65$ eV. To end up in the NV^0 excited state ($E_{\mathrm{NV0,ex}} = 2.16$ eV above the ground state of NV^0), a photon with at least 0.65+2.16 eV = 2.81 eV ($\widehat{=}$ 441 nm) would be needed. The NV^0 metastable state is also an excited state, implying a similar minimum photon energy. Therefore, these energetic considerations imply that after the ionization of NV^-, NV^0 can only be in its ground state. In addition to promoting one electron to the conduction band for ionization from the NV^- excited state, another electron from the e orbital has to decay to the a orbital. This latter effect could possibly be an Auger process [104].

3. From the NV^0 ground state, one photon with energy $E \geq E_{\mathrm{NV0,ex}} = 2.16$ eV is absorbed to yield the NV^0 excited state.

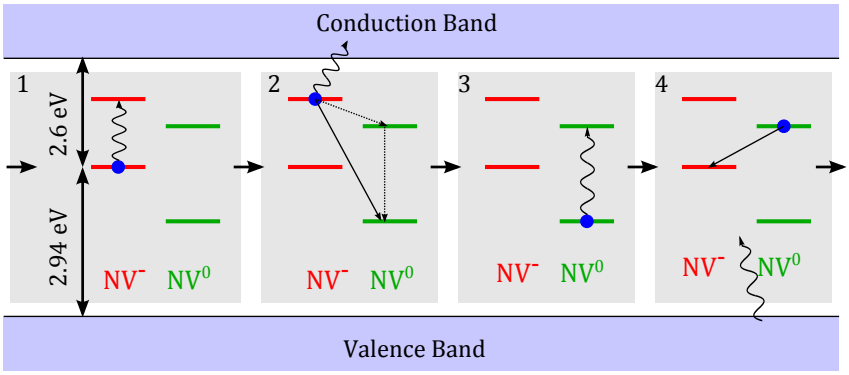

Figure 2.7.: Model for ionization and recombination. Illustration of the full cycle of photo-induced ionization and recombination of NV^- by two-photon processes. In both cases, first NV^- respectively NV^0 are excited by one photon, and a second photon excites one electron from the NV^- excited state into the conduction during ionization, respectively excites one electron from the valence band into the NV during recombination. See text for more detailed description.

4. Another photon promotes one electron from the valence band to the NV, forming NV^-. What is the final state in NV^-? From the NV^0 excited state, the remaining recombination energy is therefore $\approx \Delta_{\mathrm{re},0} - E_{\mathrm{NV0,ex}} = 0.78$ eV. To end up in the NV^- excited state, an energy of at least $\approx E_{\mathrm{NV-,ex}} + 0.78$ eV $= 2.73$ eV ($\hat{=}$ 454 nm) is necessary. To end up in the NV^- ^{1}E metastable state, the necessary energy is $\approx E_{\mathrm{NV-,ms}} + 0.78$ eV $\lesssim 1.54$ eV ($\hat{=}$ 805 nm). This means that we expect the NV to be in either the NV^- ground state or metastable state after recombination.

In this section, we will further investigate the wavelength dependence of the photo-induced ionization dynamics of the NV. These measurements will yield the wavelength dependence of the ionization and recombination rates, the intrinsic absorption spectrum of NV^- and the steady state population of NV^- in dependence of the illumination wavelength. Furthermore, we will determine the ionization and recombination energies of NV^-, which are also shown in fig. 2.7.

2.3.1. Charge state dynamics

As we have seen in section 2.2, low laser illumination of the NV allows for real-time monitoring of the charge state dynamics. Here, we use this method for illumination wavelengths of 540 to 610 nm, and analyse the observed charge state dynamics with a hidden Markov model. For shorter wavelengths, this analysis is not possible, because the difference of observed fluorescence rates between the NV^- and NV^0 states becomes severely reduced. For wavelengths longer that 610 nm, the recombination rate is too low to observe the dynamics, because NV^0 can hardly be excited. From the hidden Markov

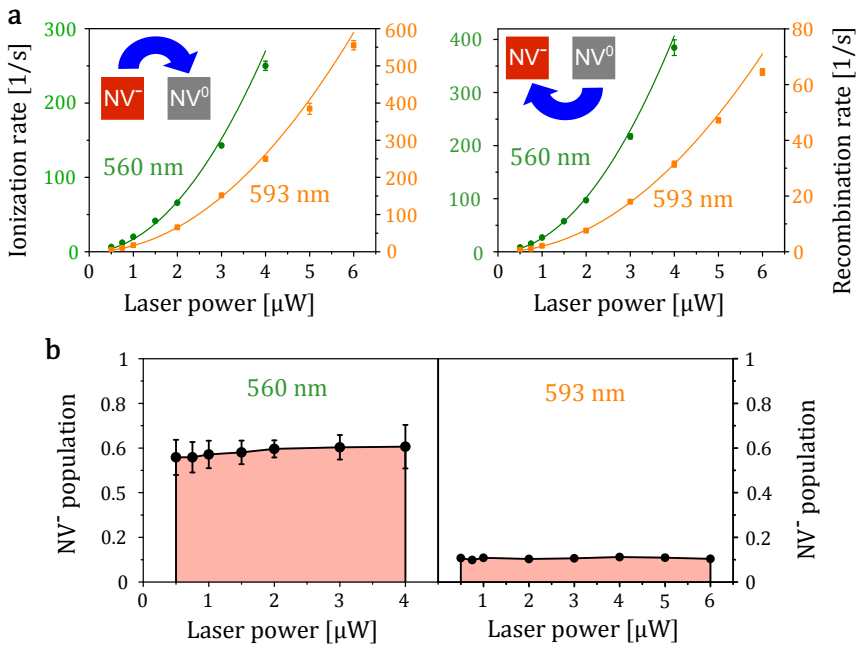

Figure 2.8.: Power dependence of charge state dynamics. **a**, Power dependence of the ionization and recombination rate for 560 nm and 593 nm laser illumination. The solid lines are quadratic fits for the rate $r = aI^2$, where I is the laser power. **b**, Average population of NV^- calculated by eq. (2.8).

model, we can obtain the detected fluorescence rates for both states, and the ionization and recombination rates. From the ionization and recombination rates (r_{ion} and r_{re}, respectively) we can also calculate the steady state population $p_{\mathrm{NV-}}$ of NV^- by

$$p_{\mathrm{NV-}} = \frac{r_{\mathrm{re}}}{r_{\mathrm{ion}} + r_{\mathrm{re}}}. \tag{2.8}$$

Power dependence Previously, we observed a quadratic dependency on the laser power of the ionization rate for red illumination (637 nm), and of the recombination rate for green illumination (532 nm). As a first step, we verify the quadratic dependency of both rates for the two illumination wavelengths 560 nm and 593 nm. Fig. 2.8a shows these rates, as obtained from a hidden Markov model, and the quadratic dependency for low laser powers. Additionally, we calculate the steady state population of NV^- according to eq. (2.8), see fig. 2.8b. For these illumination powers, there is no notable change in the NV^- population.

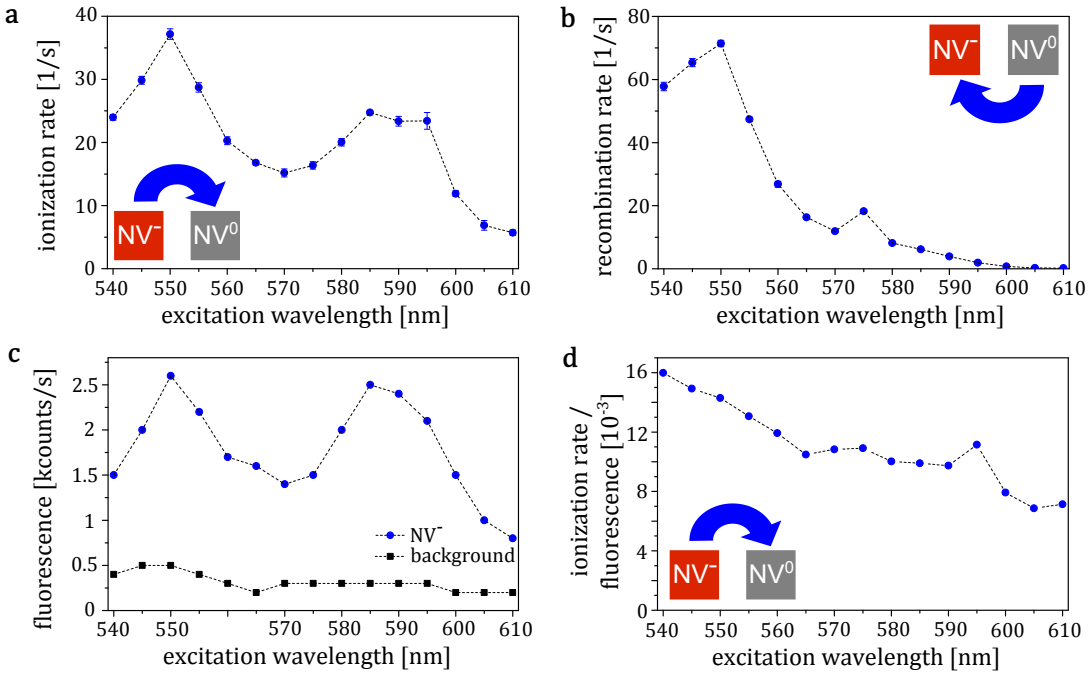

Figure 2.9.: Wavelength dependence of charge state dynamics. The illumination power was fixed to 1 μW. Dashed lines are guides to the eye. **a**, Ioization rate. **b**, Recombination rate. **c**, Fluoresence level of NV^- (background corrected, i.e. high fluorescence level minus low fluorescence level (background) of the time trace). **d**, Ratio of ionization rate to NV^- fluorescence level. Because NV^- fluorescence level $\propto$ NV^- excited state population, this ratio is proportional to the

Wavelength dependence To measure the wavelength dependence (540 to 610 nm) of the charge state dynamics, a fixed illumination power of 1 μW was used. We expect the ionization and recombination rates to roughly resemble the intrinsic absorption cross section of the involved excitation step, which directly influences the population of the excited state, and therefore the total rates according to eq. (2.3). Fig. 2.9a,b shows the wavelength dependence of the ionization and recombination rates. For the ionization rate, two maxima at around 550 and 590 nm are observed. As we will see below, these maxima are, indeed, a result of the intrinsic absorption of NV^-. For the recombination rate, we find a local maximum at 575 nm, which coincides with the zero phonon-line of NV^0. For higher photon energies, the recombination rate shows a steep increase. These two features resemble, as expected, a typical absorption spectrum of a solid state defect, with zero-phonon line and phonon side band.

Applying the hidden Markov model to the fluorescence time traces also yields the observed fluorescence levels. This allows us to determine the intrinsic absorption cross-section of NV^-, which was not possible before. In previous studies [72, 103], the measured fluorescence was always time averaged (or ensemble average) over the NV being in NV^- or NV^0. Additionally, the appearance of ionization and recombination rates influences the excited state population of NV^-. This, in turn, will lead to non-trivial deviations of the relation between intrinsic absorption cross-section of NV^- and its excited state population ($\hat{=}$ fluorescence), see appendix A.1. For our measurements, these imitations do not apply: Due to the time-resolved observation of the charge state, we are able to directly determine the fluorescence level of NV^- during time intervals where no ionization events occur. Therefore, the observed NV^- fluorescence shown in fig. 2.9c is directly proportional to the intrinsic absorption cross-section of NV^-. Note that this assertion only holds if the internal dynamics within NV^- do not depend on the illumination wavelength, which would be an unexpected feature. The measured double peak structure was not observed before, however, we cannot explain this behavior.

With the fluorescence level of NV^-, which is proportional to the excited state population, we can also calculate the ionization cross-section from the excited state according to eq. (2.3) by the ratio of total ionization rate to NV^- fluorescence. Note that this is only possible if ionization occurs exclusively from the excited state, however, ionization from the metastable state cannot be excluded, as discussed above. This ratio of total ionization rate to NV^- fluorescence is shown in fig. 2.9d.

2.3.2. NV^- population

An important requirement for QIP is the initialization of the system, which includes initialization of the NV in its negative charge state NV^-. So far, NV^0 does not seem suitable for QIP, due to short nuclear spin coherence times (see section 2.1) and the lack of ODMR. Here, we investigate the steady-state population of NV^- depending on the excitation wavelength, which is also the initialization probability into NV^- due to the long lifetime of NV^0. For the measurements performed in section 2.3.1 in the range of 540

to 610 nm, we can directly calculate the NV^- population from the ionization and recombination rates according to eq. (2.8). This is shown in fig. 2.10a. The visible behavior is mainly dominated by the recombination rate via the absorption of NV^0, cf. section 2.3.1. For wavelengths longer than 610 nm, the absorption of NV^0 and therefore also the NV^- population will go further down. However, what about shorter wavelengths? The previous measurements (section 2.3.1), which were based on real-time monitoring of the charge state dynamics, are not possible at shorter wavelength. Therefore, we employ another method to measure the NV^- population, which is based on single shot charge state detection (section 2.2). The measurement sequence is shown in fig. 2.10b. First, an arbitrary laser pulse with variable wavelength leads to a characteristic NV^- population. The NV^- population is then measured via single shot charge state detection, which leads to a histogram with two Poissonian distributions corresponding to the two charge states, see fig. 2.10b. By fitting the sum of two Poissonian distributions, the obtained areas of the single Poissonians yield the populations of NV^- and NV^0, which were prepared by the first laser pulse.

This measurement was performed in the range of 450 to 570 nm, and the result is shown in fig. 2.10c together with the data from fig. 2.10a. The population of NV^- is maximal at ≈ 75 % for 510 to 540 nm. For longer wavelengths, it decreases due to reduced absorption of NV^0 (see above). For shorter wavelengths, it decreases due to one-photon ionization of NV^- (see section 2.3.3). A similar behavior was observed in low temperature studies [103]. Therefore, initialization of the NV into its negative charge state with > 75 % probability was not achieved by illumination.

2.3.3. Ionization and recombination energy

So far, the observed ionization and recombination of NV^- were two-photon processes (cf. fig. 2.7). Because the used photon energies were too low, ionization and recombination only occurred via the excited states of NV^- and NV^0. However, if the photon energy is high enough, direct one photon ionization and recombination from the respective ground states is possible. Here, we will measure the transition from two-photon ionization and recombination to one-photon ionization and recombination, which will allow us to determine the energy of the NV^- ground state within the diamond band gap.

For this purpose, we use correlated single shot charge state measurements (see section 2.2), in order to determine the power dependence of the ionization and recombination rates for arbitrary illumination wavelength. Fig. 2.11a shows the measurement sequence. The first laser pulse measures the current charge state of the NV. The second laser pulse with arbitrary wavelength, power and duration will influence and possibly change the charge state due to photo-induced ionization and recombination. The last laser pulse again measures the charge state of the NV. By correlating the results of the two charge state measurements, the influence of the laser pulse on the charge state can be determined. We vary the length of the laser pulse at a fixed wavelength and power, which yields the charge state evolution for this specific illumination (wavelength and power).

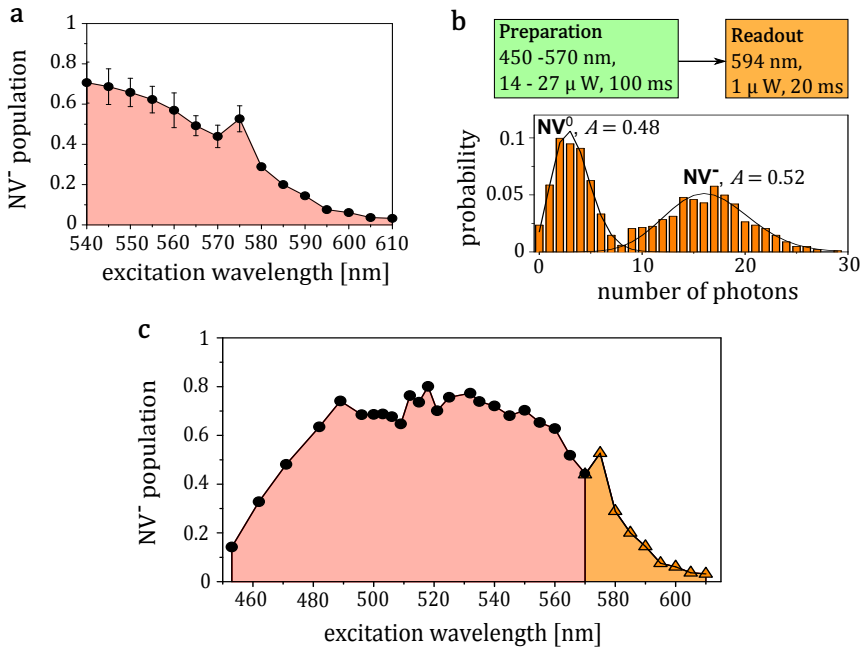

Figure 2.10.: NV^- population. **a**, NV^- population for 540 to 610 nm excitation wavelength, obtained from the ionization and recombination rates measured in section 2.3.1 with 1 μW excitation power. **b**, Upper part: Measurement sequence for the NV^- population based on single shot charge state detection. Note that the preparation pulse must be long enough to reach the steady-state population distribution. Only fluorescence during the second laser pulse is detected. Lower part: Probability distribution of measurement results (i.e. normalized histogram) for preparation with a laser pulse with 565 nm wavelength, 17 μW power and 100 ms duration. The charge states corresponding to the two peaks are indicated together with the amplitude A of a two-Poissonian fit (solid line). **c**, NV^- population depending on the excitation wavelength from 450 - 610 nm. Results from b (single shot charge state detection) and from a (real-time charge state monitoring) are combined here.

Depending on the result of the first charge state measurement (NV^- or NV^0), the evolution is obtained for the corresponding initial charge state (NV^- or NV^0, respectively), see fig. 2.11b. As shown in appendix A.2, from the measured charge state evolution we can obtain the ionization and recombination rates for this specific illumination. To measure the power dependence of the ionization and recombination rates for a specific illumination wavelength, we repeat this measurement for varying illumination powers at fixed illumination wavelength, which yields the data shown in fig. 2.11c. With the measured power dependence of the ionization rate r_{ion} and recombination rate r_{re}, we can separately determine the one-photon part and the two-photon part, by fitting a parabola

$$r_{\text{ion/re}} = aI + bI^2, \tag{2.9}$$

where a is the linear part corresponding to the one-photon process and b is the quadratic part corresponding to the two-photon process. We repeat the procedure above for different illumination wavelengths, and for each wavelength determine the relative cross-section of the one-photon ionization and recombination processes, which is the linear part a in eq. (2.9). This is shown in fig. 2.11d.

As we can see, for low photon energies, ionization and recombination are purely two-photon processes. Only above a certain threshold energy corresponding to the NV^- ionization energy and recombination energy, the relative cross-section for one-photon ionization and recombination starts to increase. To obtain the ionization energy of NV^- from this data, we model the relative cross-section for the one-photon processes according to Fermi's Golden Rule, and approximate the density of states (DOS) $g(E)$ at the edge of the valence and conduction bands by a free electron gas (in three dimensions), such that

$$g(E) \propto \sqrt{E - E_0}, \qquad E \geq E_0, \tag{2.10}$$

where E is the electron energy and E_0 the energy of the NV^- ground state relative to the band edges (absolute value), i.e. for ionization relative to the conduction band and for recombination relative to the valence band, and assume that the matrix element of the transition does, with good approximation, not depend on the photon energy. However, both the energy E and the energy E_0 are not sharp values, but have a probability distribution: The energy E is the energy of the electron after absorbing a photon, i.e. E is the photon energy, which depends on the spectral width of the excitation laser (Gaussian distribution with $\approx$ 2 nm standard deviation). The energy E_0 has a probability distribution due to thermal effects of both the NV^- ground state energy and the band edge energies. Because we do not know the form of this probability distribution, we approximate it with a Gaussian distribution. The final energy E_{f} of the electron after absorption, which is the initial electron energy plus the photon energy, is then also given by a Gaussian distribution

$$P(E_{\text{f}}) \propto e^{-\frac{1}{2}\left(\frac{E_{\text{f}} - \hbar\omega}{\sigma}\right)^2}, \tag{2.11}$$

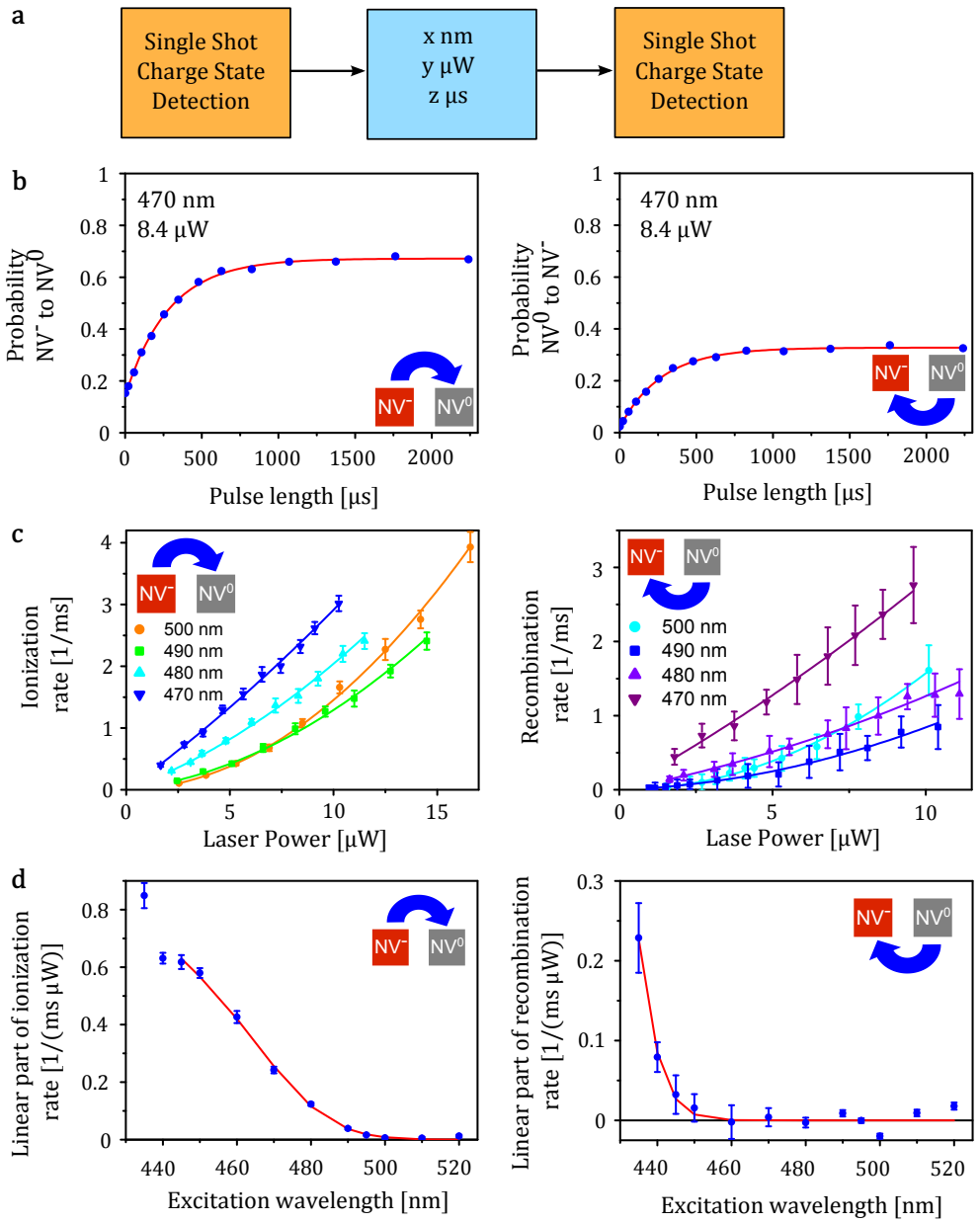

Figure 2.11.: Ionization and recombination energies. **a**, Measurement sequence for correlated charge state detection. The second laser pulse can be arbitrary wavelength, power and duration. **b**, Measured charge state evolution during the second laser pulse for initial state NV^- (left graph) and NV^0 (right graph), which is given by the result of the first charge state measurement. The solid (red) lines are fits, as described in appendix A.2. **c**, Power dependence of the ionization and recombination rates (left and right graph, respectively) for different illumination wavelengths. The fits (solid lines) are performed according to eq. (2.9). **d**, Wavelength dependence of the linear part of ionization and recombination rates (left and right graph, respectively). See text for explanation of fit (solid red line)

where $\hbar\omega$ is the average photon energy set by the excitation laser and σ the width of the distribution. The expected relative cross-section for the one-photon processes (a in eq. (2.9)) is the convolution of the final photon energy eq. (2.11) with the DOS eq. (2.10),

$$a(\hbar\omega) = A \int_{-\infty}^{\infty} \sqrt{E_\mathrm{f} - E_0}\; e^{-\frac{1}{2}\left(\frac{E_\mathrm{f}-\hbar\omega}{\sigma}\right)^2} \mathrm{d}E_\mathrm{f}, \tag{2.12}$$

where E_0, σ and A are fitting parameters. Eq. (2.12) is solved numerically ($\sqrt{E_\mathrm{f} - E_0}$ is zero for $E_\mathrm{f} < E_0$). For fitting the ionization rate, only data points down to 445 nm are considered, because the approximation eq. (2.10) is only valid close to the band edge. For the recombination rate, there are only four relevant measurements points. Therefore, for the parameter σ the value from the ionization data with $\sigma = 0.069$ eV was used, because the broadening mechanisms are the same. Then E_0 is the only fitting parameter for the recombination rate shown in fig. 2.11d.

From the above described analysis of the data shown in fig. 2.11d, we can extract the ionization energy of NV^-, which is $E_\mathrm{ion} = (2.604 \pm 0.005)$ eV, and the recombination energy $E_\mathrm{ion} = (2.94 \pm 0.02)$ eV.

2.4. Improved electron spin initialization

The observed photo-ionization of the NV also sheds new light onto the electron spin polarization in the NV^- ground state. On the one hand, the optical cycle during illumination within NV^- leads to polarization into $m_\mathrm{s} = 0$ due to spin-state dependent inter-system crossing. On the other hand, the illumination also leads to ionization and recombination. After recombination, NV^- is assumed to end up in a random spin state, as there is no physical reason for preferred population of $m_\mathrm{s} = 0$. This introduces a depolarizing mechanism, which increases with the illumination power. Therefore, we expect increased electron spin polarization for decreasing illumination power. The electron spin polarization can be measured very accurately by single shot nuclear magnetic resonance (NMR), see section 2.1.

Fig. 2.12a shows the measurement sequence. Fig. 2.12b shows the measured nuclear spin flip probability in $m_\mathrm{S} = 0$ after a low power red laser pulse (637 nm, 1 μW). Without the red pulse, the population of the $m_\mathrm{S} = 0$ state is given by the green laser pulse used for the nuclear single shot measurement. As can be seen, even a very short low power red pulse increases this population by increasing the polarization of the electron spin in NV^-. The subsequent decrease of the spin flip probability is due ionization of NV^- by the red laser. For this illumination, the lifetime of NV^- was ≈ 2 ms. In the following, we will measure the absolute polarization of the electron spin in NV^-, by measuring the nuclear spin flip probability in $m_\mathrm{S} = -1$.

In order to obtain the electron spin polarization of NV^- from the nuclear spin flip probability p_flip in $m_\mathrm{S} = -1$, a few things have to be taken into account. We are interested in the polarization within NV^-, which is the relative occupation probability of the m_S

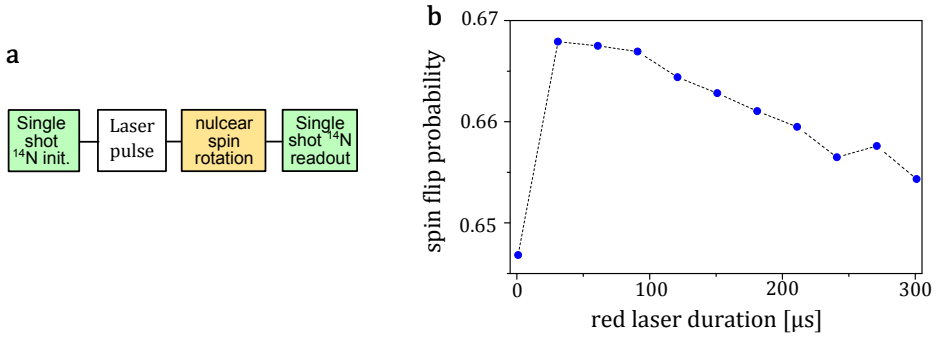

Figure 2.12.: NV$^-$ polarization measurement. **a**, Measurement sequence. **a**, Spin flip probability in $m_S = 0$ after varying duration of red (637 nm), 1 μW illumination.

states, but not the total occupation probability of $m_S = -1$. Therefore, we normalize the measurement result by the total probability to be in NV$^-$, which is $p_{NV-} = 0.75$. Additionally, the measured flip probability is reduced by the single shot measurement fidelity F, cf. fig. 2.1b. The estimated relative flip probability $p_{flip,rel}$ is

$$p_{flip,rel} = p_{flip} \frac{1}{0.75} \frac{1}{1-2F^2}, \tag{2.13}$$

where p_{flip} is the measured flip probability. Additionally, the long duration of the rf-π pulse of 600 μs relative to the electron T_1 time of ≈ 4 ms leads to electron spin flips during the nuclear spin rotation. This will lead to an additional flip probability in $m_S = -1$ due to electron spin flips from $m_S = 0$ to -1. This effect can be estimated by a convolution of the flip probability of the $m_S = 0$ to -1 state with the flip probability of the nuclear spin due to the induced Rabi oscillations. The probability p_{ms-1} that the electron spin has flipped at time t from the $m_S = 0$ to -1 state is approximated by

$$p_{ms-1} = 0.33 \left(1 - \exp\left(-t/T_1\right)\right), \tag{2.14}$$

(where we approximated the population of the $m_S = 0$ state at time $t = 0$ to be 100%), and the probability that it flips during time dt is deduced to

$$\mathrm{d}p_{ms-1} = \frac{0.33}{T_1} \left(1 - \exp\left(-t/T_1\right)\right) \mathrm{d}t. \tag{2.15}$$

The Rabi-induced flip probability of the nuclear spin, $p_{flip,t}$, if the electron spin is flipped from $m_S = 0$ to -1 at time t, is

$$p_{flip,t} = \sin^2\left(\frac{\Omega(t_\pi - t)}{2}\right), \tag{2.16}$$

where t_π is the duration of the nuclear pulse, and $\Omega = 2\pi\frac{1}{1.2}$ kHz is the nuclear Rabi frequency. The total probability that the nuclear spin is flipped in the experiment due

to electron T_1 decay from $m_S = 0$ to -1 is

$$p_{\text{flip,T1}} = \int_{t=0}^{t_\pi} \sin^2\left(\frac{\Omega(t_\pi - t)}{2}\right) \frac{0.33}{T_1} \left(1 - \exp\left(-t/T_1\right)\right) \mathrm{d}t. \tag{2.17}$$

Numerically solving eq. (2.17) yields $p_{\text{flip,T1}} = 2.4$ %.

The flip probability p_{flip} is measured by the sequence shown in fig. 2.12a, once with on-resonant rf pulses and once with off-resonant rf pulses. The difference of these two measurements is p_{flip}, which is then normalized by eq. (2.13), and $p_{\text{flip,T1}}$ is subtracted to obtain the relative population $\rho_{\text{ms}-1}$ of the $m_S = -1$ state. By assuming that the populations of the $m_S = -1$ and $m_S = +1$ states are the same, $\rho_{\text{ms}-1} = \rho_{\text{ms}+1}$, we can calculate the relative population of $m_S = 0$ within NV^- by $\rho_{\text{ms0}} = 1 - 2\rho_{\text{ms}-1}$ This measurement is performed for high power green illumination (532 nm) typically used in experiments, and low power red illumination (637 nm). The results are shown in table 2.1.

Please note that these are preliminary results, and more accurate and meaningful

λ	power	time	resonant	off-resonant	p_{flip}	$\rho_{\text{ms}-1}$	ρ_{ms0}
532 nm	≈ 100 μW	1 μs	0.204	0.172	6.5 %	4.1 %	91.8 %
637 nm	≈ 1 μW	30 μs	0.1839	0.1647	3.82 %	1.42 %	97.2 %

Table 2.1.: Polarization measurement results. Resonant and off-resonant are measured spin flip probabilities for resonant and off-resonant rf control.

results would require further measurements, like measuring the power-dependence of polarization at one wavelength. The accuracy of the results could be improved by using much higher Rabi frequencies for the nuclear spin rotation, to decrease the effect of electron T_1 decay, and by measuring the spin flip probability in all m_S and directly calculating the relative populations.

2.5. Conclusions

In this chapter, we have unravelled the photo-induced ionization and recombination mechanism of NV^-, which is important for understanding the dynamics of the NV. Especially for high-fidelity quantum information processing tasks, control of the charge state is necessary. We have already demonstrated a method to measure the charge state of a single NV by a non-destructive, single shot measurement, see section 2.2. In sections 3.1 and 3.2, we will use this method for charge state pre-selection of measurements. In section 3.3 we will introduce another method based on nuclear single shot measurements, to post-select measurement results for the desired charge state. Additionally, the observed blinking due to ionization of the NV for low-power illumination (cf. fig.

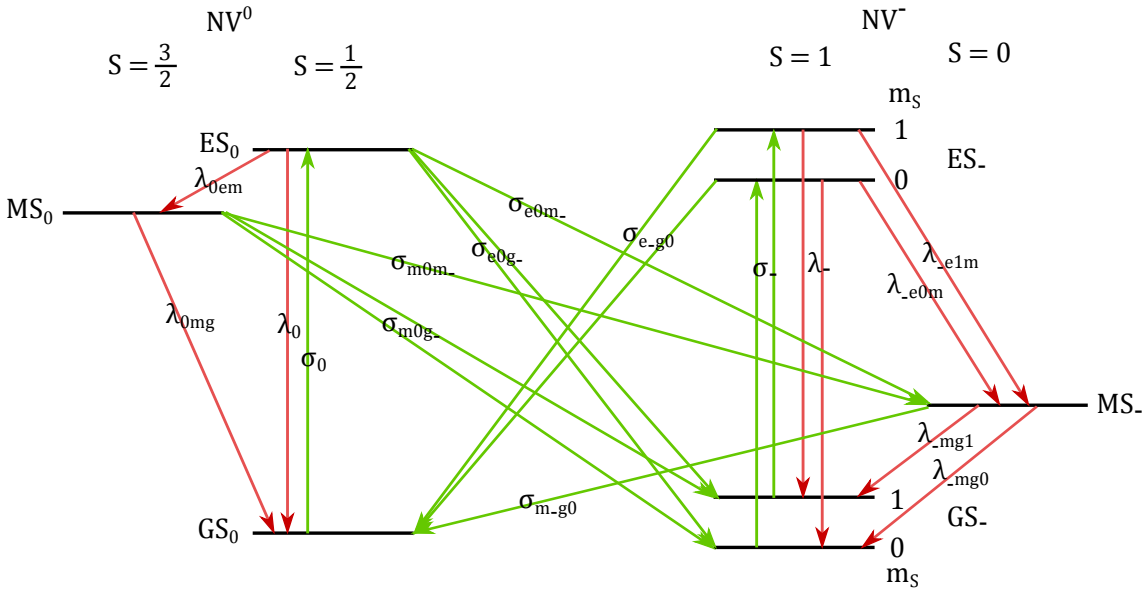

Figure 2.13.: Proposed model for the optical dynamics of the NV. $ES_{0/-}$, $MS_{0/-}$, $GS_{0/-}$, are excited state, metastable state and ground state of NV^0 and NV^-. Red arrows indicate radiative and non-radiative decay processes, where the decay rate λ is the figure of interest. Green arrows indicate processes induced by photon absorption, where the absorption cross-section σ is the figure of interest. The actual rate of these transitions is obtained by multiplying the corresponding absorption cross-section σ with the illumination power. Transitions between the two charge states are assumed to be spin-state independent. The placement and ordering of the states is only given schematically for illustrative reasons, and does not necessarily represent the relative energies.

2.2) can be used for high-resolution microscopy by stochastic optical reconstruction microscopy (STORM) [107] respectively photoactivation localization microscopy (PALM) [108]. Thereby, several emitters within a diffraction limit spot are switched on and off stochastically, such that at any time fluorescence of most likely only one emitter is detected, which leads to fluorescence bursts whenever an emitter is "on". This allows for reconstruction of the position of the emitter by fitting its point spread function to the observed fluorescence during one burst.

2.5.1. Rate equation model including photo-ionization

The results of this chapter allow us to propose a new rate equations model to describe the effective dynamics within NV^-, see fig. 2.13. Previously, power dependent rates between the triplet and singlet states of NV^- have been discussed and investigated [109, 110], however, without considering the actual mechanism and spin selective dynamics within NV^-. The model proposed in fig. 2.13 takes into account the two-photon ionization and recombination processes as discussed in section 2.3, i.e. for illumination wavelengths

of around 500 to 600 nm. The model is supposed to be able to explain the dynamics for NV^-, specifically the fluorescence, the spin polarization, and the total population of NV^-, but not for NV^0, and spin selective rates within NV^0 are not considered. Note that several states of both charge states (see [78], [81]) are neglected here, which are believed to not being relevant for the above discussed values at the current state of knowledge. Also note that for the actual values of the absorption cross-sections, the degeneracy due to different spin orientations of the states has to be taken into account, in accordance with Fermi's Golden Rule.

3. Applications of nuclear spin single shot readout

In this chapter, we will apply single shot readout of the ^{14}N nuclear spin in several experiments. Is section 3.1, we show violation of a temporal Bell inequality. Here, high-fidelity single shot readout is a necessary requirement. In section 3.2, we implement generalized measurements for discrimination of non-orthogonal quantum states, where single shot readout is needed for consecutive measurements. For both these experiments, we will additionally employ charge state pre-selection, to prepare the NV in its negative charge state, see section 2.2. Charge state pre-selection is based on low-power illumination of the NV with $\approx$ 595 nm wavelength, such that only fluorescence of NV$^-$ is detected. Due to the low illumination power, photo-ionization of the NV is suppressed, allowing for non-destructive, single shot charge state detection. In section 3.3, we use single shot readout for quantum-limited measurements of magnetic fields. To this end, we will demonstrate a new method for charge state post-selection, by using the third state of the ^{14}N nuclear spin.

The results presented in this chapter are published in [44] (section 3.1), [46] (section 3.2), [45] (section 3.3).

3.1. Violation of a temporal Bell inequality

When quantum mechanics (QM) was introduced, the intuitive, yet classical concepts of realism and locality had to be dismissed. This lead Einstein, Podolsky and Rosen in 1935 [111] to believe that quantum mechanics cannot be complete, as it contradicts with these concepts, which they defined as: (1) *Reality*: "If, without in any way disturbing a system, we can predict with certainty (i.e., with probability equal to unity) the value of a physical quantity, then there exists an element of physical reality corresponding to this physical quantity", and (2) *locality*: The measurement of one system can have no immediate effect on another, spatially separated system, e.g. for two entangled systems. For the given definition of *reality* it is important to note that the authors of [111] assumed that a deterministic description of the world is possible, i.e. that the result of a measurement can, in principle, be predicted with certainty. Some time later in 1964, Bell proposed an experimentally testable inequality that holds for any theory which complies with both these concepts [112]. However, he also showed that QM violates this inequality, meaning that either QM is wrong (and not just incomplete) or that the assumptions are wrong.

Nowadays, we know that the latter is the case, and *reality* and *locality* do not apply for a description of the world on a quantum level. Especially the violation of *reality* for macroscopic systems is counter-intuitive to how we experience the world. This was exemplified by Schrödinger's cat gedanken experiment [113]. He envisaged a cat that is trapped within a perfectly isolated box, together with a device that can randomly kill the cat. According to QM, the cat is dead and alive at the same time, as long as observations of what is happening inside the box are not possible. Only when we open the box (measure the cat's state), we will find the cat in one of its two states, either dead or alive, which are *exclusive* measurement results. This result is non-deterministic, i.e. it is impossible to assign the cat's state as either dead or alive right before the measurement. Therefore, the concept of defining the state as dead and alive at the same time is not merely an illustration of our lack of knowledge, but means that the cat's state, in the sense of a measurement result, is not even defined.

The inequality proposed by Bell, and similar proposals [114, 115, 116], focused on the concept of *locality*. Here, however, we will test *reality* for a single system, without the assumption of *locality*. Such an experimental test based on an inequality was first proposed by Leggett and Garg in 1985 in the context of macroscopic superconducting quantum interference devices (SQUID) [117]. Instead of probing correlations of two spatially separated system, one is interested in state correlations of a single system at different points in time. This type of inequality (see below) was later termed temporal Bell inequalities (TBI), and possible variations for the experimental implementation were proposed [118, 119, 120, 121, 122] and implemented for SQUIDs [123] and for photons [124], both based on weak measurements.

A TBI similar to the one given by Leggett and Garg [117] can be obtained with only the assumption of *realism*:

A1) *Realism*: The state of any physical system is always well defined, i.e. the dichotomic variable $M_n(t)$, which tells us whether ($M_n(t) = 1$) or not ($M_n(t) = -1$) the system is in state n, is, at any time, $M_n(t) = \{-1, 1\}$.

Without loss of generality, in the following we will look at only one state n, and omit this index. The definition of *realism* does not necessarily mean that we know the value of $M(t)$, but merely that it exists, in principle, and that it can be obtained from some set of time-dependent variables $\lambda(t)$, the so called hidden variables, i.e. by $M(t) = M(\lambda(t))$. To derive the inequality along the lines of [121], we start by defining the temporal correlation $K(t_i, t_j) = K_{ij}$ of $M(t)$ at the two times t_i, t_j as

$$K_{ij} = \int \mathrm{d}\lambda(t) P(\lambda(t)) M_i M_j := \langle M_i M_j \rangle \,, \tag{3.1}$$

where $P(\lambda(t))$ is the probability that a certain evolution $\lambda(t)$ happens, and $M_i = M(\lambda(t_i))$. K_{ij} is the statistical information on M_i given that M_j is known, and vice versa. We now take the value of $M(t)$ at three points in time, $\{M_1, M_2, M_3\}$, for any

evolution $\lambda(t)$, and find that

$$M_1M_2 + M_2M_3 - M_1M_3 \leq 1, \tag{3.2}$$

as $M_i = \{-1, 1\}$ according to A1. By averaging this equation according to eq. (3.1), we finally obtain the TBI

$$\begin{aligned}&\langle M_1M_2 + M_2M_3 - M_1M_3\rangle = \langle M_1M_2\rangle + \langle M_2M_3\rangle - \langle M_1M_3\rangle \\ &= K_{12} + K_{23} - K_{13} \leq 1,\end{aligned} \tag{3.3}$$

which is only based on A1, and is violated by quantum mechanics [117].

However, it turns out that in order to measure violation of eq. (3.3), non-invasive measurements are required. By measuring K_{12}, K_{23}, K_{13}, i.e. M_1M_2, M_2M_3, M_1M_3, separately, the dynamics of the system, i.e. the $P(\lambda(t))$ in eq. (3.1), are changed for the intermediate measurement of M_2M_3 needed for K_{23}. Therefore, the first line in eq. (3.3) does not hold any more, i.e. we cannot assume eq. (3.3) to be fulfilled only based on *realism*. On the other hand, direct measurement of M_1, M_2, M_3 at the same experimental run will obey eq. (3.2), as the possible measurement results are $M_i = \{-1, 1\}$ by definition. A possible solution are weak measurements [125], which have been used to show violation of a TBI in SQUIDs and for photons [123, 124].

Here, we use a different approach based on a further assumption, namely *stationarity* [120, 121]:

A2) *Stationarity*: The conditional probability $Q_{nm}(t_i, t_j)$ to find a system in state m at time t_j, if it was in state n at time t_i only depends on the time difference $t_j - t_i = \Delta t$.

This assumption is fulfilled if the probability distribution $P(\lambda(t))$ for the possible evolutions of $\lambda(t)$ is always the same for a given initial state $M(t)$. Of course, the evolution $\lambda(t)$ of the system depends on its interaction with the environment, i.e. we have to ensure that the environment is stable enough and / or that these interactions are small enough. As we will see later, $Q_{nm}(\Delta t)$ is measured to be indeed stable on long time scales, see fig. 3.1b. Additionally, the decoherence in our system is very small on the time scale of single measurements, indicating that the influence on the dynamics due to environmental interactions is small. Nevertheless, it is assumed to be possible to construct hidden variable theories, which fulfil *realism* and the observed measurement results, yet violate *stationarity*, i.e. our measurement result will impose restrictions on possible hidden variable models. $Q_{nn}(\Delta t)$ is connected with K_{ij} by

$$K_{ij} = K(\Delta t) = 2Q_{nn}(\Delta t) - 1. \tag{3.4}$$

Inserting eq. (3.4) into eq. (3.3) and setting $t_2 - t_1 = t_3 - t_2 = \Delta t$ we obtain the TBI

$$Q_{nn}(2\Delta t) - Q_{nn}^2(\Delta t) \geq 0, \tag{3.5}$$

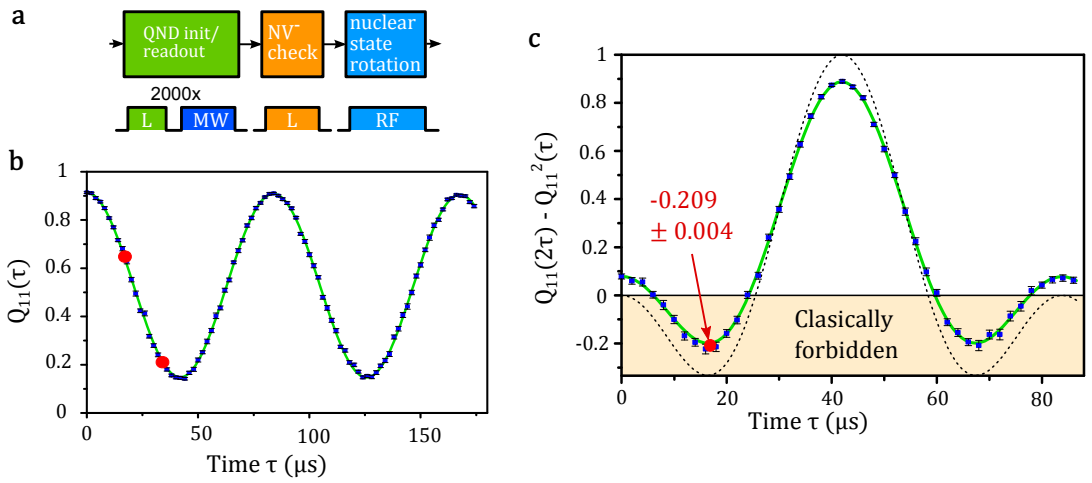

Figure 3.1.: Violation of temporal Bell inequality. **a**, Measurement sequence (see text). **b**, Rabi oscillations of the ^{14}N nuclear spin obtained by varying the duration of the rf pulses in sequence a, yielding $Q_{11}(\tau)$. The blue squares are the measurement results, the green line a cosine fit. The errors bars are the empirical standard deviation obtained from many chronologically ordered sub-ensembles of the full measurement data. Therefore, these errors also impose an upper bound on the long-term temporal fluctuations of $Q_{11}(\Delta t)$. The measurement points at the red dots were measured with increased accuracy. **c**, Calculated result of the TBI eq. (3.5). The green line is the result of the TBI calculated from the fitting parameters of b. For comparison, the black dashed line would be the result of an ideal experiment (error-free implementation and measurement of Rabi oscillations). The red dot corresponds to the two red dots in b.

which can be experimentally tested without the need of measuring the intermediate correlation of $\langle M_2 M_3 \rangle$. The temporal Bell inequality eq. (3.5) is violated by quantum mechanics for a Rabi oscillation with $Q_{nn}(\Delta t) = \cos^2(\Omega \Delta t)$ (where Ω is the Rabi frequency), if Δt corresponds to a rotation of $\approx \pi/5.1$ on the Bloch sphere, yielding a value of $-1/3$.

3.1.1. Experimental violation of the temporal Bell inequality

For testing the TBI eq. (3.5) experimentally, we will use the ^{14}N nuclear spin associated with the NV in diamond. Here, projective, single shot readout is necessary to measure two-time correlations. Additionally, to observe full-contrast Rabi oscillations (only limited by the readout fidelity) we also need to initialize the NV into its negative charge state, which is achieved by charge state pre-selection. The measurement sequence is shown in fig. 3.1a. First, the state of the ^{14}N nuclear spin is measured by single shot readout. Second, single shot charge state detection is performed, see section 2.2. Third, a rf pulse of varying duration induces Rabi oscillations of the nuclear spin. Finally, the next single shot state measurement of the ^{14}N is performed. Correlating the two ^{14}N spin state measurements and averaging over many measurements yields the conditional

probability $Q_{11}(\Delta t)$.

Fig. 3.1b shows $Q_{11}(\Delta t)$ (the Rabi oscillations). We can see that the curve is not symmetric with respect to $Q_{11}(\Delta t) = 0.5$, which is attributed to the limited fidelity of the charge state pre-selection and the imperfect polarization of the NV electron spin, cf. section 2.2 and section 2.4. From the measured value of $Q_{11}(\Delta t)$, we calculate the result of the TBI eq. (3.5), see fig. 3.1c. These results demonstrate a clear violation of the TBI.

Conclusions This violation of a TBI indicates that the dynamics of a single nuclear spin cannot be described by a deterministic theory obeying the *realism* assumption A1, however, with the possible loophole that the *stationarity* assumption A2 is not fulfilled. More generally, these results indicate that quantum mechanics can, indeed, be considered as a complete theory, describing the non-deterministic behaviour of nature. A possible approach to overcome the limiting assumption of *stationarity* is the use of delayed-choice measurements, by utilizing a second nuclear qubit [119].

3.2. Distinguishing between non-orthogonal quantum states

In this section, we will experimentally investigate optimal, generalized quantum measurements of two non-orthogonal states. The standard description of the quantum measurement process is based on observables [126]. An observable $\hat{O}$ is a hermitian operator, and can be written in its eigenbasis as

$$\hat{O} = \sum_m o_m \left|o_m\right\rangle \left\langle o_m\right| , \tag{3.6}$$

where the eigenvalues o_m are the possible measurement results and $|o_m\rangle$ the corresponding eigenstate. After the measurement, the system will be in the eigenstate corresponding to the measurement result o_m. The probability $p(o_m)$ to obtain the measurement result o_m can be written in terms of projectors $\hat{P}_m = |o_m\rangle \langle o_m|$

$$p(o_m) = \langle\psi|o_m\rangle \langle o_m|\psi\rangle = \langle\psi| \hat{P}_m |\psi\rangle , \tag{3.7}$$

where $|\psi\rangle$ is the state of the system. Note that the projectors are orthogonal, i.e. that $\hat{P}_m \hat{P}_n = 0$ for $m \neq n$. Generalized measurements are based on so called probability operators $\hat{\Pi}_m$, whose expectation value is the probability that a measurement yields the result m [127]. The most important difference to standard measurements is that the operators $\hat{\Pi}_m$ do not need to be orthogonal.

The generalized measurement description allows for optimal discrimination between non-orthogonal quantum states. This is important e.g. for quantum communication [128, 129, 130, 131]. In quantum key distribution, transmission of the key in two non-orthogonal states leads to improved security [128]. By utilizing unambiguous state discrimination (see below), perfect quantum teleportation even with nonmaximally entangled states can be achieved [131].

3.2.1. Optimal state discrimination

The discrimination of non-orthogonal quantum states can be optimized with respect to two requirements, which are the minimum-error measurement and unambiguous state discrimination (USD). In the following, we consider the two non-orthogonal states $|a\rangle , |b\rangle$ which are defined in an orthogonal basis $\{|0\rangle , |-1\rangle\}$ as

$$|a\rangle = \cos\theta|0\rangle - \sin\theta|-1\rangle, \quad |b\rangle = \cos\theta|0\rangle + \sin\theta|-1\rangle, \tag{3.8}$$

where $0 \leq \theta \leq \pi/4$, and θ is half the angle between $|a\rangle$ and $|b\rangle$. We assume that no further prior information about the states is provided, such that the probabilities of the system to be in state a, b are $p_a = p_b = 0.5$.

For the minimum-error measurement, the goal is to minimize the error in identifying

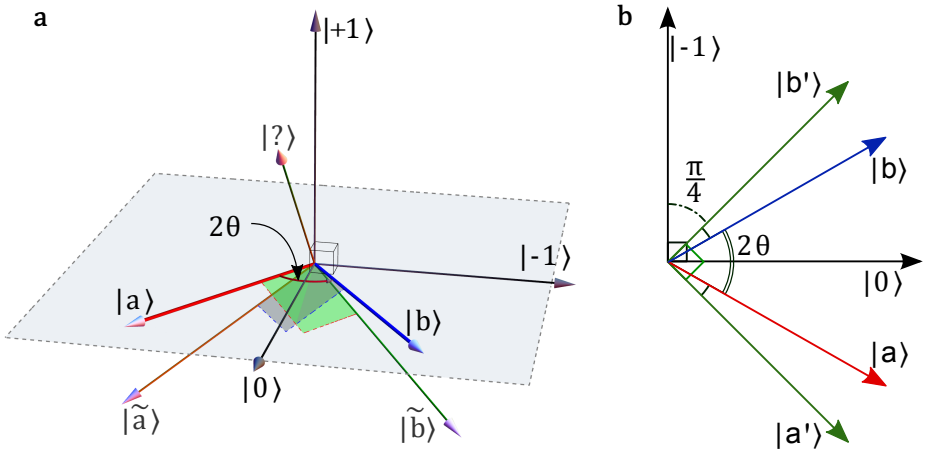

Figure 3.2.: Geometric representation of measurement basis. **a**, For optimal USD. **b**, For the minimum-error measurement

the state, while each measurement should yield a state assignment. For two states, this approach also yields the highest mutual information [127]. It turns out that this can be achieved by a standard projective measurement in an appropriate orthogonal measurement basis $\{|a'\rangle, |b'\rangle\}$ [127]. This is illustrated in fig. 3.2b. The orthonormal basis $\{|a'\rangle, |b'\rangle\}$ is symmetric to $|a\rangle, |b\rangle$, with

$$|a'\rangle = \frac{1}{\sqrt{2}}\left(|0\rangle - |-1\rangle\right), \quad |b'\rangle = \frac{1}{\sqrt{2}}\left(|0\rangle + |-1\rangle\right), \tag{3.9}$$

which is independent of the angle θ. A positive result for measurement on $|a'\rangle$ indicates $|a\rangle$, and a positive result on $|b'\rangle$ indicates $|b\rangle$. The error probability of making a false state identification (with ideal measurements) is [132]

$$p_{err}^{opt} = \frac{1}{2}\left(1 - \sqrt{1 - |\langle a|b\rangle|^2}\right). \tag{3.10}$$

Since every measurement yields a state assignment due to the orthogonal measurement basis, the probability of a correct result is $p_{corr} = 1 - p_{err}^{opt}$, which is the highest possible probability to identify the state correctly.

For unambiguous state discrimination (USD), we require that every state identification is correct (for ideal measurements). This is possible by allowing for inconclusive measurement results. A non-optimal approach (called standard USD in the following) is obtained by using the orthogonal measurement basis $\{|a\rangle, |a^\perp\rangle\}$ or $\{|b\rangle, |b^\perp\rangle\}$, where $|a^\perp\rangle$ and $|b^\perp\rangle$ are orthogonal to $|a\rangle$ and $|b\rangle$, respectively. Then, a positive measurement result on $|a^\perp\rangle$ ($|b^\perp\rangle$) indicates that the state is not $|a\rangle$ ($|b\rangle$), such that is must be unambiguously $|b\rangle$ ($|a\rangle$). Specifically, $|a^\perp\rangle$ and $|b^\perp\rangle$ are

$$|a^\perp\rangle = \sin\theta|0\rangle + \cos\theta|-1\rangle, \quad |b^\perp\rangle = \sin\theta|0\rangle - \cos\theta|-1\rangle. \tag{3.11}$$

The drawback compared to minimum-error measurements is that not every measurement yields a conclusive results, i.e. if the measurement is positive on $|a\rangle$ ($|b\rangle$), still both initial states are possible. The probability of such an inconclusive result with ideal measurements is given by

$$p_? = (1 + |\langle a|b\rangle|^2)/2 \geq 1/2, \tag{3.12}$$

and the probability of a correct state assignment is

$$p_{\text{corr}} = 1 - p_?. \tag{3.13}$$

Optimal USD was proposed by Ivanovic, Dieks and Peres in [133, 134, 135], and is optimal in the sense that it yields the lowest possible probability of an inconclusive result. It is realized by extending the measurement Hilbert space to at least three dimensions $\{|0\rangle, |-1\rangle, |+1\rangle\}$. A possible choice of such a measurement basis is illustrated in fig. 3.2a. The measurement basis is spanned by

$$\begin{aligned} |\tilde{a}\rangle &= \frac{1}{\sqrt{2}}\left(\tan\theta|0\rangle - |-1\rangle - \sqrt{1-\tan^2\theta}|+1\rangle\right), \\ |\tilde{b}\rangle &= \frac{1}{\sqrt{2}}\left(\tan\theta|0\rangle + |-1\rangle - \sqrt{1-\tan^2\theta}|+1\rangle\right), \\ |?\rangle &= \sqrt{1-\tan^2\theta}|0\rangle + \tan\theta|+1\rangle, \end{aligned} \tag{3.14}$$

where $|\tilde{a}\rangle$ and $|\tilde{b}\rangle$ herald the states $|a\rangle$ and $|b\rangle$, respectively, and $|?\rangle$ corresponds to the inconclusive result. For this basis, the overlap of $|\tilde{a}\rangle$ with $|b\rangle$ and of $|\tilde{b}\rangle$ with $|a\rangle$ is zero, $\langle\tilde{a}|b\rangle = \langle\tilde{b}|a\rangle = 0$, such that positive results on $|\tilde{a}\rangle$, $|\tilde{b}\rangle$ yield unambiguous state assignment. For ideal measurements, the probability of correct state assignment p_{corr} and the probability of inconclusive results $p_?$ are

$$\begin{aligned} p_{\text{corr}} &= |\langle\tilde{a}|a\rangle|^2 = |\langle\tilde{b}|b\rangle|^2 = 1 - |\langle a|b\rangle| \\ p_? &= |\langle?|a\rangle| = |\langle?|b\rangle| = |\langle a|b\rangle|. \end{aligned} \tag{3.15}$$

3.2.2. Experimental implementation

Here, we implement the generalized measurements introduced in section 3.2.1 on the ^{14}N nuclear spin of the NV. We employ projective, single shot readout of the nuclear spin and charge state pre-selection (cf. sections 2.2, 3.1.1). The basic measurement sequence is shown in fig. 3.3a. The first step is the initialization of the ^{14}N nuclear spin into $m_I = |0\rangle$ by measurement pre-selection. Then, single shot charge state detection is performed to pre-select for NV^-. After these two initialization steps, the spin operations for state preparation and measurement are carried out. For the preparation of the states $|a\rangle, |b\rangle$ in eq. (3.8), a 2θ pulse is applied onto the $m_I = |0\rangle \leftrightarrow |-1\rangle$ transition

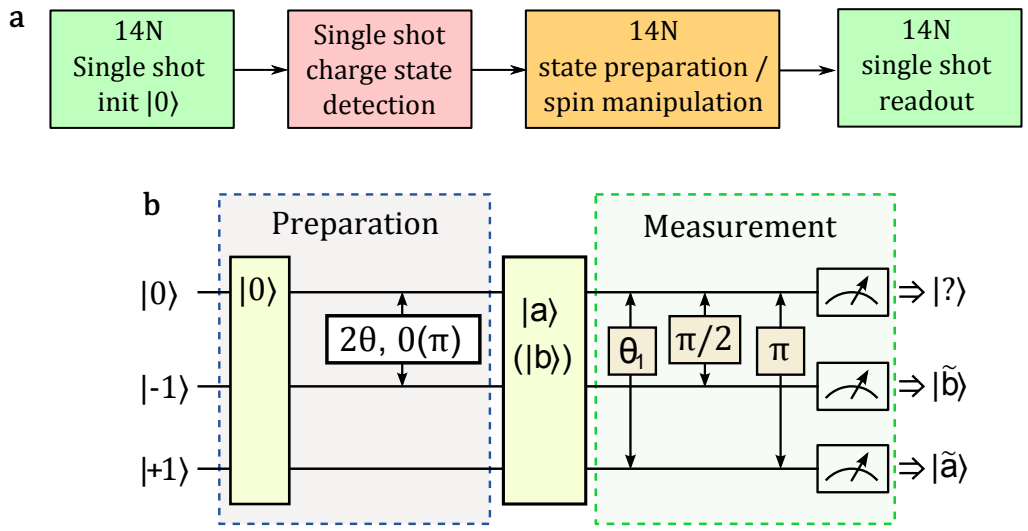

Figure 3.3.: Measurement sequence. **a**, Basic sequence with ^{14}N initialization and charge state pre-selection. **b**, Pulse sequence on the ^{14}N spin for optimal USD.

with phase 0 or π, creating state $|a\rangle$ or $|b\rangle$, respectively. The measurement basis, which depends on the chosen generalized measurement protocol as described in section 3.2.1 is realized by rotating the state appropriately on both transitions $m_\mathrm{I} = |0\rangle \leftrightarrow |-1\rangle$ and $m_\mathrm{I} = |0\rangle \leftrightarrow |+1\rangle$ (see below), such that the final measurement in the spin eigenbasis $m_\mathrm{I} = \{|0\rangle, |-1\rangle, |+1\rangle\}$ corresponds to the desired measurement basis. This final projective readout is carried out by subsequent measurements on the eigenstates. Due to the finite readout fidelity and possible spin flips during readout, multiple positive results or no positive results for the subsequent measurements can be obtained. For multiple positive results, we take the first one as the final result. If no positive result is obtained, the measurement is ignored, which leads to an effective imperfect detection efficiency.

The measurement basis for the minimum error measurement is given in eq. (3.9), and is independent of the angle θ. It is obtained by applying a $\pi/2$ pulse with phase 0 onto the $m_\mathrm{I} = |0\rangle \leftrightarrow |-1\rangle$ transition. Additionally, we apply a π rotation onto the $m_\mathrm{I} = |0\rangle \leftrightarrow |+1\rangle$ transition, such that the final measurement is performed in the $m_\mathrm{I} = \{|-1\rangle, |+1\rangle\}$, which yields higher fidelities than measurements on $m_\mathrm{I} = |0\rangle$. The probability to obtain at least one positive measurement result (effective detection efficiency) for this implementation was $\approx 83.1\%$.

For the standard unambiguous state discrimination, the operations $\hat{U}_a = |0\rangle\langle a| + |1\rangle\langle a^\perp|$ and $\hat{U}_b = |0\rangle\langle b| + |1\rangle\langle b^\perp|$ yield the two possible measurement bases given in eq. (3.11). These operations are realized by 2θ and -2θ pulses for $\hat{U}_a$ and $\hat{U}_b$, respectively, on the $m_\mathrm{I} = |0\rangle \leftrightarrow |-1\rangle$ transition. Again, a π rotation onto the $m_\mathrm{I} = |0\rangle \leftrightarrow |+1\rangle$ transition is performed before readout. Depending on the chosen basis, $m_\mathrm{I} = |-1\rangle$ corresponds to $|a^\perp\rangle$ or $|b^\perp\rangle$, and $m_\mathrm{I} = |-1\rangle$ corresponds to $|a\rangle$ or $|b\rangle$. Here, the effective detection

efficiency was $\approx 84.6\%$.

The pulse sequence for the optimal USD is shown in fig. 3.3b. The operation $\hat{U}$ that generates the measurement basis defined in eq. (3.14) is (in the basis $\{|0\rangle, |-1\rangle, |+1\rangle\}$)

$$\hat{U} = \frac{1}{\sqrt{2}} \begin{bmatrix} \tan\theta & -1 & -\sqrt{1-\tan^2\theta} \\ \tan\theta & 1 & -\sqrt{1-\tan^2\theta} \\ \sqrt{2(1-\tan^2\theta)} & 0 & \sqrt{2}\tan\theta \end{bmatrix}. \tag{3.16}$$

We decompose this operation into two rotations [136, 137], which each act on only one spin transition. The decomposition is given by $\hat{U} = \hat{T}_{0,-1}\hat{T}_{0,+1}$, with

$$\hat{T}_{0,-1} = \frac{1}{\sqrt{2}} \begin{pmatrix} 1 & -1 & 0 \\ 1 & 1 & 0 \\ 0 & 0 & \sqrt{2} \end{pmatrix}, \tag{3.17}$$

$$\hat{T}_{0,+1} = \begin{bmatrix} \tan\theta & 0 & -\sqrt{1-\tan^2\theta} \\ 0 & 1 & 0 \\ \sqrt{1-\tan^2\theta} & 0 & \tan\theta \end{bmatrix}. \tag{3.18}$$

$\hat{T}_{0,+1}$ corresponds to a $\theta_1 = 2\arcsin(\sqrt{1-\tan^2\theta})$ rotation on the $m_\mathrm{I} = |0\rangle \leftrightarrow |+1\rangle$ transition and $\hat{T}_{0,+1}$ to a $\pi/2$ rotation on the $m_\mathrm{I} = |0\rangle \leftrightarrow |-1\rangle$ transition. As above, finally a π rotation on the $m_\mathrm{I} = |0\rangle \leftrightarrow |+1\rangle$ transition is applied. This has the additional effect that if the pulse sequence is not successful due to e.g. imperfect electron spin initialization, the result will be inconclusive. For the final measurement, a positive result on $m_\mathrm{I} = |0\rangle$, $|-1\rangle$, and $|+1\rangle$ corresponds to $|?\rangle$, $|a\rangle$, and $|b\rangle$, respectively, where $|?\rangle$ indicates the inconclusive result. Here, the average detection efficiency was $\approx 90.2\%$.

Method	d	unambiguous	error %	efficiency %
SUSD	2	yes	~ 3.5	84.6
IDP	3	yes	$4 - 7.5$	90.2
Helstrom	2	no	> 3.5	83.1

Table 3.1.: Comparison of the three implemented measurement protocols. Column d is the needed dimension of the Hilbert space. The Helstrom measurement has an inherent error probability; here we show the minimum error due to measurement imperfections.

Results Table 3.1 compares the three implemented measurement protocols. Fig. 3.4 shows the measurement results. The probability of obtaining a correct results is $p_\mathrm{corr} = p(a|a)p_a + p(b|b)p_b$, where $p(i|j)$ is the conditional probability to get result i if state j was prepared, and p_a, p_b are the initial state probabilities for $|a\rangle$, $|b\rangle$, respectively. Likewise, the probability for an incorrect result is $p_\mathrm{err} = p(b|a)p_a + p(a|b)p_b$, and for an inconclusive result $p_? = p(?|a)p_a + p(?|b)p_b$.

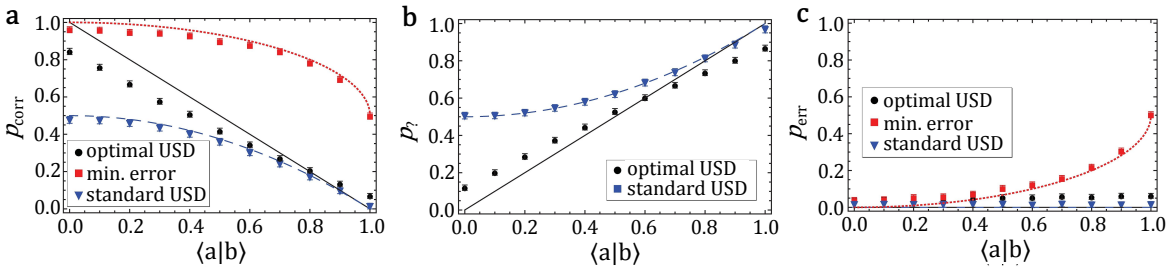

Figure 3.4.: Measurement results. **a**, Probability for correct result $p_{\text{corr}} = p(a|a)p_a + p(b|b)p_b$. **b**, Probability for inconclusive result $p_? = p(?|a)p_a + p(?|b)p_b$. **c**, Probability for incorrect result $p_{\text{err}} = p(b|a)p_a + p(a|b)p_b$. The solid / dotted lines show the expected result for ideal measurements.

A main drawback of the standard USD is that only one state can be probed, i.e. if the system is initially in the other state, the result will always be inconclusive. This can be seen in fig. 3.4a, b: The probability for a correct result is at most 0.5, and the probability for an inconclusive result always > 0.5. For optimal USD, both states can be probed independently, leading to better results for p_{corr} and $p_?$. However, due to the increased experimental complexity the error probability is slightly increased, see fig. 3.4c and table 3.1.

An important comparison is the probability for an incorrect result p_{err} of the USD and the minimum error measurement. Ideally, for USD there should be no incorrect results, whereas these are expected for the minimum error measurement. Nevertheless, due to experimental imperfections there will be incorrect results for all measurement protocols. Fig. 3.4c shows that for small overlap $\langle a|b\rangle$, p_{err} is similar for all three implementations, and mainly limited by the readout fidelity for the minimum error measurement. Only for larger overlap $\langle a|b\rangle$, p_{err}, the intrinsic p_{err} of the minimum error measurement dominates. On the other hand, the probability of a correct result for the minimum-error measurement is higher than for USD, as expected.

Conclusions Here, we have implemented generalized measurements for the first time in solid state qubits, which has previously only been done optically [138, 139]. This was achieved by making use of the qutrit character of the ^{14}N nuclear spin. The ability to perform these type of measurements is of interest for QIP, and confirms this potential application of the NV.

3.3. High-dynamic-range magnetometry

A promising application of the NV is sensing of magnetic fields and other physical values, e.g. electric fields and temperature. These sensing methods are based on measuring energy shifts of the NV's spin state transitions, i.e. shifts of the Lamor frequency, via phase accumulation [25, 23, 24]. The Lamor frequency can be measured efficiently by Ramsey interferometry, also called free induction decay (FID), see section 1.3.1. Thereby, a coherent superposition of two spin states can be generated via a $\pi/2$ pulse. In the rotating frame of the rf signal, the phase of this superposition will evolve with the frequency difference of the rf and the Lamor frequency, such that the state rotates around the z-axis of the Bloch sphere. After a waiting time τ, a second $\pi/2$ pulse rotates the state around the same axis as the first pulse, and thereby maps the phase ϕ accumulated during the waiting time τ onto the eigenstate populations of the spin, which is then obtained by measurement. For magnetic field sensing, the frequency difference ω of the rf and the Lamor frequency is proportional to magnetic field changes $\underline{B}$ due to the Zeeman interaction, such that

$$\omega = \frac{\phi}{\tau} \propto \gamma \underline{B} \cdot \underline{\hat{S}} \tag{3.19}$$

where γ is the spin's gyromagnetic ratio and $\underline{\hat{S}}$ the spin operator.

In section 3.3.1, we show the accuracy scaling and ambiguity behavior of Lamor frequency-based measurements. We will see that for high sensitivity measurements, long phase accumulation times τ are desired, whereas short phase accumulation times yield a large accessible range (e.g. magnetic field range with unambiguous results) for the sensor. This contradiction can be tackled by a so called quantum phase estimation algorithm (QPEA), which is introduced in section 3.3.2. Finally, this algorithm will be implemented experimentally on the ^{14}N of the NV, see section 3.3.3.

The results of this section have been published in [45]. A similar study which uses the electron spin of the NV for implementation of the QPEA, however, without single shot readout, was published in [140].

3.3.1. Accuracy scaling and ambiguity

The accuracy of Ramsey based phase estimation is limited by the final readout for determining the state populations. For single shot readout, the signal contrast is given by the readout fidelity, and the noise for this measurement is quantum shot noise, because of the probabilistic nature of quantum mechanics, which are both independent of the

phase accumulation time τ [1]. The accuracy σ of the frequency ω in eq. (3.19) is therefore

$$\sigma \propto \frac{1}{\tau}. \tag{3.20}$$

In principle, increasing the total measurement time T by increasing τ yields the $1/T$ limit of the precision. However, the phase accumulation time τ is limited by the coherence time T_2 (for AC magnetometry) of the spin. This yields the highest achievable precision of $\sigma \propto 1/T_2$ for a single measurement. Upon repeating measurements with phase accumulation time τ, the final precision scales as

$$\sigma \propto \frac{1}{\tau\sqrt{N}} = \frac{1}{\sqrt{T\tau}} \tag{3.21}$$

where N is the number of repetitions. In the following, we refer to eq. (3.21) as the $1/\sqrt{T}$ limit, where $T = \tau N$ is the total measurement time. Here, the time needed for initialization and readout of the system is ignored, as we are interested in the performance of our algorithm, independent of the details of the implementation. The relationship eq. (3.21) does not only apply to phase measurements, but to any sensor whose precision is limited by only quantum shot-noise (statistical noise), according to the central limit theorem. Due to this fundamental mathematical relationship of the measurement precision with the total measurement time, the achievable precision is usually given in terms of sensitivity, which is obtained by multiplying the achieved precision σ with the square-root of the total measurement time T. Here, in the case of magnetometry based on phase estimation, the magnetic field sensitivity δB is

$$\delta B \propto \sigma\sqrt{T} \propto \frac{1}{\tau}\frac{1}{\sqrt{N}}\sqrt{T} = \frac{1}{\sqrt{\tau}}, \tag{3.22}$$

where we used eq. (3.20), eq. (3.21) and $T = \sqrt{\tau N}$.

These $1/\sqrt{T}$ limit and $1/T$ limit are exemplified in fig. 3.5, where the square of the sensitivity δB is plotted versus the total phase accumulation time T. In a real experiment, the achieved sensitivity will be reduced by the limited measurement fidelity and decoherence of the spin. This leads to an overhead compared to the limits, which is why only $1/\sqrt{T}$ or $1/T$ scaling is observed.

Due to the periodicity of the phase signal, the phase and magnetic field estimates will be ambiguous. This means that the phase accumulation time τ must be chosen such that the maximum magnetic field $B_{\max}$ leads to a phase accumulation of at most $\phi_{\max} = \pi$, where

$$B_{\max} \propto \frac{1}{\tau}, \tag{3.23}$$

[1] Note that the quantum shot noise actually depends on the state populations, i.e. on the accumulated phase. This effect, however, is countered by the dependency of the state population on the phase, which is weak for points where the shot noise is low. Nevertheless, these considerations can be neglected for an unknown phase accumulation frequency.

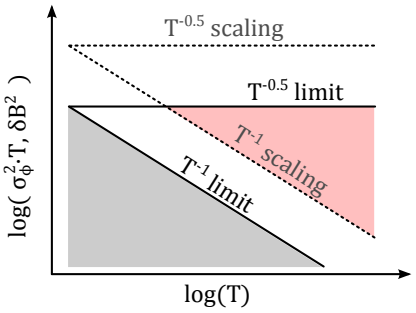

Figure 3.5.: Schematic limits and scaling of Ramsey based phase estimation.

cf. eq. (3.19). As can be seen from eq. (3.22) and eq. (3.23), the maximum magnetic field decreases faster with the phase accumulation time than the sensitivity. The dynamic range, which is the maximum field divided by the sensitivity, therefore decreases with $\sqrt{\tau}$. As an example, for an achieved sensitivity of $4\frac{\mathrm{nT}}{\sqrt{\mathrm{Hz}}}$ with the NV [22], the accessible field range is only $\Delta B \in [-31\mathrm{nT}, 31\mathrm{nT})$. If this prior information of the maximum magnetic field is not available, the phase accumulation time τ has to be decreased, which in turn decreases the sensitivity.

3.3.2. Quantum phase estimation algorithm

Recently, algorithms for improved phase estimation with photons were introduced in the context of Heisenberg limited measurements [141, 142, 143], and also proposed for the NV [144]. To achieve both high sensitivity according to eq. (3.22) and unambiguous field measurements according to eq. (3.23), weighted measurements with different phase accumulation times τ_k are performed. The sensing times are chosen as

$$\tau_k = \tau_0 2^k, \quad k = 0, 1, ..., K. \tag{3.24}$$

In our case, we set $\tau_0 = 20\mu$s, which was technically limited by the experiment (see section 3.3.3). In the following, we express the total measurement more generally by the number of resources N, where one resource is $N = 1 \mathrel{\widehat{=}} \tau_0$, as this is the minimal phase accumulation time. The weighting is implemented by adjusting the number of measurement repetitions M at each τ_k by

$$M_{(K,k)} = M_K + F(K - k). \tag{3.25}$$

Here we use $M_K = 36$ and $F = 8$. The total number of resources N_K and the total measurement time T_K depending on K are

$$\begin{aligned} N_K &= \sum_{k=0}^{K} M_{(K,k)} \cdot 2^k \\ T_K &= \tau_0 \cdot \sum_{k=0}^{K} M_{(K,k)} \cdot 2^k = \tau_0 \cdot N_K, \end{aligned} \tag{3.26}$$

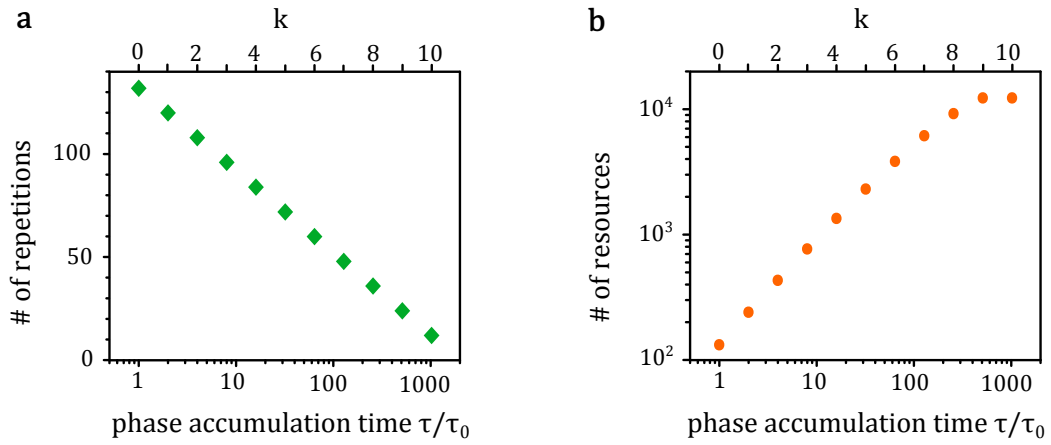

Figure 3.6.: QPEA algorithm. **a**, Number of measurement repetitions $M_{(K,k)}$ for each τ_k according to eq. (3.25). **b**, Number of resources $M_{(K,k)} \cdot 2^k$ for each τ_k.

Even though the number of measurement repetitions decreases for longer phase accumulation times τ according to eq. (3.25), most the the measurement resources (i.e. time) are still expended on the longest and most sensitive measurements, see fig. 3.6. Additionally, a controlled phase shift θ_C is introduced, to determine the phase ϕ modulo 2π. Here, we implement fixed phase shifts of 0, $\pi/2$, π, $3\pi/2$. Another possibility are adaptive phase shifts with feedback from the measurement results [144], which is not implemented here for technical reasons.

To obtain the final estimate for the phase, a most-likelihood estimation is performed. For each repetition of the Ramsey experiment the final state of the system is measured, which yields either 0 or 1. These results provide information about the accumulated phase ϕ according to the probability distribution [144]

$$P(\pm 1|\phi) = \frac{1}{2}\left[1 \pm (1-2F^2)\mathrm{e}^{\tau_k/T_2}\cos(2^k\phi - \theta_C)\right], \tag{3.27}$$

where $P(\pm 1|\phi)$ is the conditional probability that the accumulated phase is ϕ given that the measurement yielded result ± 1, F is the measurement fidelity and T_2 the coherence time. The final probability distribution of the algorithm is obtained by multiplication of the single probability distributions eq. (3.27) as

$$P(\phi) = \prod_i P_i(m_i|\phi), \tag{3.28}$$

where m_i is the i'th measurement results. The maximal point of this distribution is taken as the final result for the phase estimate ϕ.

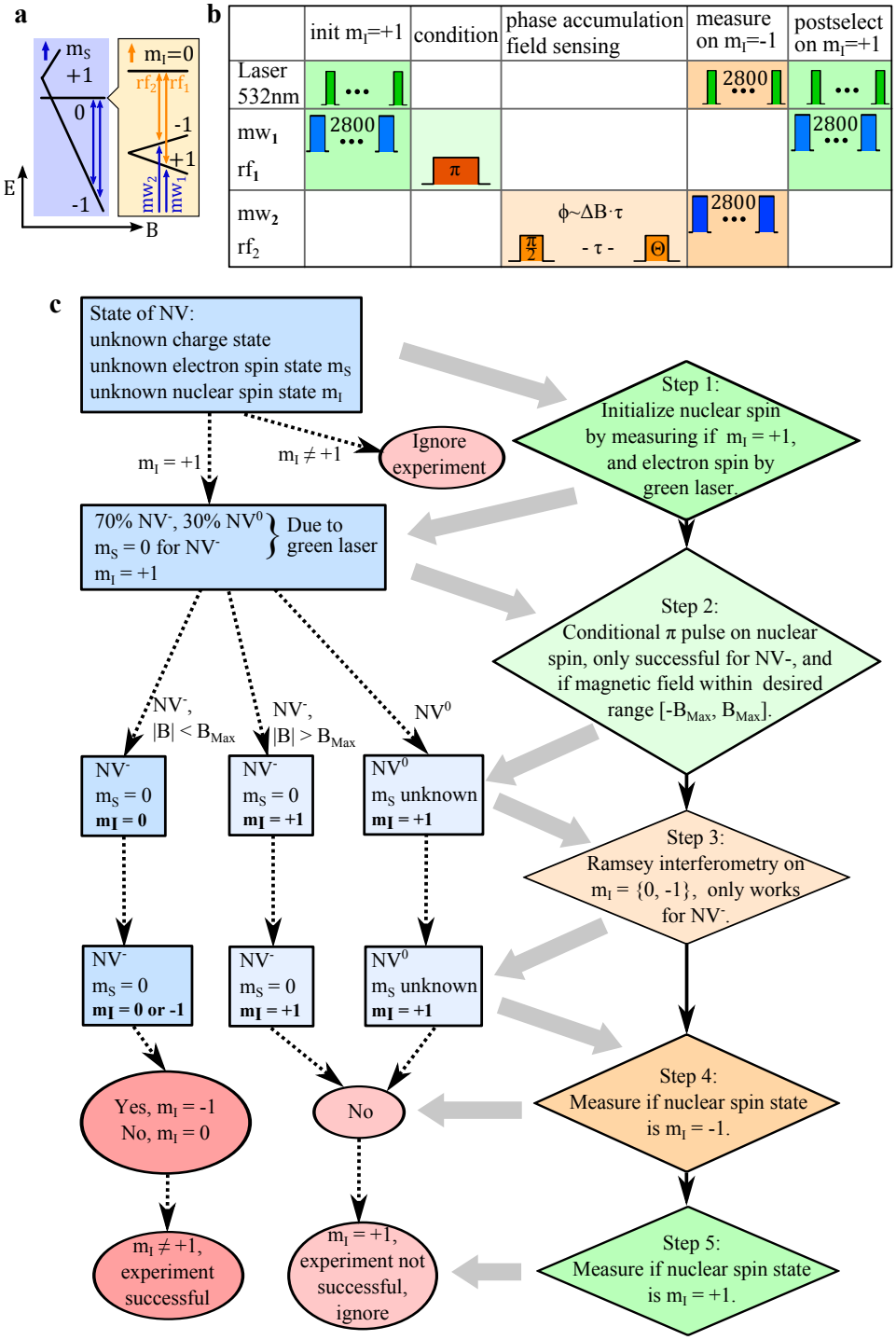

Figure 3.7.: Full sequence for Ramsey interferometry. **a**, Energy level scheme and used transitions. **b**, Full pulse sequence. **c**, Flow chart of the measurement and analyzation logic (see text)

3.3.3. Experimental implementation of the QPEA

Here, we implement the QPEA introduced in section 3.3.2 on the ^{14}N nuclear spin of the NV, and employ single shot readout (see section 1.2.4) to achieve quantum limited measurements. As a first step, we perform a Ramsey experiment with varying phase accumulation time τ. In addition to the measurement preselection for initialization of the nuclear spin, we also develop a new method to postselect the experiment for the negative charge state NV$^-$. This method exploits the qutrit states of ^{14}N . The full measurement and pulse sequence is shown in fig. 3.7. First, the ^{14}N spin is initialized into $m_N = +1$ by single shot measurement. Then, a π rotation with rf_1 is performed on the $m_N = +1 \leftrightarrow 0$ transition. This rotation will only work if the NV is in the correct electronic state NV$^-$ and $m_S = 0$, i.e. if the driving field is in resonance with the nuclear spin transition. The actual QPEA experiment is carried out in the $m_N = \{0, -1\}$ subspace with rf_2. Finally, two single shot measurements are performed. The first measurement is on $m_N = +1$. If the spin is still in this state, the previous π rotation did not work, from which we infer that the NV was not in the correct electronic state. The second measurement is on $m_N = -1$, and yields the actual result of the experiment, which is discarded if the NV was in the wrong state according to the first measurement. Note that this postselection technique can also be used to limit the magnetic field range to which the sensor is sensitive. The frequency range of the rf_1 π pulse can be adjusted by either the used rf power, or by optimal control (cf. section 1.3.2). If the magnetic field is then not within the desired range, the pulse will not work and the measurement results are omitted.

Fig. 3.8 shows the result of a Ramsey experiment on the ^{14}N nuclear spin with the above described measurement sequence. From this measurement, we can extract the contrast of the Ramsey fringes of $1 - 2F^2 = 0.79$ and the coherence time $T_2 = 7.25$ ms, which are both needed to calculate the probability distribution eq. (3.27). Due to the finite length of the $\pi/2$ pulses, an additional phase is accumulated during these pulses, even for a phase accumulation time $\tau = 0$, see fig. 3.8b. This phase corresponds to an additional, fixed phase accumulation time ϵ, such that the total phase accumulation time $\tau' = \tau + \epsilon$. Here, $\epsilon = 20$ μs, which also limits the smallest phase accumulation time τ_0. In the following, we omit the dash of τ' and refer to the total phase accumulation time as τ.

Fig. 3.9a shows an example probability distribution of the phase / magnetic field estimate for one run of the QPEA. It illustrates that measurements with small k (short τ_k) remove ambiguity, while measurements with large k (long τ_k) yield high sensitivity. The precision is determined empirically by repeating the algorithm many times, and for each run take the maximal point of the distribution as the result, see fig. 3.9b. From the histogram of estimation results, we calculate the standard deviation of one single run of the QPEA. Note that the standard deviation of one single run could also be calculated directly from the obtained probability distribution. During this measurement, fluctuations of the magnetic field can occur due to thermal drifts of the permanent magnet,

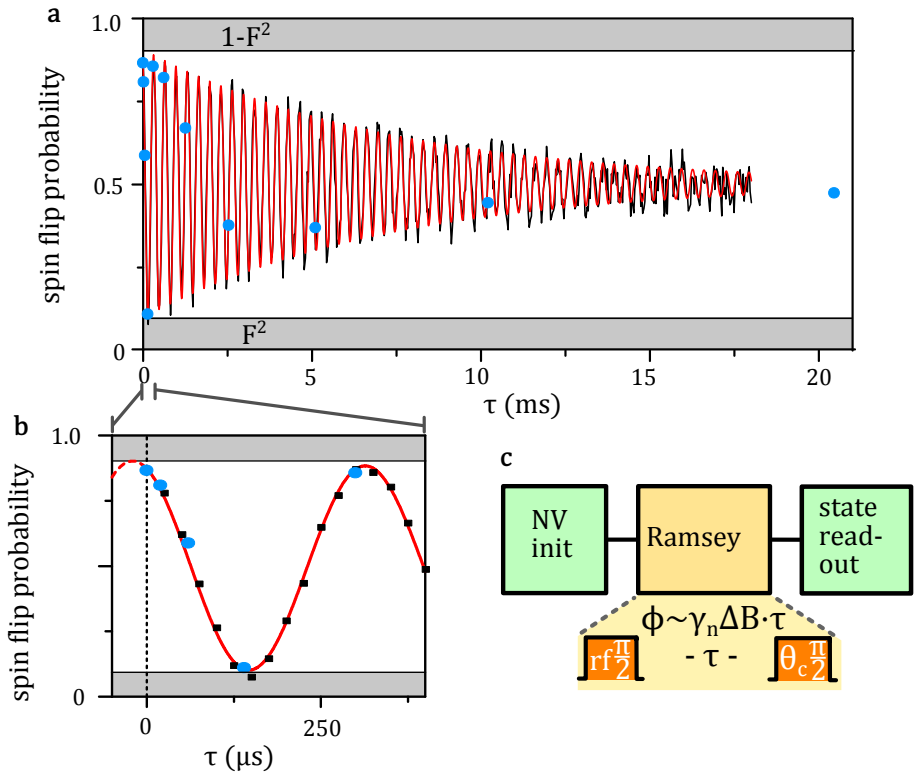

Figure 3.8.: Ramsey fringes. **a**, Result of the Ramsey experiments on the ^{14}N nuclear spin. The black line are the measurement results, and the red line a cosine fit $\frac{1}{2}\left[1 \pm (1-2F^2)\mathrm{e}^{\tau/T_2}\cos(\omega\tau)\right]$. Here, $1-2F^2 = 0.79$ and $T_2 = 7.25$ ms. The blue dots are the measurement points used for the QPEA. **b**, Magnification of the Ramsey fringes for small τ, such that the fixed offset off 20 μs due to the length of the $\pi/2$ is visible. **c**, Schematic Ramsey sequence.

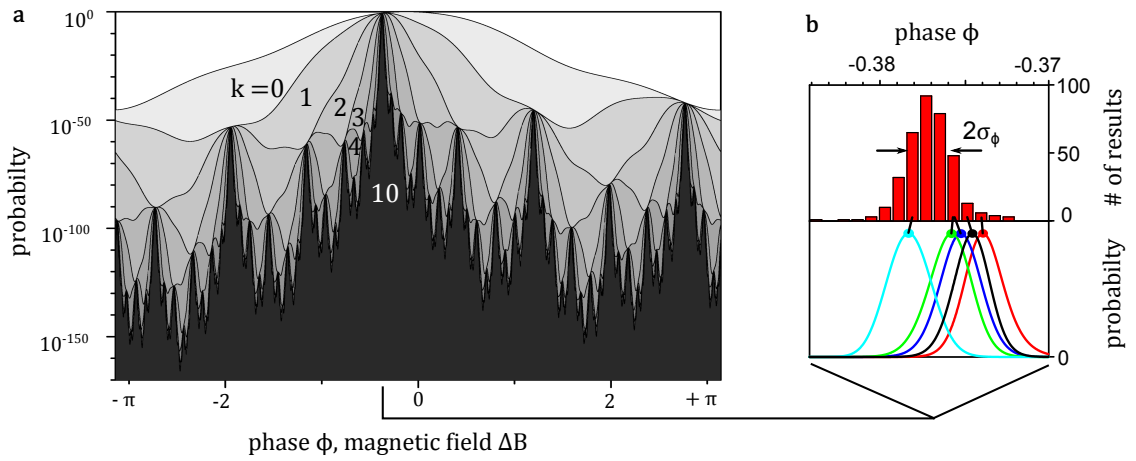

Figure 3.9.: QPEA analyzation. **a**, Probability distribution of the phase / magnetic field estimate during one run of the QPEA, by increasing $k = 0, 1, ..., K$ ($K = 10$). **b**, Lower part: Magnification of the probability distribution (with linear scale) at the region of the maxima for several runs of the QPEA. Upper part: Histogram of measurement results obtained from the maximal point of each run of the QPEA.

such that the obtained variance would be limited by these fluctuations. Therefore, we use the much more sensitive electron spin to periodically determine the current magnetic field, and adjust the rf according to the Zeeman shift of the nuclear spin states. By doing so, the frequency difference of the rf and the Lamor frequency is kept constant, and the pure statistical variance of the estimate can be measured.

To analyse the precision scaling of the QPEA, we increase the total measurement time T by increasing the parameter K, see section 3.3.2. The relationship between the standard deviation of the magnetic field (σ_B) and of the phase (σ_ϕ) is

$$\sigma_B = \frac{\sigma_\phi}{\gamma_N \tau_0}, \tag{3.29}$$

where γ_N is the gyromagentic ratio of ^{14}N . The field sensitivity δB is

$$\delta B = \sqrt{\sigma_B^2 T}. \tag{3.30}$$

Fig. 3.10a shows the sensitivity scaling of the standard measurement approach compared with the QPEA. The precision of the standard measurement scales with $1/\sqrt{T}$ (constant sensitivity), as expected. For the QPEA, we find a precision scaling of $1/T^{0.85}$, such that the precision of the QPEA surpasses the $1/\sqrt{T}$ quantum limit. Besides the vertical offset of the sensitivity due to limited readout fidelity and decoherence, there is also an additional horizontal overhead of the QPEA compared to the $1/T$ limit due to the measurement with short τ_k, which remove the ambiguity. The increase of the sensitivity of the QPEA at the last two points is because τ_k becomes larger than the coherence time

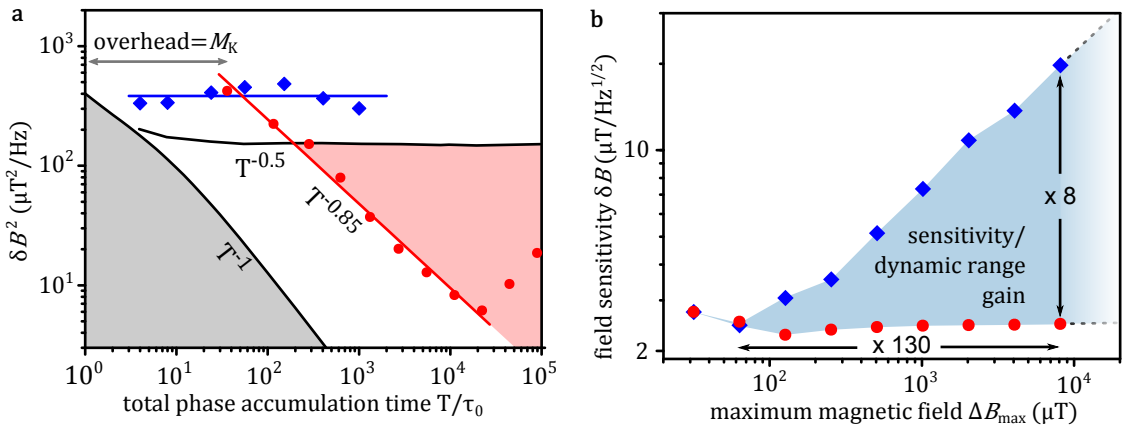

Figure 3.10.: Scaling and dynamic range of QPEA and standard measurement. **a**, Sensitivity scaling of the standard measurement by repeating Ramsey interferometry with only τ_0 (blue diamonds), and sensitivity scaling of the QPEA (red dots, calculated from 358 runs). Black lines are the quantum limits (see section 3.3.1), which were calculated by assuming 100 % measurement fidelity and no decoherence. **b**, Sensitivity and maximum magnetic field of standard measurement (blue diamonds) and of the QPEA (red dots).

$T_2 = 7.25$ ms (cf. fig. 3.8).

The advantage of the QPEA compared to the standard measurement is that both maximal sensitivity and high dynamic range can be achieved. This is illustrated in fig. 3.10b. It shows the magnetic field sensitivity of both the QPEA and the standard measurement, depending on the maximal magnetic field $\Delta B_{\max}$. As explained in section 3.3.1, the sensitivity of the standard measurement becomes worse as $\Delta B_{\max}$ is increased, which is due to the decrease of the sensing time τ_0. For the same maximal magnetic field, the sensitivity of the QPEA is a factor of 8 better than that of the standard measurement. Vice versa, for the same sensitivity, the dynamic range of the QPEA is a factor of 130 larger compared to the standard measurement.

3.3.4. Conclusion

We have experimentally demonstrated that a quantum phase estimation algorithm can be applied to improve the dynamic range of magnetic field measurements, by increasing either the maximal magnetic field for a given sensitivity, or increasing the sensitivity for a given maximal magnetic field, compared to the standard measurement. In our case, the maximal magnetic field range is technically limited by available rf power, which leads to a smallest phase accumulation time $\tau_0 = 20\ \mu$s due to the finite length of the pulses. A possibility to increase this range besides the rf power is optimal control, which has been applied in [145]. Here, we relied on the nuclear spin for field sensing to show and apply the basic principle of the QPEA. The electron spin would be more suitable for practical

field sensing due to its factor ≈ 9000 higher gyromagnetic ratio. This could even be combined with single shot readout of the nuclear spin, by mapping the electron spin state onto the nuclear spin after the Ramsey interferometry, and subsequent readout of the nuclear spin.

4. Quantum register based on single nuclear spins: Quantum error correction

Nuclear spins in the vicinity of an NV can provide a powerful resource to increase the versatility of a single NV. This has already been exploited in the previous chapters, where projective measurements of the nitrogen nuclear spin via quantum logic readout was applied. Especially for quantum information processing (QIP) with the NV, nuclear spins can prove to be of high importance. Due to the extreme isolation of nuclear spins from the environment, nuclear spin resonance (NMR) has enabled many proof-of-principle experiments for QIP [9]. However, ensemble based NMR imposes several drawbacks for scalable QIP, see section 1.1. The extreme isolation of nuclear spins makes direct measurements of single nuclear spins impossible with conventional technology using pick-up coils. Here, hybrid spin systems with coupled electron and nuclear spins are a promising approach. Thereby, the electron spin provides readout, non-local control and scalability, whereas the nuclear spins can be used as long-lived qubits. For the NV, nuclear spins are provided by nearby ^{13}C atoms in the diamond lattice, apart from the always-present ^{14}N nuclear spin.

In this chapter, we will implement a fully-functional nuclear spin register based on the NV, where the NV electron spin provides access to the single nuclear spins. Fully-functional means that we can initialize the whole register, perform projective readout of individual qubits, and can implement fast local and non-local gates, i.e. have universal control of the register. With the potential scalability of NV center arrays [50, 49], these features address all requirements needed for scalable QIP. In section 4.1, we show that projective readout of multiple ^{13}C nuclear spin with a single NV is possible. We use this projective readout combined with swap-like gates from the electron spin to the nuclear spins for high-fidelity initialization of the register, see section 4.2. Non-local control of the nuclear spins is realized by exploiting the hyperfine interaction with the electron spin, as explained in section 4.3. Optimal control allows for high-fidelity implementation of the non-local gates (section 4.4). Finally, in section 4.5 we will utilize these tools to implement phase flip quantum error correction (QEC) on a three-qubit nuclear spin register. Furthermore, we will analyze the number of usable ^{13}C spins (section 4.6), and demonstrate detection of a so-called weakly coupled ^{13}C spin at high magnetic fields (section 4.7).

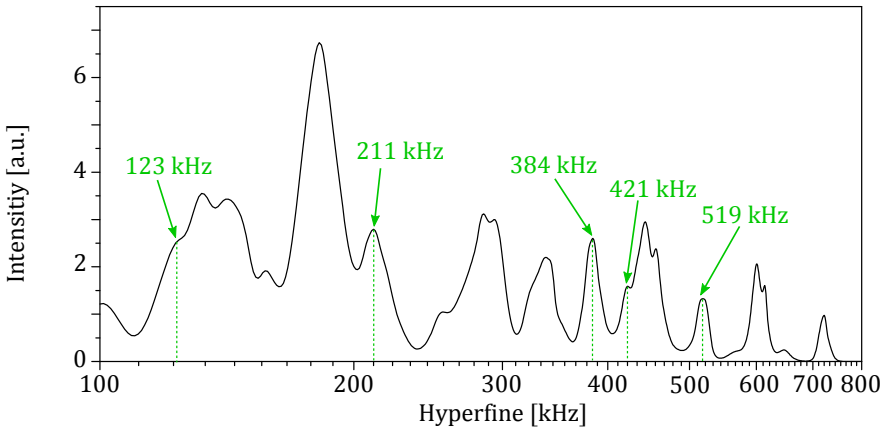

Figure 4.1.: Hyperfine probability spectrum. Hyperfine spectrum as explained in the text. Only hyperfine values with a relative error of less than 4% were used, such that hyperfine values which are close-by to each other can be resolved. Values indicated in green are suitable for single shot readout at around 5000 Gauss and fluorescence count rates of around 200 kcounts/s.

The results of this chapter are published in [48].

4.1. Single shot readout of ^{13}C nuclear spins

Projective, single-shot readout of ^{13}C nuclear spins can be achieved in a similar fashion as for the ^{14}N nuclear spin, by repetitively mapping the state of the nuclear spin onto the electron, and subsequent optical readout of the electron spin. In order to map the ^{13}C nuclear spin state onto the electron spin by a mw pulse, the coupling between nuclear and electron spin must be larger than linewidth of the electron transition (so-called strong coupling). Additionally, a long lifetime of the nuclear spin during the optical cycle of the NV is required, see section 1.2.4. Furthermore, the duration of non-local gates scales inversely with the hyperfine interaction, i.e. stronger hyperfine interaction enables faster non-local gates. Therefore, we use a diamond with 0.2 % ^{13}C content. This value is a compromise for strongly coupled ^{13}C spins being robust against electron spin flips, but still enabling non-local gates much faster than the electron T_2 and T_1 times.

To find ^{13}C nuclear spins positions suitable for single shot readout (SSR), we acquired statistics of possible ^{13}C hyperfine splittings for almost 3300 NVs. For each analyzed NV, the EPR spectrum is measured, e.g. as shown in Fig. 4.3b. A multi-peak function fit was used to determine hyperfine interactions larger than approximately 100 kHz, as the line width of the transition is around 50 kHz FWHM. These measurements where performed at magnetic fields of around 10 Gauss. However, the magnetic field was not aligned for all NVs, which can slightly alter the measured hyperfine interaction compared to the value at zero field or at small, aligned magnetic fields. The deviation is expected to be below 2.5 % (in the worst case of pure dipolar hyperfine interaction, unfavorable

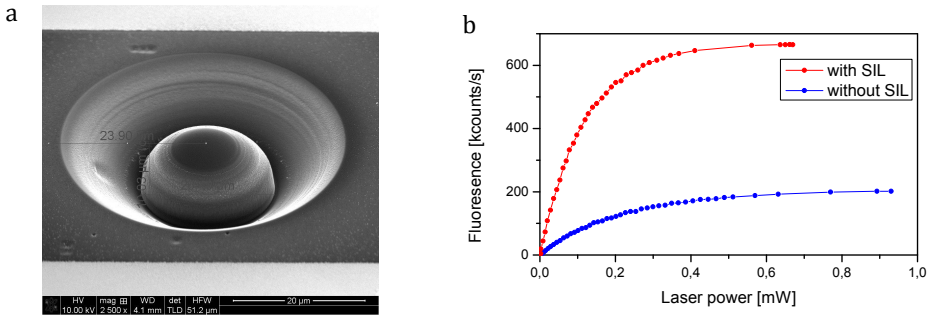

Figure 4.2.: Solid immersion lens. **a**, Scanning electron microscope picture of the SIL. **b**, Fluorescence saturation curves of the same NV with and without SIL

^{13}C position and perpendicular magnetic field). Finally, we can create a hyperfine probability spectrum in the following way: For each observed hyperfine interaction, we take a Gaussian distribution at the center of the observed value, and a standard deviation according to the fit accuracy. Summing up over all measured values results in the spectrum shown in Fig. 4.1. By trying to perform single shot readout on these ^{13}C spins, we found that the hyperfine splitting (in kHz) of 124, 211, 384, 422, 517 are usable for single shot readout at magnetic fields of around 0.5 T, with spin lifetimes (in readout steps) comparable to or better than ^{14}N [41].

4.2. Three-qubit nuclear register: Readout and initialization

Figure 4.3a illustrates our hybrid spin register, which consists of the NV electron spin, the ^{14}N nuclear spin ($I = 1$), and two ^{13}C nuclear spins ($I = \frac{1}{2}$) with hyperfine interactions of 413 kHz ($^{13}C_1$) and 89 kHz ($^{13}C_2$). Figure 4.3b shows the hyperfine splitting of the electron $m_S = 0 \leftrightarrow -1$ transition into 12 individual lines, corresponding to the 12 states of the nuclear register. A magnetic field of around 6200 Gauss that is applied parallel to the symmetry axis of the NV decouples the dynamics of the nuclear spins from the electron spin, which is necessary for single shot readout (cf. section 1.2.4). Additionally, to improve the readout fidelities and reduce the measurement time, we created a solid immersion lens (SIL) within the surface of the diamond [146]. This inhibits fluorescence photon losses due to total internal reflection at the diamond surface, thus increasing the detected fluorescence count rate. A picture of the SIL is shown in fig. 4.2a. The SIL increases the detected fluorescence by a factor of > 3.

Similar to the single shot readout of the ^{14}N (see section 1.2.4), we can map any eigenstate of the nuclear register onto the electron spin. This is achieved by applying frequency selective microwave (mw) π-pulses resonant with the corresponding transition lines of the electron (see fig. 4.3b), which yields a C_nNOT_e operation. For example,

multiple mw pulses can be applied onto all lines corresponding to the state of one nuclear spin, in order to map the state of this nuclear spin onto the electron spin, see fig. 4.3c. Fluorescence time traces of the NV while performing repetitive readout of the three nuclear spins are shown in fig. 4.3d. Fig. 4.3d also shows histograms of the measurement results. We can see the two distinct fluorescence levels corresponding to different nuclear spin states, which enables single shot readout. The achieved single shot readout fidelities are 95.8 % for ^{14}N , 96.9 % for $^{13}C_1$ and 99.6 % for $^{13}C_2$. For the following experiments, we did not read out the separate nuclear spins as shown in fig. 4.3d, but rather directly probe one state of the total register, by applying the C_nNOT_e gate in fig. 4.3c on only one transition shown in fig. 4.3b. The average readout fidelity of the whole register after the post-selection measurement (see below) is ≈ 89 %.

Nuclear spin initialization To initialize the nuclear register, we use a combination of projective readout and swap-like gates with the electron spin. The full pulse sequence for this is shown in fig. 4.3e, under 'nuclear initialization'. The main drawback of measurement-based initialization is that it is a probabilistic method, which does not allow deterministic state initialization. Especially for an increasing number of systems, the probability of successful initialization decreases exponentially. However, we can map the initialized state of the electron spin (which can be initialized deterministically) onto the nuclear spins [38]: First, the state of the nuclear spin is mapped onto the electron via a C_nNOT_e gate (as described above). Then, a C_eNOT_n gate is applied to map the electron spin state onto the nuclear spin. Finally, a laser pulse re-polarizes the electron spin into $m_S = 0$. Effectively, the two gates flip the nuclear spin only if it is in one state (e.g. in $|1\rangle$, leaving it unaffected if it already is in the desired state (here $|0\rangle$). The polarization efficiency of the whole register with this sequence is around 50 %, owing to the finite probability of the NV being in NV^- (around 70 %) and limited pulse fidelities.

As explained in section 1.2.4, the initialization fidelity can be increased by shifting the photon count threshold for single shot readout to lower photon count numbers. Due to the overlap of the photon count distributions of the two fluorescence levels, photon count numbers that are close to the threshold have a higher probability to give a wrong result. By using a lower initialization threshold, these results are thrown away, and only photon count values with a high probability to yield the correct spin state are used. However, this pre-selection of initialization measurement comes at the expense of reduced initialization probability. To get an estimate of the initialization fidelity into state $|^{14}\mathrm{N},^{13}\mathrm{C}_1,^{13}\mathrm{C}_2\rangle = |+1,0,0\rangle$, a second single shot measurement after the initialization sequence shown in fig. 4.3e is needed. First, an estimate of the fidelity of this second measurement is made. By using the same threshold for both single shot measurements, the measured conditional probability of finding the system in state $|\psi\rangle = |+1,0,0\rangle$ for the second measurement if it was in this state for the first measurement is $p(\psi|\psi) \approx F_0^2$, where F_0 is the fidelity of a single measurement. Then, the threshold for the first initialization measurement is shifted, and the above defined conditional probability is now $p_{\mathrm{shift}}(\psi|\psi) \approx F_{\mathrm{init}}F_0$,

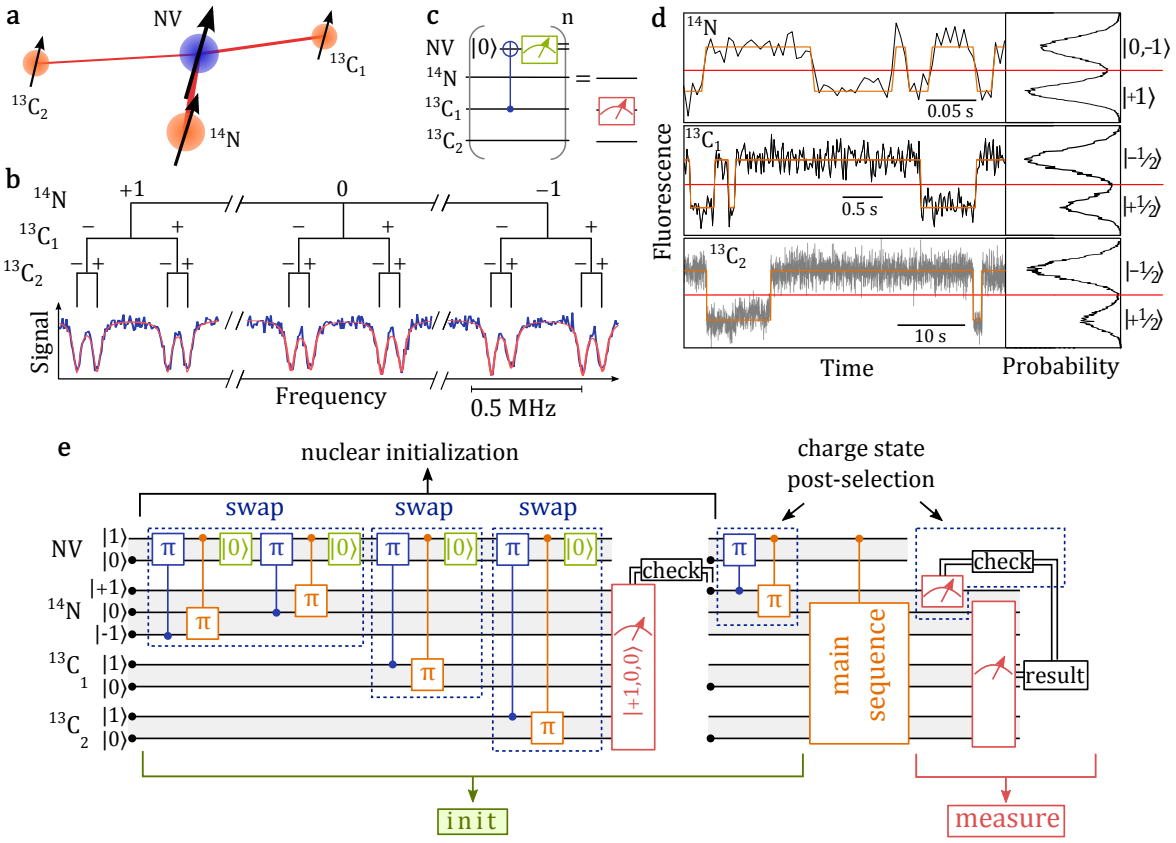

Figure 4.3.: NV based hybrid electron and nuclear spin register. **a**, Illustration of the quantum register consisting of three nuclear spins hyperfine (hf) coupled to the central NV electron spin, enabling nuclear spin readout and entanglement. **b**, Hyperfine splitting of the $m_S = 0 \leftrightarrow -1$ transition into 12 individual lines (^{14}N: 2.16 MHz, $^{13}C_1$: 413 kHz, $^{13}C_2$: 89 kHz). Each line can be individually driven, which allows for electron spin state manipulation depending on the state of the nuclear register. Here, $|-\rangle$ and $|+\rangle$ correspond to ^{13}C nuclear spin state $|m_C = -\frac{1}{2}\rangle$ and $|m_C = +\frac{1}{2}\rangle$, respectively. **c**, Wire diagram for the projective readout of the nuclear spins, here exemplified for the $^{13}C_1$ spin (see text and section 1.2.4). **d**, Left side: Time trace of the NV fluorescence during repetitive readout of the corresponding nuclear spin as shown in c. The jumps indicate flips of the nuclear spin, and show that the readout of all nuclear spins is much faster than the flip rate, which allows for projective readout. Right side: Histograms of measurement results of the time traces and threshold for single-shot readout. For initialization, the threshold can be shifted down to increase the initialization fidelity, at the expense of the rate of successful initialization events. **e**, Base sequence for initialization of nuclear spins and charge state post-selection (see text). The 'main sequence' step is the actual sequence we want to implement (e.g. entanglement generation and QEC). Black dots on the state lines indicate the qubit state populations.

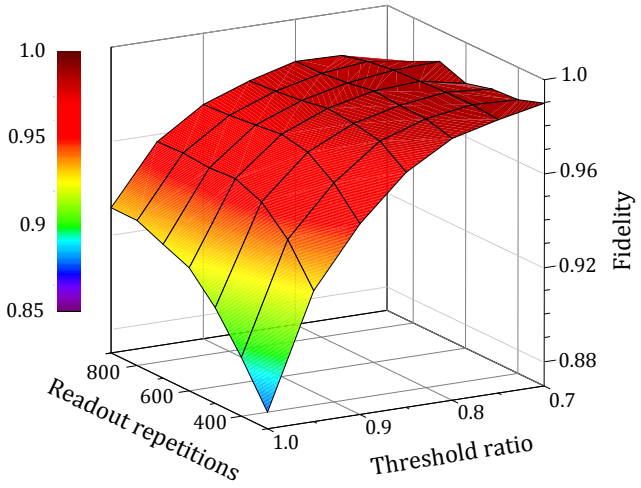

Figure 4.4.: Initialization of the nuclear register. Initialization fidelity of the nuclear register with a combination of swap-like gates with the electron spin and single shot readout (cf. fig. 4.3e) depending on the number of readout pulses and the threshold shift.

yielding the initialization fidelity F_{init}. Fig. 4.4 shows the estimated initialization fidelity using different thresholds for the initialization, depending on the number of readout steps (readout laser pulses).

Electronic initialization As we have seen in Chapter 2, not only the electron spin has to be initialized for QIP, but also the charge state of the NV. Here, we will use a method similar as described in section 3.3, which is based on post-selection of the charge state by exploiting the usually unused third state of the ^{14}N nuclear spin. Thereby, a nuclear spin π rotation conditional on the NV being in its negative charge state is performed. After implementing the actual experiment, the success of this initial state flip can be probed by single shot readout. Here, we use a slightly modified version of this scheme, which is shown in fig. 4.3e as 'post-selection'. First, a frequency-selective electron π pulse at the transition frequency corresponding to the initial nuclear register state is performed, to flip the electron spin into $m_S = -1$. Then, the ^{14}N π rotation conditional on NV$^-$ and on $m_S = -1$ is applied. This allows for post-selection not only on the charge state, but also on the success of the electron π pulse. If, due to thermal drifts of the external magnetic field or due to fluctuations of the Overhauser field, the transition frequency of the electron spin is not within the frequency range of the electron π pulse, the ^{14}N π pulse will not be successful, and the result of the experiment can be discarded.

4.3. Selective and Non-local gates

For universal control of the nuclear register both local gates selective for each qubit and non-local gates have to be applied. By performing the gates in the $m_S = -1$ subspace of the electron spin, all local gates can be applied selectively to each nuclear spin via their distinct hyperfine interaction, see fig. 4.3e.

Non-local gates between nuclear spins are realized via the hyperfine interaction with the electron spin. Due to the low magnetic moment, the interaction between two nuclear spins is too weak to allow for direct conditional state manipulation within the nulcear spin T_2 time, which is limited by the electron spin T_1 of around 7 ms. In principle, non-local gates between two nuclear spins can be implemented in a straightforward manner by a series of CNOT gates implemented by selective π-pulses, as shown in fig. 4.5a. However, this sequence involves coherences on the electron spin while applying gates on the nuclear spins. Because the duration of nuclear gates is longer than the electron T_2^* time (here $T_2^* \approx 9\mu s$), direct implementation of this sequence is not possible. A possible solution would be a combination of dynamical decoupling of the electron spin during implementation of the nuclear spin gate [147]. Instead, here we use an approach that does not rely on nuclear spin manipulation while having coherences on the electron spin. The scheme is based on a controlled $2\pi_x$ rotation of the electron spin conditional on the state of the nuclear register [148], which will change the phase of the state by π. Therefore, this rotation effectively acts as a CPhase gate on the nuclear register, allowing for non-local nuclear spin gates.

An example of how to implement a CNOT gate between two nuclear spins using this CPhase gate is shown in fig. 4.5b. We start with e.g. ^{14}N in state $|\psi\rangle = \alpha\,|0\rangle + \beta\,|1\rangle$ and ^{13}C initialized in $|0\rangle$. Then, a $(-\pi/2)_x$ pulse is applied to ^{13}C , to obtain (excluding normalization)

$$|^{14}N,^{13}C\rangle = \alpha|00\rangle + i\alpha|01\rangle + \beta|10\rangle + i\beta|11\rangle. \tag{4.1}$$

Now, a CPhase gate based on an electron spin $2\pi_x$ rotation conditional on the nuclear spin state being $|11\rangle$ will yield a phase shift of π. This results in the (already entangled) state

$$\alpha|00\rangle + i\alpha|01\rangle + \beta|10\rangle - i\beta|11\rangle. \tag{4.2}$$

A final ^{13}C π_x pulse finishes the CNOT gate and yields

$$\alpha|00\rangle - i\beta|11\rangle. \tag{4.3}$$

A major limitation for the fidelity of this gate is that it must be implemented both spectrally selective to be conditional on the nuclear register state, and at the same time be robust against spectral detuning due to inhomogeneous broadening of the electron spin transition. To achieve this high-fidelity, yet conditional implementation of the CPhase gate, we use optimal control based on the GRAPE-algorithm as explained in section 1.3.2. A possible control sequence is shown in fig. 4.5c, which was used for the creation of the GHZ state in section 4.4.

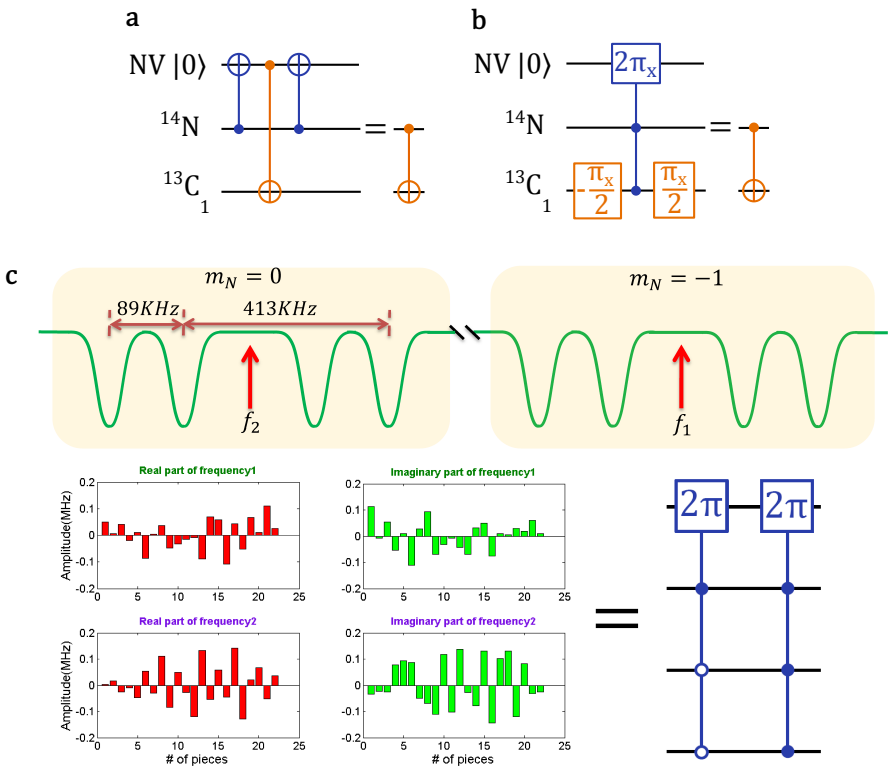

Figure 4.5.: Nuclear spin CNot gates. **a**, Scheme for non-local nuclear spin gates via the electron spin. **b**, Implementation by a nuclear CPhase gate, realized by a $2\pi_x$ rotation of the electron spin conditional on the nuclear spin states. **c**, Illustration of the robust implementation of the conditional 2π rotation on the electron spin, for the gate used in section 4.4 to generate the GHZ state, see fig. 4.6b. Upper part: Transition spectrum of the electron spin. Two mw frequencies f_1 and f_2 are applied to cover the full spectrum. Lower part: Control steps for both frequencies, each step is 1.46 μs long.

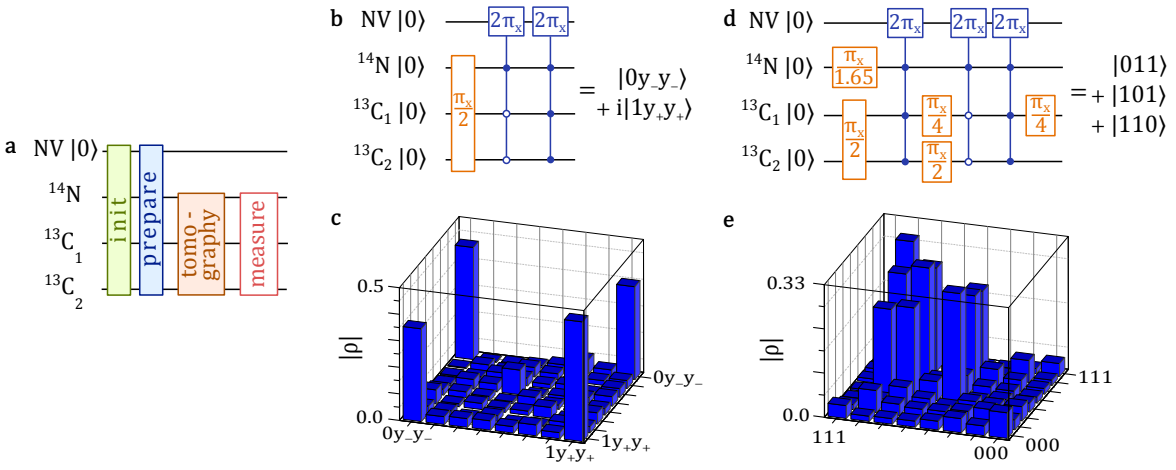

Figure 4.6.: Entanglement of nuclear spins. **a**, Schematic sequence for entanglement and state tomography. The initialization step is explained in fig. 4.3e. The preparation step is either sequence b for the GHZ state or d for the W state. The tomography and measurement steps are iterated over all measurement operators needed for tomography, as explained in appendix B.1. **b**, Pulse sequence for creating a GHZ-like state. **c**, Reconstructed density matrix of the GHZ state. **e**, Pulse sequence for creating a W state. **f**, Reconstructed density matrix of the W state.

4.4. Entanglement of three nuclear spins

Utilizing the techniques for initialization and readout as described in section 4.2 and for non-local nuclear spin gates as described in section 4.3, we can now create three-qubit entangled states of the nuclear spins, and perform state tomography. For three qubits, there are two types of maximally entangled states, which cannot be transformed into each other by only local gates. These two states are the so-called GHZ state (excluding normalization)

$$|\mathrm{GHZ}\rangle = |000\rangle + |111\rangle \tag{4.4}$$

and the W state

$$|\mathrm{W}\rangle = |001\rangle + |010\rangle + |100\rangle\,. \tag{4.5}$$

Fig. 4.6b,d shows the sequences that create these two types of states. Here, the GHZ like state $|0y_-y_-\rangle + |1y_+y_+\rangle$ is created, which differs from the GHZ state eq. (4.4) only by local rotations. After preparation, these states are then measured by state tomography, see appendix B.1. Fig. 4.6c,e shows the reconstructed density matrices. The fidelity $F = \langle\psi\,|\rho|\,\psi\rangle$ of the prepared state ρ can be estimated by correcting for the readout fidelity of ≈ 89 %, which yields $F = (88 \pm 1)\%$ for the GHZ state and $F = (85 \pm 3)\%$ for the W state. This fidelity is reduced by the fidelity of the robust 2π pulses (≈ 95 %), the T_1 decay of the electron spin ($\approx 96\%$) and initialization and post-selection fidelity ($\approx 97\%$).

In addition to state tomography, we also demonstrate violation of the Mermin inequal-

ity [149]. The Mermin inequality generalizes the inequalities devised by Bell [112] and Greenberger et. al. [116] to n-particle entanglement. These types of inequalities hold for any *local*, *realistic* theory [116], but are violated by quantum mechanics. Therefore, experimental violation of such an inequality is considered as proving genuine quantum entanglement. Note that for most implementations, loopholes have to be taken into account, e.g. the locality-loophole, as is the case here, or the detection loophole (in which case the fair sampling assumption has to be invoked). For the GHZ-like state shown in fig. 4.6b,c the corresponding Mermin inequality is (see appendix C)

$$|\langle\sigma_x\sigma_x\sigma_z\rangle + \langle\sigma_x\sigma_z\sigma_x\rangle + \langle\sigma_y\sigma_x\sigma_x\rangle - \langle\sigma_y\sigma_z\sigma_z\rangle| \leq 2. \tag{4.6}$$

The ideal quantum state shown in fig. 4.6b would violate this inequality and yield a value of 4. Here, we measured a value of 3.258 ± 0.014, clearly showing the non-classical nature of this state.

4.5. Quantum error correction

Here, we will experimentally implement three-qubit quantum error correction in the above presented nuclear spin register. QEC is a mile-stone experiment for systems that are supposed to be usable for QIP, due to the importance of QEC for scalable QIP (see section 1.1.2) and due to high experimental demands, thus demonstrating the achieved level of control [150, 151, 152, 153, 154, 71, 10]. Here, we demonstrate for the first time QEC in a solid state spin system. As bit-flip and phase-flip correction codes are essentially the same, here we only implement phase-flip error correction, because the rate of phase flips is usually the dominating one.

Historically, so-called syndrome measurements were introduced to enable QEC (see section 1.1.2), which detect if and which error happened by measuring in which subspace of the total Hilbert space the system is in. Once the error is known, it can easily be corrected by appropriate gates. Alternatively, the syndrome measurement can be replaced by an ancillary qubit, which has to be reset after each correction step. For our register, both these approaches are not possible. During the readout of the nuclear spins via the electron spin or the reset of the electron spin (as the ancillary qubit), the unknown dynamics of the electron spin will destroy nuclear spin coherence due to the hyperfine interaction. Therefore, we use a different approach, which was also implemented in cold ions [151] and SQUIDs [10]. This code is based on restoring the state of one qubit (here $^{13}C_2$), and transferring any errors onto the other two qubits (^{14}N and $^{13}C_1$). For repetitive QEC, which is not implemented here, the state of the other two qubits has to be reset after each correction step. This approach does not need measurements of ancillary qubits. Fig. 4.7 illustrates this correction scheme. First, the initial state $|\psi\rangle = \alpha|0\rangle + \beta|1\rangle$ of $^{13}C_2$ is encoded into a three-qubit state as $|^{14}N,^{13}C_1,^{13}C_2\rangle = \alpha|y_+y_+y_+\rangle + \beta|y_-y_-y_-\rangle$. Since we are only interested in the state of $^{13}C_2$ after the correction, we will, as an example, consider an error on this qubit. After

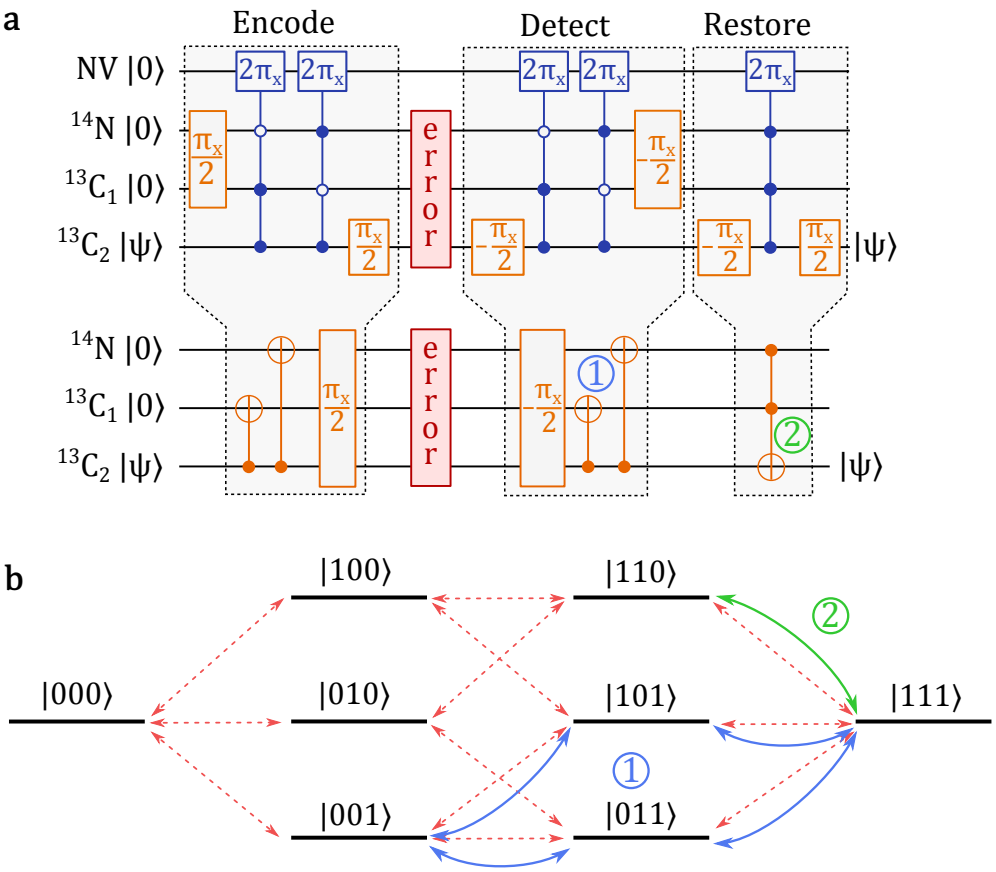

Figure 4.7.: QEC sequence. **a**, Implemented sequence for phase-flip QEC. Upper part: Actual pulse sequence in the experiment. Lower part: Effective operations within the nuclear register. Here, for the conditional gates a dot corresponds to the $|1\rangle$ state and a circle to the $|0\rangle$ state. **b**, Illustration of the detection and correction steps within the three-qubit register states. The chronological order of the two gates in step **1** is not relevant. Note that the gates in the detection step **1** are the same as used for the encoding.

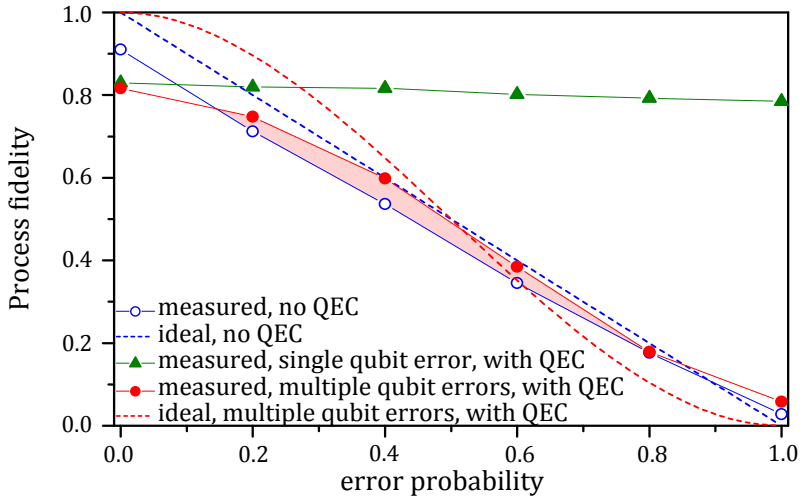

Figure 4.8.: QEC results. Measured process fidelity f of the QEC, depending on the error probability p. Green triangles are for the case where errors are only introduced on $^{13}C_2$. The blue dashed line is the ideal case (perfect measurements and gates) without error correction, $f(p) = 1 - p$, and the blue circles is for the experimental implementation. Likewise, the red dashed line is for the ideal case with QEC and with possible errors on all qubits (same probability), $f(p) = 1 - 3p^2 + 2p^3$, and the red circles are for the experimental implementation.

the decoding, the state will be $\alpha\,|000\rangle + \beta\,|111\rangle$ in case of no error and $\alpha\,|001\rangle + \beta\,|110\rangle$ in case of an error on $^{13}C_2$. The first step of the correction is to apply a conditional flip on ^{14}N and $^{13}C_1$ depending on $^{13}C_2$ being in state $|1\rangle$. Due to this step, errors of $^{13}C_2$ are detected by the other two qubits: If all three qubits are in the same state, i.e. $|000\rangle$ or $|111\rangle$, the final state of ^{14}N and $^{13}C_1$ will be $|00\rangle$, indicating that no error happened on $^{13}C_2$. On the other hand, if there was an error on $^{13}C_2$, the state is $|001\rangle$ or $|110\rangle$, and the final state of ^{14}N and $^{13}C_1$ will be $|11\rangle$, indicating this error. Thus, by applying a final conditional flip on $^{13}C_2$ if ^{14}N and $^{13}C_1$ are in state $|11\rangle$, the original state on $^{13}C_2$ is restored. These detection and correction gates are also illustrated in fig. 4.7b.

To demonstrate the implementation of this QEC code, we perform process tomography to determine the fidelity of the implemented process on $^{13}C_2$ with the ideal process, which is the unity operator $\mathbb{1}$, as described in appendix B.2. Controlled phase errors on a qubit are introduced by changing the phase of all pulses (gates) on this qubit after the error step. Fig. 4.8 shows the results of the experiment. The green triangles are the process fidelity of the implemented QEC, while errors only appear on $^{13}C_2$. Indeed, these single errors are faithfully corrected by the algorithm. The blue circles and the red dots are the process fidelity without QEC and with QEC, respectively. This comparison shows that for zero error probability, the process fidelity with QEC is reduced compared to the case without QEC due to the increased complexity of the measurement. However, for an error probability $>\approx 0.15$, the implementation of QEC is beneficial, as indicated by the red area in fig. 4.8.

4.6. Estimated number of strongly and weakly coupled nuclear spin

In the previous part of this chapter, we relied on strongly coupled nuclear spins for single shot readout, initialization and non-local control. Here, strongly coupled means that the hyperfine splitting is larger than the electron spin inhomogeneous broadening ($1/T_2^*$), such that the splitting is visible in the electron spin resonance spectrum, see fig. 4.3b. In this case, electron spin rotations conditional on the nuclear spin state can be implemented by frequency-selective mw pulses, see section 4.3. The (average) number of such nuclei close-by to an NV is limited, as increasing the concentration of ^{13}C within the diamond would also increase the linewidth of the electron spin transition, up to the point where contact interaction becomes dominant [155]. In addition to these strongly coupled nuclear spins, also weakly coupled spins can be addressed by the NV. Weakly coupled means that the hyperfine splitting is smaller than the electron spin inhomogeneous broadening ($1/T_2^*$), but larger than the electron spin homogeneous broadening ($1/T_2$). These nuclear spins can be addressed at low magnetic fields via the electron spin by applying dynamical decoupling [37, 156, 157, 158, 159].

Here, we will estimate the average number of suitable strongly and weakly coupled nuclear spins depending on the external magnetic field and the ^{13}C concentration, which is done by numerical simulations. To this end, we numerically calculate the volume within the diamond of suitable ^{13}C positions surrounding the NV. We assume only dipole-dipole hyperfine interaction, and ignore contact interaction, which means that the results are expected to be valid for hyperfine interactions below ~ 1 MHz. The first condition for a suitable ^{13}C nuclear spin is that the hyperfine splitting is larger than a certain threshold value, which is $1/T_2^*$ in the strong coupling case and $1/T_2$ for weak coupling. Note that for high-fidelity implementation of quantum algorithms, these thresholds, especially the $1/T_2$ limit, can usually not be fully exploited. The second condition roughly estimates if single shot readout of the nuclear spin is possible. For this, we require that the difference of the nuclear spin eigenbasis $\{|n_i\rangle\}$ with respect to the z-basis $\{|z_i\rangle\}$ is smaller than $1 - |\langle n_i|z_i\rangle|^2 < 0.25 \cdot 10^{-4}$. Due to this change of the nuclear spin eigenbasis depending on the electron spin state, the nuclear spin becomes projected into a new eigenbasis whenever the electron spin flips, which might destroy the nuclear spin state, see section 1.2.4. Our requirement means that the nuclear spin state will survive $\approx 4 \cdot 10^4$ electron spin flips, which corresponds to $\approx 4 \cdot 10^4$ readout steps, if one electron spin flip happens per readout step. The volume of suitable ^{13}C positions is obtained by numerical integration. For each volume element, we calculate the hyperfine splitting and the nuclear spin eigenbasis from the Hamiltonian of the electron plus nuclear spin system (see section 1.2.3), and mark this volume element as suitable if the two conditions described above are fulfilled.

Fig. 4.9a summarizes the results of this simulation. For strongly coupled nuclear spins, we can see that increasing the ^{13}C concentration to the natural value (brown dots) and

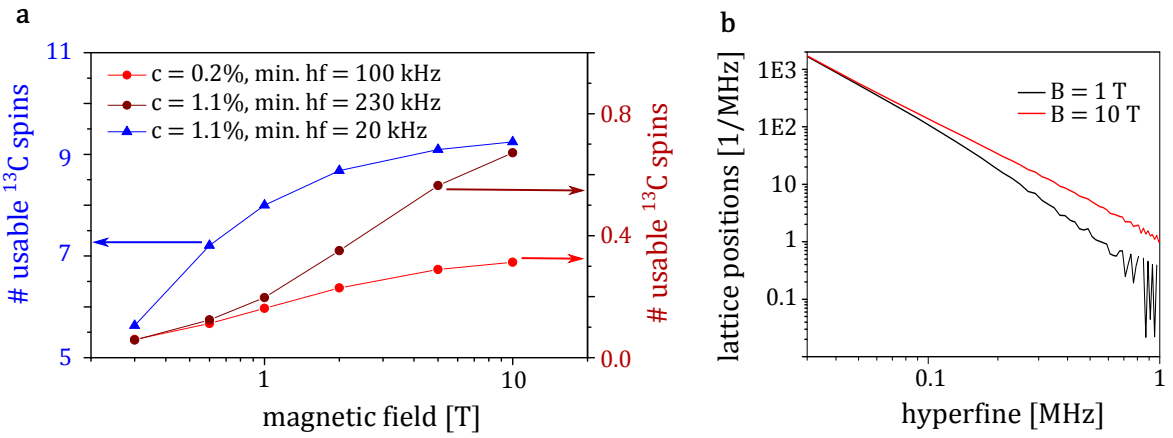

Figure 4.9.: Average number of suitable ^{13}C spins. **a**, Average number of suitable ^{13}C spins per NV for different ^{13}C concentrations c and different minimum hyperfine interaction. The red dots are for strongly coupled nuclei, and the blue triangles for including weakly coupled nuclei with at least 20 kHz hyperfine splitting. **b**, Spectral density of suitable lattice positions per NV for different magnetic fields B. The fluctuations at higher hyperfine interaction are due to numerical grain. Note that for these simulations, actual lattice positions are not taken into account.

increasing the magnetic field to 10 T increases the average number of suitable ^{13}C spins by around one order of magnitude compared to the current case (0.2 % ^{13}C concentration, red dots, 0.6 T). The blue triangles show the case where weakly coupled ^{13}C spins are included in the register. For a natural ^{13}C concentration $c = 1.1$ %, a T_2 time of 0.65 ms is possible [155], corresponding to a minimal hyperfine splitting of ≈ 1.5 kHz for an addressable ^{13}C , which, however, will not be usable for high-fidelity implementation of algorithms with several gates. By setting the minimal hyperfine splitting to > 20 kHz, we find that on average ≈ 10 ^{13}C spins per NV are usable. Note that for smaller hyperfine interaction, the density of suitable ^{13}C positions steeply increases, as can be seen in fig. 4.9b. For example, decreasing the minimal hyperfine splitting to > 10 kHz would yield ≈ 20 suitable ^{13}C , which would make spectral addressing of all these spins challening. Fig. 4.9b also illustrates that at a field of 1 T, nearly all ^{13}C positions with hyperfine splitting < 100 kHz are suitable, and increasing the field mainly affects the ^{13}C spins with stronger hyperfine interaction.

4.7. Detection of weakly coupled nuclear spins

In the previous section, we have seen that including weakly coupled nuclear spins can greatly increase the achievable size of the nuclear register. Here, we want to discuss and experimentally demonstrate how these weakly coupled spins can be addressed by the NV electron spin at high magnetic fields. So far, detection of weakly coupled nuclear spins with dynamical decoupling (DD) has been carried out at low magnetic fields [37,

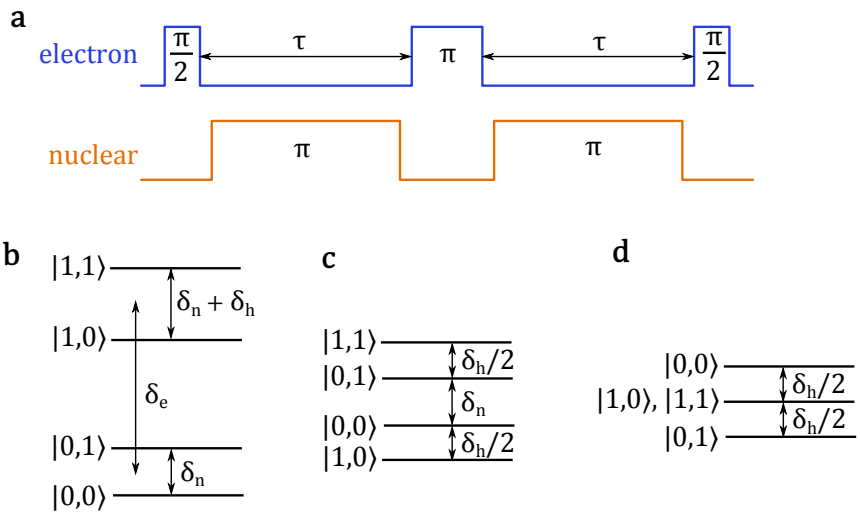

Figure 4.10.: ^{13}C detection via DD. a, DD sequence on electron and nuclear spin. Note that for technical reasons, a small time delay of ≈ 2 μs has to be introduced between electron and nuclear operations. **b**, Energy level scheme without rotating frame. δ_e is the energy splitting of the electron spin without hyperfine interaction (i.e. zero-field splitting plus electron Zeeman), δ_n is the nuclear Zeeman splitting, and δ_h the hyperfine splitting. **c**, Energy level scheme in the rotating frame of the electron spin. **d**, Energy level scheme in the rotating frame of the electron spin and of the nuclear spin in $m_s = -1$, which is used for the calculations.

156, 157, 158, 159]. In this case, the eigenbasis of the nuclear spins is mainly defined by the dipolar field of the electron spin at the position of the nucleus. In principle, DD removes the inhomogeneous dephasing of the electron spin by making the final coherent state independent of any static magnetic fields, generated by e.g. different states of the nuclear spin bath, see section 1.3.1. For previously demonstrated detection of weakly coupled nuclear spins [37, 156, 157, 158, 159], it is important that the eigenbasis of the nuclear spin (i.e. its quantization axis) depends on the electron spin state. Then, the change of the nuclear spin eigenbasis during coordinated flips of the electron spin will induce effective nuclear spin rotations due to precession within the new eigenbasis. During the DD, this effect will lead to changes of the nuclear spin state, such that the magnetic field generated by this nuclear spin will not be static, and influence the final state of the electron spin, if the timing of the DD is set appropriately [37].

However, for strong magnetic fields (larger than the hyperfine interaction), this effect is suppressed, as the nuclear spins eigenbasis will mainly be defined by the external field. Moreover, for single shot readout we even need that the eigenbasis of the nuclear spin does not change with the electron spin state. In this case, a technique similar to double electron-electron resonance can be applied. There, the state of the second spin (the nuclear spin in our case) is actively driven during the DD of the first spin (the NV electron spin). A difference is that in our case, the Rabi frequency of the nuclear

spin is usually smaller than the hyperfine interaction, such that all gates on the nuclear spin are selective to the electron spin state. The sequence for addressing these weakly coupled nuclear spins is shown in fig. 4.10a. To calculate the state evolution during this sequence, we go into the rotating frame of the electron spin and of the nuclear spin in the $m_s = -1$ state, see section 1.3. The effective energy level scheme is shown in fig. 4.10b. Note that due to inhomogeneous broadening, the electron spin driving field is always slightly off-resonant, however, this effect will be removed by DD, and is therefore ignored for the following considerations. We now calculate the possible evolution of the state $|e, n\rangle$ depending on the initial state of the nuclear spin, where e is the electron spin and n the nuclear spin. This is done in eq. (4.7) − eq. (4.11), where the first column is for nuclear spin state $|0\rangle$, the second column for state $|1\rangle$, and the last column without any nuclear spin, for reference. Eq. (4.7) is the state after the electron $\pi/2$ pulse. We set the states $|1,0\rangle$, $|1,1\rangle$ to zero energy such that only the states $|0,0\rangle$, $|0,1\rangle$ will accumulate phase (cf. fig. 4.10d). After the waiting time τ and the nuclear conditional π pulse the state is eq. (4.8). Then, the electron π pulse yields eq. (4.9). After the second waiting time τ and nuclear π pulse the state is eq. (4.10), which is re-written in eq. (4.11) for better readability.

$$|0,0\rangle - |1,0\rangle \qquad |0,1\rangle - |1,1\rangle \qquad |0\rangle - |1\rangle \tag{4.7}$$

$$e^{i\delta_h \tau/2}|0,0\rangle + |1,1\rangle \qquad e^{-i\delta_h \tau/2}|0,1\rangle - |1,0\rangle \qquad |0\rangle - |1\rangle \tag{4.8}$$

$$-e^{i\delta_h \tau/2}|1,0\rangle + |0,1\rangle \qquad -e^{-i\delta_h \tau/2}|1,1\rangle - |0,0\rangle \qquad -|1\rangle - |0\rangle \tag{4.9}$$

$$e^{i\delta_h \tau/2}|1,1\rangle + e^{-i\delta_h \tau/2}|0,1\rangle \qquad -e^{-i\delta_h \tau/2}|1,0\rangle - e^{i\delta_h \tau/2}|0,0\rangle \qquad -|1\rangle - |0\rangle \tag{4.10}$$

$$e^{i\delta_h \tau}|1,1\rangle + |0,1\rangle \qquad e^{-i\delta_h \tau}|1,0\rangle + |0,0\rangle \qquad |1\rangle + |0\rangle \tag{4.11}$$

The nuclear spin can be detected depending on the waiting time τ and the hyperfine splitting δ_h. If $\tau\delta_h = n\pi$, $n = 1, 3, 5, ...$, then the final state eq. (4.11) will be orthogonal to the case where no nuclear spin is present, independent on the initial state of the nuclear spin. The final electron $\pi/2$ pulse in 4.10a will then yield the electron spin state $|1\rangle$ instead of $|0\rangle$ for no nuclear spin, i.e. the presence of the nuclear spin is detected by the final state of the electron spin, which is demonstrated below experimentally. In addition, the initial state of the nuclear spin can be detected, i.e. implementation of a C_nNOT_e is possible. By setting the accumulated phase to $\tau\delta_h = n\pi/2$, $n = 1, 3, 5, ...$, the final state eq. (4.11) will be orthogonal for the two initial states of the nuclear spin (first two columns). The final electron $\pi/2$ pulse in 4.10a must then be applied with a $\pi/2$ phase shift, such that one initial state of the nuclear spin will yield the electron spin state $|0\rangle$, and the other initial nuclear spin will yield the electron spin state $|1\rangle$.

The experimental detection of weakly coupled nuclear spins is demonstrated on the same NV that was used for the previous measurements in this chapter. To measure a hyperfine spectrum of this NV, we have to sweep the parameters for the measurement sequence (fig. 4.10a), which are τ, the rf frequency and the rf power. The phase evolution

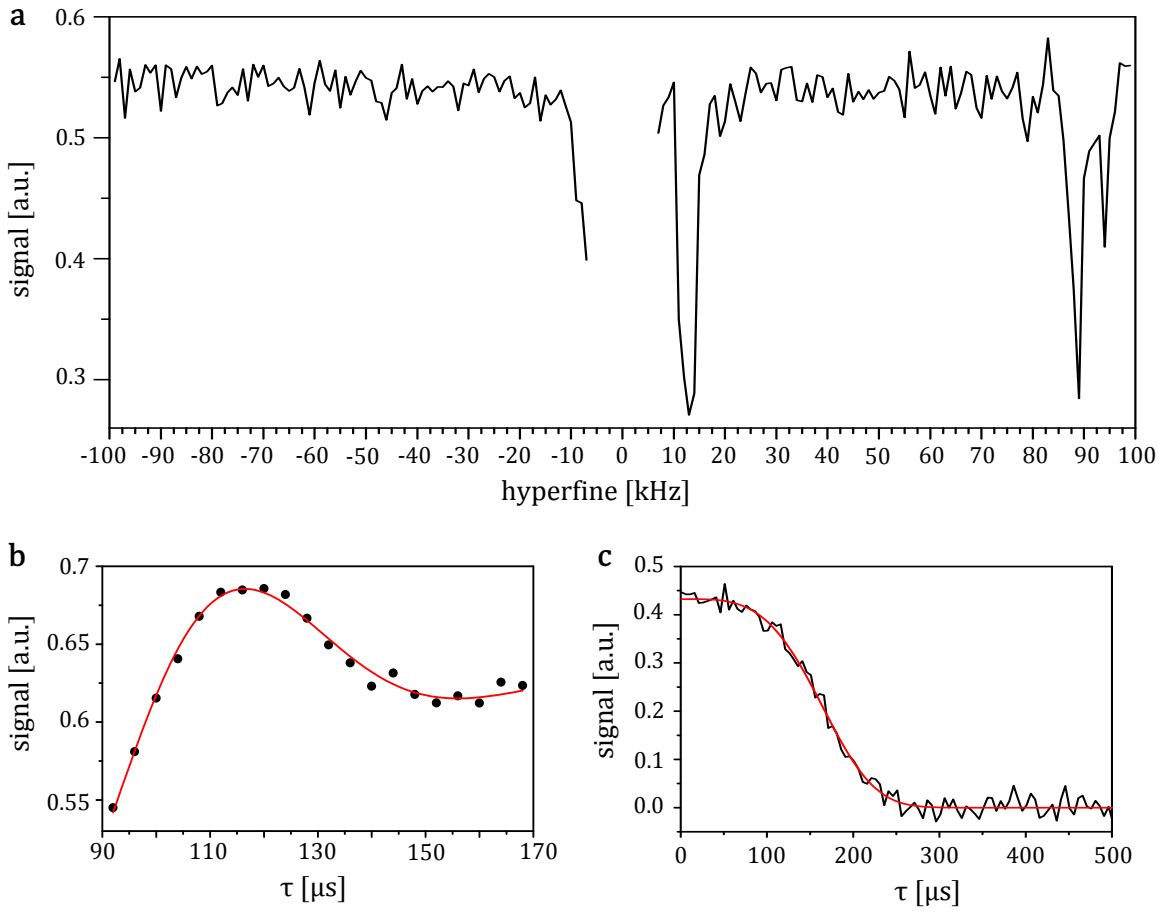

Figure 4.11.: Experimental ^{13}C detection via DD. All measurement shown here were performed with single shot readout of the ^{14}N nuclear spin, i.e. the final state of the electron spin was mapped onto the ^{14}N spin and then read out. **a**, Hyperfine spectrum of the NV. **b**, Measurement of the hyperfine splitting of a weakly coupled ^{13}C (12.3 kHz), see text for description. The damping of the oscillations is due to homogeneous dephasing of the electron spin. **c**, Hahn echo of the electron spin. Both the ^{14}N and $^{13}C_2$ (413 kHz hyperfine splitting) were initialized by single shot readout for this measurement, and the Rabi frequency of the electron spin was 1.88 MHz. The final $\pi/2$ pulse of the Hahn echo was performed once with phase 0 and once with phase π relative to the other pulses. The results of these two measurements were then subtracted. The fitting function is $A\exp(-(x/T_2)^p)$, with parameters $T_2 = 179$ μs, $p = 3.74$, $A = 0.43$.

time τ has to be set to $\tau\delta_h = n\pi$, $n = 1, 3, 5, ...$ Here, we chose n such that τ is as close as possible to 120 μs, which is slightly shorter than the T_2 time (see Hahn-echo in fig. 4.11c). Keeping τ roughly constant ensures that the spectrum is not obscured by varying decoherence effects. Furthermore, the rf has to be resonant to the nuclear spin and has to be adjusted by the current hyperfine splitting. Finally, the rf power (i.e. the Rabi frequency) has to be adjusted such that a π rotation is performed during time τ. The obtained spectrum is shown in fig. 4.11a. The ^{13}C spin at around 90 kHz is the one which was also visible in the ODMR spectrum of the NV ($^{13}C_2$), i.e. is strongly coupled. Additionally, we find another weakly coupled ^{13}C with hyperfine splitting of $\approx$ 13 kHz. Below 10 kHz, this measurement is hardly possible, due to the short electron $T_2 \approx 180$ μs. However, the spectrum does not look as 'smooth' as expected, e.g. the dip at 90 kHz is split into two unequal dips. This effect could be due the above described jumps of τ and of the rf power, but this would have to be examined in more detail. We can further analyse the weakly coupled ^{13}C . Therefore, the rf frequency, power and duration is set constant to induce a π rotation on this ^{13}C , and the time τ for the DD sequence is varied (note that τ must be longer than the rf duration). This measurement yields oscillations with a frequency corresponding to the hyperfine splitting, as shown in fig. 4.11b. The measured hyperfine splitting is 12.3 kHz.

4.8. Conclusions and outlook

In this chapter, we have experimentally demonstrated the capabilities of a hybrid electron-nuclear spin register based on the NV. The advantages of this hybrid register are fully exploiting by using the electron spin exclusively for control of the nuclear qubits (initialization, readout, selective and non-local gates), and the nuclear qubits as a long-lived quantum storage. Due to the achieved high-fidelity implementation of all control requirements, demonstration of quantum error correction was possible. For this work, we relied on strongly coupled nuclear spins, which limits the number of available nuclear spins, and also requires an NV with a specific nuclear spin environment. In addition to these strongly coupled nuclear spins, weakly coupled nuclear spins can greatly increase the size of the register, see section 4.6. We have seen that addressing of such nuclear spins is possible via dynamical decoupling of the electron spin, and provided first experimental demonstration in section 4.7.

For our implementation of QEC, errors were introduced artificially. In our case, the natural phase noise of the nuclear spins is generated by flips of the electron spin, which limits the coherence time of the nuclear spins to the $T_1 \approx 7$ ms time of the electron spin. Additionally, this means that the noise source of all three nuclear spins is the same. As soon as the electron spin flips, the nuclear spins decohere on the time scale of the hyperfine splitting, i.e. within several μs. Note that this effect does not lead to correlated errors (i.e. if qubit 1 is flipped qubit 2 will be flipped as well), but rather that after an electron spin flip, all coherences are lost, and the error probability of all qubits is 50 %,

which renders QEC non-applicable. It has been shown that the nuclear spin coherence can be protected by inducing fast dynamics on the electron spin (much faster than hyperfine splitting), such that the effective hyperfine interaction is suppressed (similar to motional averaging) [160]. By combining this technique with QEC, it could be possible to even extend the natural coherence time of the nuclear spins.

Another possible improvement is the implementation of repetitive QEC. The challenge there is to store the quantum information, while resetting the remaining part of the register, i.e. removing the entropy generated by the error. As the nuclear spins can be reset via the electron spin (see section 4.2), the task is to re-polarize the electron spin optically without destroying nuclear spin coherence. In our case, this was not possible because the hyperfine interaction was too strong. By carefully adjusting the laser power to avoid ionization of the NV, the optical polarization of the electron spin should be achievable within ~ 10 μs (cf. section 2.4). This means that the inverse hyperfine interaction (δ_h) must be much longer than the polarization time of the electron, i.e. $1/\delta_h \gg\approx 10$ μs, $\delta_h \ll 100$ kHz.

A. Rate equations

A.1. Steady state fluorescence of the NV with ionization

Here, we want to model the steady-state fluorescence of NV^-, depending on the illumination power. We will see that due to photo-ionization, the power and wavelength dependence of this steady-state fluorescence does not yield direct information of the NV^- intrinsic absorption cross-section, as would be the case without ionization. To this end, we use a four-level model, with NV^- ground state (G), excited state (E) and metastable state (M). For NV^0, we only take a single state (0) into account, as we are only interested in the state populations within NV^-. The model is illustrated in fig. A.1, and the corresponding rate equations are

$$\begin{aligned} \dot{p}_\mathrm{G} &= -I\sigma p_\mathrm{G} + \lambda_\mathrm{EG} p_\mathrm{E} + \lambda_\mathrm{MG} p_\mathrm{M} + r_\mathrm{re} p_0, \\ \dot{p}_\mathrm{E} &= I\sigma p_\mathrm{G} + (-\lambda_\mathrm{EG} - \lambda_\mathrm{EM} - I\sigma_\mathrm{ion}) p_\mathrm{E}, \\ \dot{p}_\mathrm{M} &= \lambda_\mathrm{EM} p_\mathrm{E} - \lambda_\mathrm{MG} p_\mathrm{M}, \\ \dot{p}_0 &= I\sigma_\mathrm{ion} p_\mathrm{E} - r_\mathrm{re} p_0, \end{aligned} \tag{A.1}$$

where p_i denotes the population of state i, λ_{ij} a decay rate from state i to state j, I the illumination intensity, σ the absorption cross-section of NV^-, and σ_ion the cross-section of ionization. The rate r_re is the effective recombination rate according to (2.3), which

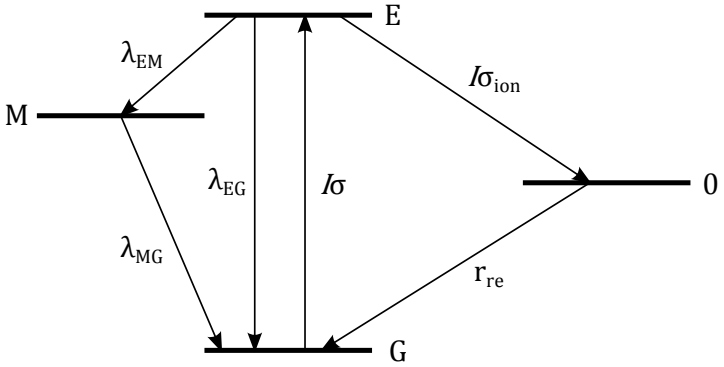

Figure A.1.: Four-level model of the NV.

is

$$r_{\mathrm{re}} = \sigma_{\mathrm{re}} I \frac{I}{I + I_0}, \tag{A.2}$$

where σ_{re} is an effective recombination cross-section, and I_0 is the saturation power of NV^0. The steady-state populations are obtained by setting all time derivatives in (A.1) to zero,

$$0 = \dot{p}_{\mathrm{G}} = \dot{p}_{\mathrm{E}} = \dot{p}_{\mathrm{M}} = \dot{p}_0, \tag{A.3}$$

and using

$$1 = p_{\mathrm{G}} + p_{\mathrm{E}} + p_{\mathrm{M}} + p_0. \tag{A.4}$$

Solving these equations for the excited state population p_{E} of NV^- yields

$$p_{\mathrm{E}} = p_S \frac{I}{I + I_S}, \tag{A.5}$$

where the saturation population p_S is

$$p_S = \frac{1}{1 + \lambda_{\mathrm{EM}}/\lambda_{\mathrm{MG}} + \sigma_{\mathrm{ion}}/\sigma_{\mathrm{re}} + \sigma_{\mathrm{ion}}/\sigma}, \tag{A.6}$$

and the saturation power I_S is

$$I_S = \frac{\lambda_{\mathrm{EG}} + \lambda_{\mathrm{EM}} + I_0 \sigma \sigma_{\mathrm{ion}}/\sigma_{\mathrm{re}}}{\sigma + \sigma \lambda_{\mathrm{EM}}/\lambda_{\mathrm{MG}} + \sigma_{\mathrm{ion}} + \sigma \sigma_{\mathrm{ion}}/\sigma_{\mathrm{re}}}. \tag{A.7}$$

As can be seen, not only the NV^- intrinsic absorption cross-section σ depends on the excitation wavelength, but also σ_{ion} and σ_{re}. Therefore, the time or ensemble averaged fluorescence of NV^- cannot be used to determine the wavelength dependence of σ, as changes of the other cross-sections will also influence the fluorescence.

A.2. Two-level rate equation for determination of ionization and recombination rates

Here, we calculate the relationship of the intrinsic rates of two-level linear rate equations with the measured state evolution, as obtained in section 2.3.3 for the charge state dynamics of the NV. The rate equations are

$$\begin{pmatrix} \dot{p}_{\mathrm{NV}^-} \\ \dot{p}_{\mathrm{NV}^0} \end{pmatrix} = \underbrace{\begin{pmatrix} -\lambda_{\mathrm{ion}} & \lambda_{\mathrm{re}} \\ \lambda_{\mathrm{ion}} & -\lambda_{\mathrm{re}} \end{pmatrix}}_{A} \cdot \underbrace{\begin{pmatrix} p_{\mathrm{NV}^-} \\ p_{\mathrm{NV}^0} \end{pmatrix}}_{p}, \tag{A.8}$$

where p_{NV^-}, p_{NV^0} are the populations of NV^- and NV^0, respectively, and λ_{ion}, λ_{re} are the rates for ionization (i.e. from NV^- to NV^0) and recombination (i.e. from NV^0 to NV^-), respectively. The time evolution of the population vector p is then given by

$$p(t) = e^{At} p(0), \tag{A.9}$$

which is solved by diagonalizing A. The starting point $p(0)$ is fixed by the result of the first charge state measurement, which is either $p(0) = \begin{pmatrix} 1 \\ 0 \end{pmatrix}$ (for NV^-) or $p(0) = \begin{pmatrix} 0 \\ 1 \end{pmatrix}$ (for NV^0). Then, the evolution of $p(t)$ can be calculated with the eigenvectors and eigenvalues of A, which yields

$$p_{-/0}(t) = \begin{pmatrix} \frac{\lambda_{re}}{\lambda_{ion}+\lambda_{re}} \\ \frac{\lambda_{ion}}{\lambda_{ion}+\lambda_{re}} \end{pmatrix} \pm \frac{\lambda_{0-/-0}}{\lambda_{ion}+\lambda_{re}} e^{-(\lambda_{ion}+\lambda_{re})t} \begin{pmatrix} -1 \\ 1 \end{pmatrix}, \tag{A.10}$$

where $p_{-/0}(t)$ is the evolution for the two initial states $NV^{-/0}$, respectively. These functions describe the measured charge state evolutions shown in fig. 2.11b. Fitting the functions to the measurement data yields the steady state population $p(\infty)$

$$p(\infty) = \begin{pmatrix} \frac{\lambda_{re}}{\lambda_{ion}+\lambda_{re}} \\ \frac{\lambda_{ion}}{\lambda_{ion}+\lambda_{re}} \end{pmatrix}, \tag{A.11}$$

and the decay rate r_{dec} into the steady state,

$$r_{dec} = \lambda_{ion} + \lambda_{re}. \tag{A.12}$$

With these two values, the ionization rate λ_{ion} and recombination rate λ_{re} can be calculated, see fig. 2.11c.

B. Tomography

B.1. State tomography

For state tomography, the density matrix ρ is expanded as

$$\rho = \sum_i a_i A_i, \tag{B.1}$$

where the A_i form a basis of mutually orthogonal operators. In the case of a single qubit, we would use the Pauli matrices $\mathbb{1}$, σ_x, σ_y, σ_z. For multiple qubits, the A_i are all combinations of the Pauli matrices for all qubits, i.e.

$$A_i = \left\{ \mathbb{1}^{(1)}\mathbb{1}^{(2)}...\mathbb{1}^{(n)}, \mathbb{1}^{(1)}\mathbb{1}^{(2)}...\sigma_x^{(n)}, ..., \sigma_z^{(1)}\sigma_z^{(2)}...\sigma_z^{(n)} \right\}, \tag{B.2}$$

where the superscripts indicates on which qubit the operator acts. The a_i in eq. (B.1) are given by the expectation value $\mathrm{Tr}\,(A_i\rho)$ of the corresponding operator [1]. These expectation values can be determined experimentally. Since only the expectation value of the σ_z operator can be measured directly, we apply $\pi/2$ rotations around the y and x axis of a spin to get the expectation values of σ_x and σ_y. Solving eq. (B.1) with the measured a_i yields the state of the system. Note that due to statistical measurement errors, the measured density matrix may not be positive semi-definite.

B.2. Process tomography

A general characterization of a quantum mechanical process $\mathcal{E}$ on a system is obtained by expanding the density matrix ρ into a basis of orthonormal states $|\psi_i\rangle$, and measuring the effect of the operator E_i of the process on each of these states:

$$\begin{aligned} \rho &= \sum_i p_i \left|\psi_i\right\rangle \left\langle\psi_i\right|, \\ \mathcal{E}(\rho) &= \sum_i E_i p_i \left|\psi_i\right\rangle \left\langle\psi_i\right| E_i^\dagger. \end{aligned} \tag{B.3}$$

The E_i can be measured by initializing the states $|\psi_i\rangle$ and performing state tomography after the process. Furthermore, we can do the expansion

$$E_i = \sum_m \chi_{im} A_m, \tag{B.4}$$

[1] Note that expectation value of the identity is fixed, as the sum of the diagonal elements of the density matrix ρ must be one, $\sum \rho_{ii} = 1$. E.g. for a qubit, the expectation value of the identity $\mathbb{1}$ is 0.5.

where the A_m form a basis of mutually orthogonal operators. Inserting eq. (B.4) into eq. (B.3) yields

$$\mathcal{E}(\rho) = \sum_{mn} \chi_{mn} A_m \rho A_n^\dagger, \tag{B.5}$$

where the $\chi_{mn} = \sum_i \chi_{im}\chi_{in}$ form the process matrix χ.

For the error correction, we only consider the effect of the process on the qubit that is carrying the information after the correction. Additionally, we are only interested in the fidelity F of the measured process and the ideal process χ_{id}, which is

$$F = \mathrm{Tr}(\chi_{\mathrm{id}}\chi). \tag{B.6}$$

Here, we chose the Pauli matrices $A_m = \{\mathbb{1}, \sigma_x, \sigma_y, \sigma_z\}$ as the operator basis. The ideal process for the error correction is the identity, and therefore $\chi_{11}^{\mathrm{id}} = 1$, and all other values being zero. The fidelity is then χ_{11}. Table B.1 shows the measurements we perform to obtain

$$\chi_{11} = \frac{1 + (r_{z,z} - r_{-z,z} + r_{x,x} - r_{-x,x} + r_{y,y} - r_{-y,y})}{4}, \tag{B.7}$$

by noting that $\chi_{11} + \chi_{22} + \chi_{33} + \chi_{44} = 1$.

Init	Measure	result
$\|z\rangle$	σ_z	$r_{z,z} = \chi_{11} + \chi_{14} + \chi_{41} + \chi_{44}$
$\|-z\rangle$	σ_z	$r_{-z,z} = -\chi_{11} + \chi_{14} + \chi_{41} - \chi_{44}$
$\|x\rangle$	σ_x	$r_{x,x} = \chi_{11} + \chi_{12} + \chi_{21} + \chi_{22}$
$\|-x\rangle$	σ_x	$r_{-x,x} = -\chi_{11} + \chi_{12} + \chi_{21} - \chi_{22}$
$\|y\rangle$	σ_y	$r_{y,y} = \chi_{11} + \chi_{13} + \chi_{31} + \chi_{33}$
$\|-y\rangle$	σ_y	$r_{-y,y} = -\chi_{11} + \chi_{13} + \chi_{31} - \chi_{33}$

Table B.1.: Measurement procedure and theoretical results for the process fidelity.

C. Mermin inequality

A first test for the non-deterministic and non-local structure of quantum mechanics was proposed by Bell in 1964 for the case of two entangled particles [112]. A general inequality to measure this behaviour of quantum mechanics for multiple particles was derived by Mermin [149]. For three particles, the inequality is

$$|\langle\sigma_x\sigma_x\sigma_y\rangle + \langle\sigma_x\sigma_y\sigma_x\rangle + \langle\sigma_y\sigma_x\sigma_x\rangle - \langle\sigma_y\sigma_y\sigma_y\rangle| \leq 2 \tag{C.1}$$

for any deterministic, local theory. However, the state

$$|\psi\rangle = \frac{1}{\sqrt{2}}(|000\rangle + i\,|111\rangle) \tag{C.2}$$

yields the value 4 for eq. (C.1). In our case, the prepared state is

$$|\psi\rangle = \frac{1}{\sqrt{2}}(|0\overline{y}\overline{y}\rangle + i\,|1yy\rangle), \tag{C.3}$$

where $|y\rangle = |0\rangle + i\,|1\rangle$ and $|\overline{y}\rangle = |0\rangle - i\,|1\rangle$. This state can be derived from eq. (C.2) by $\pi/2$ rotations around the x axis on qubit two and three. Thereby, σ_y in eq. (C.1) becomes σ_z for these two qubits, yielding the inequality

$$|\langle\sigma_x\sigma_x\sigma_z\rangle + \langle\sigma_x\sigma_z\sigma_x\rangle + \langle\sigma_y\sigma_x\sigma_x\rangle - \langle\sigma_y\sigma_z\sigma_z\rangle| \leq 2. \tag{C.4}$$

To measure the single terms, we transform each term to $\langle\mathbb{1}\mathbb{1}\sigma_z\rangle$. This can be achieved by a unitary operation U according to $\langle\psi\,|A|\,\psi\rangle = \langle\psi'\,|A'|\,\psi'\rangle$ for $|\psi'\rangle = U\,|\psi\rangle$ and $A' = UAU^\dagger$. The operations are shown in table C.1. The Cphase gate is described in

Measure	Operation
$\langle\sigma_x\sigma_x\sigma_z\rangle$	$\left(\frac{\pi}{2}\right)_{1,y}\left(\frac{\pi}{2}\right)_{2,y}\left(-\frac{\pi}{2}\right)_{3,y}(\text{CPhase})\left(\frac{\pi}{2}\right)_{3,y}$
$\langle\sigma_x\sigma_z\sigma_x\rangle$	$\left(\frac{\pi}{2}\right)_{1,y}(\text{CPhase})\left(\frac{\pi}{2}\right)_{3,y}$
$\langle\sigma_y\sigma_x\sigma_x\rangle$	$\left(\frac{\pi}{2}\right)_{1,x}\left(\frac{\pi}{2}\right)_{2,y}(\text{CPhase})\left(\frac{\pi}{2}\right)_{3,y}$
$\langle\sigma_y\sigma_z\sigma_z\rangle$	$\left(\frac{\pi}{2}\right)_{1,x}\left(-\frac{\pi}{2}\right)_{3,y}(\text{CPhase})\left(\frac{\pi}{2}\right)_{3,y}$

Table C.1.: Measurement procedure for the Mermin inequality.

section 4.3; here it is conditional on the states $|011\rangle$ and $|101\rangle$.

Acknowledgement

First of all, I want to thank Prof. Jörg Wrachtrup for giving me the opportunity and the support for doing my PhD thesis on the exciting topic of quantum information processing and nitrogen-vacancy defects in diamonds. I also thank Prof. Tilman Pfau for taking the time to evaluate this thesis and Prof. Hans Peter Büchler for chairing my PhD defense.

My two supervisors, Philipp Neumann and Prof. Fedor Jelezko contributed significantly to the success of my thesis. They provided important ideas and would always help me with technical, experimental and theoretical questions and challenges. For this support I am deeply thankful. I also thank Philipp for proof-reading this thesis.

I also thank all the people with whom I worked together at the institute and all around the world, namely Johannes Beck, Nabeel Aslam, Sebastian Zaiser, Mohammad Jamali, Matthias Nitsche, Adetunmise Dada, Susanna Huelga, Ressa Said, Jason Twamley, Junichi Isoya, Adam Gali, Thomas Schulte-Herbrüggen. Johannes Beck, who taught me a lot about the NV and the experimental setup, and who took part in the experiments on the initial mystery of NV^0 and on high dynamic range magnetometry. The work on high dynamic range magnetometry was also done in collaboration with Ressa Said and Jason Twamley, who designed and simulated the algorithm. Susanna Huelga provided helpful theoretical insight regarding temporal Bell inequalities. I had a great time working with Adetunmise Dada on distinguishing between non-orthogonal quantum states. Nabeel Aslam performed many of the tedious experiments for analyzing the charge state dynamics of the NV. Thomas Schulte-Herbrüggen invited us to Munich and explained us optimal control and its potential. For the error correction experiments I worked closely together with Ya Wang, who proposed and calculated the non-local gate operations and the tomography and error correction algorithms. Important steps for these experiments were the electron irradiation performed by Junichi Isoya and the creation a solid immersion lens by Mohammad Jamali.

Many people at the institute have helped me with various issues during my work. Most notably, I thank Petr Siyushev for help with dye lasers and optics, Helmut Fedder for help with Python programming, Florian Dolde and Ingmar Jacobi for help with the arbitrary waveform generator and microstructure generation, Stephan Hirschmann for help with many technical issues, and of course all the other people who supported me.

Special thanks go to my office colleagues Johannes Beck, Jan Honert, Nabeel Aslam and Sebastian Zaiser for interesting discussions not only related to physics. I also thank all the other members of the institute for a nice time during my PhD-thesis.

Finally, I want to thank my family. My beloved wife Ling Waldherr I thank for her

support and for always being there for me and for our sweet daughters Julia and Felina. I also thank my parents for supporting me and my family.

Bibliography

[1] D. Deutsch. *Quantum Theory, the Church-Turing Principle and the Universal Quantum Computer*. Proceedings of the Royal Society of London. A. Mathematical and Physical Sciences **400**(1818), 97–117 (August 1985). ISSN 1364-5021, 1471-2946.
URL http://dx.doi.org/10.1098/rspa.1985.0070

[2] P. W. Shor. *Polynomial-Time Algorithms for Prime Factorization and Discrete Logarithms on a Quantum Computer*. arXiv e-print quant-ph/9508027 (August 1995). SIAM J.Sci.Statist.Comput. 26 (1997) 1484.
URL http://arxiv.org/abs/quant-ph/9508027

[3] L. K. Grover. *A fast quantum mechanical algorithm for database search*. arXiv e-print quant-ph/9605043 (May 1996).
URL http://arxiv.org/abs/quant-ph/9605043

[4] R. P. Feynman. *Simulating physics with computers*. International Journal of Theoretical Physics **21**(6-7), 467–488 (June 1982). ISSN 0020-7748, 1572-9575.
URL http://dx.doi.org/10.1007/BF02650179

[5] N. Gisin, G. Ribordy, W. Tittel, and H. Zbinden. *Quantum cryptography*. Reviews of Modern Physics **74**(1), 145–195 (March 2002).
URL http://dx.doi.org/10.1103/RevModPhys.74.145

[6] E. Knill, R. Laflamme, and G. J. Milburn. *A scheme for efficient quantum computation with linear optics*. Nature **409**(6816), 46–52 (January 2001). ISSN 0028-0836.
URL http://dx.doi.org/10.1038/35051009

[7] A. Politi, J. C. F. Matthews, and J. L. O'Brien. *Shors Quantum Factoring Algorithm on a Photonic Chip*. Science **325**(5945), 1221–1221 (April 2009). ISSN 0036-8075, 1095-9203. PMID: 19729649.
URL http://dx.doi.org/10.1126/science.1173731

[8] R. Blatt and D. Wineland. *Entangled states of trapped atomic ions*. Nature **453**(7198), 1008–1015 (June 2008). ISSN 0028-0836.
URL http://dx.doi.org/10.1038/nature07125

[9] D. Cory, R. Laflamme, E. Knill, L. Viola, T. Havel, N. Boulant, G. Boutis, E. Fortunato, S. Lloyd, R. Martinez, C. Negrevergne, M. Pravia, Y. Sharf, G. Teklemariam, Y. Weinstein, and W. Zurek. *NMR Based Quantum Information Processing: Achievements and Prospects*. Fortschritte der Physik **48**(9-11), 875–907 (2000). ISSN 1521-3978.
URL http://dx.doi.org/10.1002/1521-3978(200009)48:9/11<875::AID-PROP875>3.0.CO;2-V

[10] M. D. Reed, L. DiCarlo, S. E. Nigg, L. Sun, L. Frunzio, S. M. Girvin, and R. J. Schoelkopf. *Realization of three-qubit quantum error correction with superconducting circuits*. Nature **482**(7385), 382–385 (February 2012). ISSN 0028-0836, 1476-4687.
URL http://dx.doi.org/10.1038/nature10786

[11] R. Hanson, L. P. Kouwenhoven, J. R. Petta, S. Tarucha, and L. M. K. Vandersypen. *Spins in few-electron quantum dots*. Reviews of Modern Physics **79**(4), 1217–1265 (October 2007).
URL http://dx.doi.org/10.1103/RevModPhys.79.1217

[12] B. E. Kane. *A silicon-based nuclear spin quantum computer*. Nature **393**(6681), 133–137 (May 1998). ISSN 0028-0836.
URL http://dx.doi.org/10.1038/30156

[13] J. Wrachtrup and F. Jelezko. *Processing quantum information in diamond*. Journal of Physics: Condensed Matter **18**(21), S807 (May 2006). ISSN 0953-8984.
URL http://dx.doi.org/10.1088/0953-8984/18/21/S08

[14] M. W. Doherty, N. B. Manson, P. Delaney, F. Jelezko, J. Wrachtrup, and L. C. Hollenberg. *The nitrogen-vacancy colour centre in diamond*. Physics Reports **528**(1), 1–45 (July 2013). ISSN 0370-1573.
URL http://dx.doi.org/10.1016/j.physrep.2013.02.001

[15] C. Kurtsiefer, S. Mayer, P. Zarda, and H. Weinfurter. *Stable Solid-State Source of Single Photons*. Physical Review Letters **85**(2), 290–293 (2000).
URL http://dx.doi.org/10.1103/PhysRevLett.85.290

[16] T. Babinec, B. Hausmann, M. Khan, Y. Zhang, J. Maze, P. Hemmer, and M. Loncar. *A diamond nanowire single-photon source*. Nature Nanotechnology **5**(3) (2010).
URL http://dx.doi.org/10.1038/nnano.2010.6

[17] F. Neugart, A. Zappe, F. Jelezko, C. Tietz, J. P. Boudou, A. Krueger, and J. Wrachtrup. *Dynamics of Diamond Nanoparticles in Solution and Cells*. Nano Letters **7**(12), 3588–3591 (December 2007). ISSN 1530-6984.
URL http://dx.doi.org/10.1021/nl0716303

[18] Y. Chang, H. Lee, K. Chen, C. Chang, D. Tsai, C. Fu, T. Lim, Y. Tzeng, C. Fang, C. Han, H. Chang, and W. Fann. *Mass production and dynamic imaging of fluorescent nanodiamonds*. Nature Nanotechnology **3**(5) (2008).
URL http://dx.doi.org/10.1038/nnano.2008.99

[19] J.-P. Boudou, P. Curmi, F. Jelezko, J. Wrachtrup, P. Aubert, M. Sennour, G. Balasubramanian, R. Reuter, A. Thorel, and E. Gaffet. *High yield fabrication of fluorescent nanodiamonds*. Nanotechnology **20**(23), 235602 (2009).
URL http://dx.doi.org/10.1088/0957-4484/20/23/235602

[20] A. Gruber, A. Drabenstedt, C. Tietz, L. Fleury, J. Wrachtrup, and C. von Borczyskowski. *Scanning Confocal Optical Microscopy and Magnetic Resonance on Single Defect Centers*. Science **276**(5321), 2012–2014 (June 1997). ISSN 1095-9203.
URL http://dx.doi.org/10.1126/science.276.5321.2012

[21] F. Jelezko, T. Gaebel, I. Popa, A. Gruber, and J. Wrachtrup. *Observation of coherent oscillations in a single electron spin*. Physical Review Letters **92**(7), 076401 (2004).
URL http://dx.doi.org/10.1103/PhysRevLett.92.076401

[22] G. Balasubramanian, P. Neumann, D. Twitchen, M. Markham, R. Kolesov, N. Mizuochi, J. Isoya, J. Achard, J. Beck, J. Tissler, V. Jacques, P. Hemmer, F. Jelezko, and J. Wrachtrup. *Ultralong spin coherence time in isotopically engineered diamond*. Nature Materials **8**(5) (2009).
URL http://dx.doi.org/10.1038/nmat2420

[23] J. Maze, P. Stanwix, J. Hodges, S. Hong, J. Taylor, P. Cappellaro, L. Jiang, M. Dutt, E. Togan, A. Zibrov, A. Yacoby, R. Walsworth, and M. Lukin. *Nanoscale magnetic sensing with an individual electronic spin in diamond*. Nature **455**(7213) (2008).
URL http://dx.doi.org/10.1038/nature07279

[24] J. Taylor, P. Cappellaro, L. Childress, L. Jiang, D. Budker, P. Hemmer, A. Yacoby, R. Walsworth, and M. Lukin. *High-sensitivity diamond magnetometer with nanoscale resolution*. Nature Physics **4**(10) (2008).
URL http://dx.doi.org/10.1038/nphys1075

[25] G. Balasubramanian, I. Chan, R. Kolesov, M. Al-Hmoud, J. Tisler, C. Shin, C. Kim, A. Wojcik, P. Hemmer, A. Krueger, T. Hanke, A. Leitenstorfer, R. Bratschitsch, F. Jelezko, and J. Wrachtrup. *Nanoscale imaging magnetometry with diamond spins under ambient conditions*. Nature **455**(7213) (2008).
URL http://dx.doi.org/10.1038/nature07278

[26] L. Hall, J. Cole, C. Hill, and L. Hollenberg. *Sensing of Fluctuating Nanoscale Magnetic Fields Using Nitrogen-Vacancy Centers in Diamond*. Physical Review Letters **103**, 220802 (2009).
URL http://dx.doi.org/10.1103/PhysRevLett.103.220802

[27] S. Steinert, F. Dolde, P. Neumann, A. Aird, B. Naydenov, G. Balasubramanian, F. Jelezko, and J. Wrachtrup. *High sensitivity magnetic imaging using an array of spins in diamond*. Review of Scientific Instruments **81**(4) (2010).
URL http://dx.doi.org/10.1063/1.3385689

[28] B. Grotz, J. Beck, P. Neumann, B. Naydenov, R. Reuter, F. Reinhard, F. Jelezko, J. Wrachtrup, D. Schweinfurth, B. Sarkar, and P. Hemmer. *Sensing external spins with nitrogen-vacancy diamond*. New Journal of Physics **13**(5), 055004 (2011).
URL http://dx.doi.org/10.1088/1367-2630/13/5/055004

[29] T. Staudacher, F. Shi, S. Pezzagna, J. Meijer, J. Du, C. A. Meriles, F. Reinhard, and J. Wrachtrup. *Nuclear Magnetic Resonance Spectroscopy on a (5-Nanometer)3 Sample Volume*. Science **339**(6119), 561–563 (January 2013). ISSN 0036-8075, 1095-9203. PMID: 23372009.
URL http://dx.doi.org/10.1126/science.1231675

[30] H. J. Mamin, M. Kim, M. H. Sherwood, C. T. Rettner, K. Ohno, D. D. Awschalom, and D. Rugar. *Nanoscale Nuclear Magnetic Resonance with a Nitrogen-Vacancy Spin Sensor*. Science **339**(6119), 557–560 (January 2013). ISSN 0036-8075, 1095-9203. PMID: 23372008.
URL http://dx.doi.org/10.1126/science.1231540

[31] F. Dolde, H. Fedder, M. Doherty, T. Nobauer, F. Rempp, G. Balasubramanian, T. Wolf, F. Reinhard, L. Hollenberg, F. Jelezko, and J. Wrachtrup. *Electric-field sensing using single diamond spins*. Nature Physics **7**(6) (2011).
URL http://dx.doi.org/10.1038/nphys1969

[32] V. M. Acosta, E. Bauch, M. P. Ledbetter, A. Waxman, L.-S. Bouchard, and D. Budker. *Temperature Dependence of the Nitrogen-Vacancy Magnetic Resonance in Diamond*. Physical Review Letters **104**(7), 070801 (February 2010).
URL http://dx.doi.org/10.1103/PhysRevLett.104.070801

[33] X.-D. Chen, C.-H. Dong, F.-W. Sun, C.-L. Zou, J.-M. Cui, Z.-F. Han, and G.-C. Guo. *Temperature dependent energy level shifts of nitrogen-vacancy centers in diamond*. Applied Physics Letters **99**(16), 161903–161903–3 (2011). ISSN 0003-6951.
URL http://dx.doi.org/10.1063/1.3652910

[34] G. Kucsko, P. C. Maurer, N. Y. Yao, M. Kubo, H. J. Noh, P. K. Lo, H. Park, and M. D. Lukin. *Nanometre-scale thermometry in a living cell*. Nature **500**(7460),

54–58 (August 2013). ISSN 0028-0836.
URL http://dx.doi.org/10.1038/nature12373

[35] P. Neumann, I. Jakobi, F. Dolde, C. Burk, R. Reuter, G. Waldherr, J. Honert, T. Wolf, A. Brunner, J. H. Shim, D. Suter, H. Sumiya, J. Isoya, and J. Wrachtrup. *High-Precision Nanoscale Temperature Sensing Using Single Defects in Diamond*. Nano Letters **13**(6), 2738–2742 (June 2013). ISSN 1530-6984.
URL http://dx.doi.org/10.1021/nl401216y

[36] F. Jelezko, T. Gaebel, I. Popa, M. Domhan, A. Gruber, and J. Wrachtrup. *Observation of coherent oscillation of a single nuclear spin and realization of a two-qubit conditional quantum gate*. Physical Review Letters **93**(13), 130501 (2004).
URL http://dx.doi.org/10.1103/PhysRevLett.93.130501

[37] L. Childress, M. Dutt, J. Taylor, A. Zibrov, F. Jelezko, J. Wrachtrup, P. Hemmer, and M. Lukin. *Coherent dynamics of coupled electron and nuclear spin qubits in diamond*. Science **314**(5797) (2006).
URL http://dx.doi.org/10.1126/science.1131871

[38] M. Dutt, L. Childress, L. Jiang, E. Togan, J. Maze, F. Jelezko, A. Zibrov, P. Hemmer, and M. Lukin. *Quantum register based on individual electronic and nuclear spin qubits in diamond*. Science **316**(5829) (2007).
URL http://dx.doi.org/10.1126/science.1139831

[39] L. Jiang, G. Dutt, E. Togan, L. Childress, P. Cappellaro, J. Taylor, and M. Lukin. *Coherence of an Optically Illuminated Single Nuclear Spin Qubit*. Physical Review Letters **100**(7), 073001 (2008).
URL http://dx.doi.org/10.1103/PhysRevLett.100.073001

[40] P. Neumann, N. Mizuochi, F. Rempp, P. Hemmer, H. Watanabe, S. Yamasaki, V. Jacques, T. Gaebel, F. Jelezko, and J. Wrachtrup. *Multipartite entanglement among single spins in diamond*. Science **320**(5881) (2008).
URL http://dx.doi.org/10.1126/science.1157233

[41] P. Neumann, J. Beck, M. Steiner, F. Rempp, H. Fedder, P. Hemmer, J. Wrachtrup, and F. Jelezko. *Single-Shot Readout of a Single Nuclear Spin*. Science **329**(5991) (2010).
URL http://dx.doi.org/10.1126/science.1189075

[42] A. Dreau, P. Spinicelli, J. R. Maze, J.-F. Roch, and V. Jacques. *Single-Shot Readout of Multiple Nuclear Spin Qubits in Diamond under Ambient Conditions*. Physical Review Letters **110**(6) (February 2013). ISSN 0031-9007, 1079-7114.
URL http://dx.doi.org/10.1103/PhysRevLett.110.060502

[43] G. Waldherr, J. Beck, M. Steiner, P. Neumann, A. Gali, T. Frauenheim, F. Jelezko, and J. Wrachtrup. *Dark States of Single Nitrogen-Vacancy Centers in Diamond Unraveled by Single Shot NMR*. Physical Review Letters **106**(15), 157601 (2011). URL http://dx.doi.org/10.1103/PhysRevLett.106.157601

[44] G. Waldherr, P. Neumann, S. Huelga, F. Jelezko, and J. Wrachtrup. *Violation of a Temporal Bell Inequality for Single Spins in a Diamond Defect Center*. Physical Review Letters **107**(9), 090401 (2011).
URL http://dx.doi.org/10.1103/PhysRevLett.107.090401

[45] G. Waldherr, J. Beck, P. Neumann, R. Said, M. Nitsche, Markham, D. Twitchen, J. Twamley, F. Jelezko, and J. Wrachtrup. *High Dynamic Range Magnetometry with a Single Nuclear Spin in Diamond*. Nature Nanotechnology **7**(2) (December 2011).
URL http://dx.doi.org/10.1038/nnano.2011.224

[46] G. Waldherr, A. C. Dada, P. Neumann, F. Jelezko, E. Andersson, and J. Wrachtrup. *Distinguishing between Nonorthogonal Quantum States of a Single Nuclear Spin*. Physical Review Letters **109**(18), 180501 (November 2012).
URL http://dx.doi.org/10.1103/PhysRevLett.109.180501

[47] N. Aslam, G. Waldherr, P. Neumann, F. Jelezko, and J. Wrachtrup. *Photo-induced ionization dynamics of the nitrogen vacancy defect in diamond investigated by single-shot charge state detection*. New Journal of Physics **15**(1), 013064 (January 2013). ISSN 1367-2630.
URL http://dx.doi.org/10.1088/1367-2630/15/1/013064

[48] G. Waldherr, Y. Wang, S. Zaiser, M. Jamali, T. Schulte-Herbrüggen, H. Abe, T. Ohshima, J. Isoya, J. F. Du, P. Neumann, and J. Wrachtrup. *Quantum error correction in a solid-state hybrid spin register*. Nature **506**(7487), 204–207 (February 2014). ISSN 0028-0836.
URL http://dx.doi.org/10.1038/nature12919

[49] F. Dolde, I. Jakobi, B. Naydenov, N. Zhao, S. Pezzagna, C. Trautmann, J. Meijer, P. Neumann, F. Jelezko, and J. Wrachtrup. *Room-temperature entanglement between single defect spins in diamond*. Nature Physics **9**(3), 139–143 (February 2013). ISSN 1745-2473, 1745-2481.
URL http://dx.doi.org/10.1038/nphys2545

[50] H. Bernien, B. Hensen, W. Pfaff, G. Koolstra, M. S. Blok, L. Robledo, T. H. Taminiau, M. Markham, D. J. Twitchen, L. Childress, and R. Hanson. *Heralded entanglement between solid-state qubits separated by three metres*. Nature **497**(7447), 86–90 (May 2013). ISSN 0028-0836.
URL http://dx.doi.org/10.1038/nature12016

[51] Y. Aharonov, D. Z. Albert, and L. Vaidman. *How the result of a measurement of a component of the spin of a spin-1/2 particle can turn out to be 100*. Physical review letters **60**(14), 1351–1354 (1988).
URL http://link.aps.org/doi/10.1103/PhysRevLett.60.1351

[52] N. W. M. Ritchie, J. G. Story, and R. G. Hulet. *Realization of a measurement of a "weak value"*. Physical review letters **66**(9), 1107–1110 (1991).
URL http://link.aps.org/doi/10.1103/PhysRevLett.66.1107

[53] J. J. L. Morton, A. M. Tyryshkin, R. M. Brown, S. Shankar, B. W. Lovett, A. Ardavan, T. Schenkel, E. E. Haller, J. W. Ager, and S. A. Lyon. *Solid-state quantum memory using the 31P nuclear spin*. Nature **455**(7216), 1085–1088 (October 2008). ISSN 0028-0836.
URL http://dx.doi.org/10.1038/nature07295

[54] J. J. Pla, K. Y. Tan, J. P. Dehollain, W. H. Lim, J. J. L. Morton, D. N. Jamieson, A. S. Dzurak, and A. Morello. *A single-atom electron spin qubit in silicon*. Nature **489**(7417), 541–545 (September 2012). ISSN 0028-0836.
URL http://dx.doi.org/10.1038/nature11449

[55] J. J. Pla, K. Y. Tan, J. P. Dehollain, W. H. Lim, J. J. L. Morton, F. A. Zwanenburg, D. N. Jamieson, A. S. Dzurak, and A. Morello. *High-fidelity readout and control of a nuclear spin qubit in silicon*. Nature **496**(7445), 334–338 (April 2013). ISSN 0028-0836.
URL http://dx.doi.org/10.1038/nature12011

[56] W. F. Koehl, B. B. Buckley, F. J. Heremans, G. Calusine, and D. D. Awschalom. *Room temperature coherent control of defect spin qubits in silicon carbide*. Nature **479**(7371), 84–87 (November 2011). ISSN 0028-0836.
URL http://dx.doi.org/10.1038/nature10562

[57] R. Kolesov, K. Xia, R. Reuter, R. Stöhr, A. Zappe, J. Meijer, P. R. Hemmer, and J. Wrachtrup. *Optical detection of a single rare-earth ion in a crystal*. Nature Communications **3**, 1029 (August 2012).
URL http://dx.doi.org/10.1038/ncomms2034

[58] C. Yin, M. Rancic, G. G. de Boo, N. Stavrias, J. C. McCallum, M. J. Sellars, and S. Rogge. *Optical addressing of an individual erbium ion in silicon*. Nature **497**(7447), 91–94 (May 2013). ISSN 0028-0836.
URL http://dx.doi.org/10.1038/nature12081

[59] T. Ladd, F. Jelezko, R. Laflamme, Y. Nakamura, C. Monroe, and J. O/'Brien. *Quantum computers*. Nature **464**(7285), 45–53 (March 2010). ISSN 0028-0836.
URL http://dx.doi.org/10.1038/nature08812

[60] M. A. Nielsen and I. L. Chuang. *Quantum Computation and Quantum Information*. Campridge University Press (2000).

[61] D. P. DiVincenzo. *Topics in Quantum Computers*. arXiv e-print cond-mat/9612126 (December 1996).
URL http://arxiv.org/abs/cond-mat/9612126

[62] S. J. Devitt, K. Nemoto, and W. J. Munro. *The idiots guide to quantum error correction*. arXiv preprint arXiv:0905.2794 (2009).
URL http://arxiv.org/abs/0905.2794

[63] A. Mizel, D. A. Lidar, and M. Mitchell. *Simple Proof of Equivalence between Adiabatic Quantum Computation and the Circuit Model*. Physical Review Letters **99**(7), 070502 (August 2007).
URL http://dx.doi.org/10.1103/PhysRevLett.99.070502

[64] R. Raussendorf and H. J. Briegel. *A One-Way Quantum Computer*. Physical Review Letters **86**(22), 5188–5191 (May 2001).
URL http://dx.doi.org/10.1103/PhysRevLett.86.5188

[65] P. W. Shor. *Fault-tolerant quantum computation*. In *Proc. 37th Symp. Foundations Comput.*, pages 56–65 (1996).
URL http://ieeexplore.ieee.org/xpls/abs_all.jsp?arnumber=548464

[66] D. P. DiVincenzo and P. W. Shor. *Fault-Tolerant Error Correction with Efficient Quantum Codes*. Physical Review Letters **77**(15), 3260–3263 (October 1996).
URL http://dx.doi.org/10.1103/PhysRevLett.77.3260

[67] D. Gottesman. *Theory of fault-tolerant quantum computation*. Physical Review A **57**(1), 127–137 (January 1998).
URL http://dx.doi.org/10.1103/PhysRevA.57.127

[68] E. Knill, R. Laflamme, and W. H. Zurek. *Resilient Quantum Computation*. Science **279**(5349), 342–345 (January 1998). ISSN 0036-8075, 1095-9203.
URL http://dx.doi.org/10.1126/science.279.5349.342

[69] E. Knill, R. Laflamme, and W. Zurek. *Threshold Accuracy for Quantum Computation*. arXiv:quant-ph/9610011 (October 1996).
URL http://arxiv.org/abs/quant-ph/9610011

[70] D. Aharonov and M. Ben-Or. *Fault-tolerant Quantum Computation with Constant Error*. In *Proceedings of the Twenty-ninth Annual ACM Symposium on Theory of Computing*, STOC '97, pages 176–188. ACM, New York, NY, USA (1997). ISBN 0-89791-888-6.
URL http://dx.doi.org/10.1145/258533.258579

[71] P. Schindler, J. T. Barreiro, T. Monz, V. Nebendahl, D. Nigg, M. Chwalla, M. Hennrich, and R. Blatt. *Experimental Repetitive Quantum Error Correction*. Science **332**(6033), 1059–1061 (May 2011). ISSN 0036-8075, 1095-9203.
URL http://dx.doi.org/10.1126/science.1203329

[72] G. Davies and M. F. Hamer. *Optical Studies of the 1.945 eV Vibronic Band in Diamond*. Proceedings of the Royal Society of London. A. Mathematical and Physical Sciences **348**(1653), 285–298 (February 1976). ISSN 1364-5021, 1471-2946.
URL http://dx.doi.org/10.1098/rspa.1976.0039

[73] J. Meijer, B. Burchard, M. Domhan, C. Wittmann, T. Gaebel, I. Popa, F. Jelezko, and J. Wrachtrup. *Generation of single color centers by focused nitrogen implantation*. Applied Physics Letters **87**(26), 261909 (December 2005).
URL http://dx.doi.org/10.1063/1.2103389

[74] J. Rabeau, P. Reichart, G. Tamanyan, D. Jamieson, S. Prawer, F. Jelezko, T. Gaebel, I. Popa, M. Domhan, and J. Wrachtrup. *Implantation of labelled single nitrogen vacancy centers in diamond using N-15*. Applied Physics Letters **88**(2), 023113 (2006).
URL http://dx.doi.org/10.1063/1.2158700

[75] J. Isberg, J. Hammersberg, E. Johansson, T. Wikstrom, D. J. Twitchen, A. J. Whitehead, S. E. Coe, and G. A. Scarsbrook. *High Carrier Mobility in Single-Crystal Plasma-Deposited Diamond*. Science **297**(5587), 1670–1672 (June 2002). ISSN 0036-8075, 1095-9203. PMID: 12215638.
URL http://dx.doi.org/10.1126/science.1074374

[76] M. Hauf, B. Grotz, B. Naydenov, M. Dankerl, S. Pezzagna, J. Meijer, F. Jelezko, J. Wrachtrup, M. Stutzmann, F. Reinhard, and J. Garrido. *Chemical control of the charge state of nitrogen-vacancy centers in diamond*. Physical Review B **83**, 081304 (2011).
URL http://dx.doi.org/10.1103/PhysRevB.83.081304

[77] M. W. Doherty, N. B. Manson, P. Delaney, and L. C. L. Hollenberg. *The negatively charged nitrogen-vacancy centre in diamond: the electronic solution*. New Journal of Physics **13**(2), 025019 (February 2011). ISSN 1367-2630.
URL http://dx.doi.org/10.1088/1367-2630/13/2/025019

[78] J. Maze, A. Gali, E. Togan, Y. Chu, A. Trifonov, E. Kaxiras, and M. Lukin. *Properties of nitrogen-vacancy centers in diamond: the group theoretic approach*. New Journal of Physics **13**(2), 025025 (2011).
URL http://dx.doi.org/10.1088/1367-2630/13/2/025025

[79] A. Batalov, C. Zierl, T. Gaebel, P. Neumann, I. Chan, G. Balasubramanian, P. Hemmer, F. Jelezko, and J. Wrachtrup. *Temporal coherence of photons emitted by single nitrogen-vacancy defect centers in diamond using optical Rabi-oscillations*. Physical Review Letters **100**(7), 077401 (2008).
URL http://dx.doi.org/10.1103/PhysRevLett.100.077401

[80] N. Manson, J. Harrison, and M. Sellars. *Nitrogen-vacancy center in diamond: Model of the electronic structure and associated dynamics*. Physical Review B **74**(10), 104303 (2006).
URL http://dx.doi.org/10.1103/PhysRevB.74.104303

[81] S. Felton, A. Edmonds, M. Newton, P. Martineau, D. Fisher, and D. Twitchen. *Electron paramagnetic resonance studies of the neutral nitrogen vacancy in diamond*. Physical Review B **77**, 081201 (2008).
URL http://dx.doi.org/10.1103/PhysRevB.77.081201

[82] L. Jiang, J. Hodges, J. Maze, P. Maurer, J. Taylor, D. Cory, P. Hemmer, R. Walsworth, A. Yacoby, A. Zibrov, and M. Lukin. *Repetitive Readout of a Single Electronic Spin via Quantum Logic with Nuclear Spin Ancillae*. Science **326** (2009).
URL http://dx.doi.org/10.1126/science.1176496

[83] N. Zarrabi, M. Dueser, R. Reuter, S. Dunn, J. Wrachtrup, and M. Boersch. *Detecting substeps in the rotary motors of FoF1-ATP synthase by Hidden Markov Models*. Proc. SPIE **6444**, 64440E (2007).
URL http://dx.doi.org/10.1117/12.701001

[84] C. Cohen-Tannoudji, B. Diu, and F. Laloe. *Quantum mechanics*. Wiley, New York (2005). ISBN 9780471569527 0471569526 9780471164333 047116433X 9780471164357 0471164356.

[85] A. Schweiger and G. Jeschke. *Principles of pulse electron paramagnetic resonance*. Oxford University Press, Oxford, UK; New York (2001). ISBN 0198506341 9780198506348.

[86] V. Dobrovitski, A. Feiguin, D. Awschalom, and R. Hanson. *Decoherence dynamics of a single spin versus spin ensemble*. Physical Review B **77**, 245212 (2008).
URL http://dx.doi.org/10.1103/PhysRevB.77.245212

[87] L. Viola, E. Knill, and S. Lloyd. *Dynamical Decoupling of Open Quantum Systems*. Physical Review Letters **82**(12), 2417–2421 (March 1999).
URL http://dx.doi.org/10.1103/PhysRevLett.82.2417

[88] G. S. Uhrig. *Keeping a Quantum Bit Alive by Optimized pi-Pulse Sequences*. Physical Review Letters **98**(10), 100504 (March 2007).
URL http://dx.doi.org/10.1103/PhysRevLett.98.100504

[89] G. de Lange, Z. Wang, D. Ristè, V. Dobrovitski, and R. Hanson. *Universal dynamical decoupling of a single solid-state spin from a spin bath.* Science **330**(6000) (2010).
URL http://dx.doi.org/10.1126/science.1192739

[90] J. Du, X. Rong, N. Zhao, Y. Wang, J. Yang, and R. B. Liu. *Preserving electron spin coherence in solids by optimal dynamical decoupling*. Nature **461**(7268), 1265–1268 (October 2009). ISSN 0028-0836.
URL http://dx.doi.org/10.1038/nature08470

[91] N. Khaneja, T. Reiss, C. Kehlet, T. Schulte-Herbruggen, and S. J. Glaser. *Optimal control of coupled spin dynamics: design of NMR pulse sequences by gradient ascent algorithms*. Journal of Magnetic Resonance **172**(2), 296–305 (February 2005). ISSN 1090-7807.
URL http://dx.doi.org/10.1016/j.jmr.2004.11.004

[92] S. Machnes, U. Sander, S. J. Glaser, P. de Fouquieres, A. Gruslys, S. Schirmer, and T. Schulte-Herbruggen. *Comparing, optimizing, and benchmarking quantum-control algorithms in a unifying programming framework*. Physical Review A **84**(2), 022305 (August 2011).
URL http://dx.doi.org/10.1103/PhysRevA.84.022305

[93] T. Caneva, T. Calarco, and S. Montangero. *Chopped random-basis quantum optimization*. Physical Review A **84**(2), 022326 (August 2011).
URL http://dx.doi.org/10.1103/PhysRevA.84.022326

[94] N. Manson and J. Harrison. *Photo-ionization of the nitrogen-vacancy center in diamond*. Diamond and Related Materials **14** (2005).
URL http://dx.doi.org/10.1016/j.diamond.2005.06.027

[95] K. Iakoubovskii, G. Adriaenssens, and M. Nesladek. *Photochromism of vacany-related centers in diamond*. Journal of Physics: Condensed Matter **12** (2000).
URL http://iopscience.iop.org/0953-8984/12/2/308/pdf/0953-8984_12_2_308.pdf

[96] I. Kupriyanov, V. Gusev, Y. Pal'yanov, and Y. Borzdov. *Photochromic effect in irradiated and annealed nearly IIa type synthetic diamond*. Journal of Physics: Condensed Matter **12** (2000).
URL http://iopscience.iop.org/0953-8984/12/35/318/pdf/0953-8984_12_35_318.pdf

[97] J. Steeds, S. Charles, J. Davies, and I. Griffin. *Photoluminescence microscopy of TEM irradiated diamond*. Diamond and Related Materials **9**(3-6), 397–403 (April 2000). ISSN 0925-9635.
URL http://dx.doi.org/10.1016/S0925-9635(99)00360-X

[98] T. Gaebel, M. Domhan, C. Wittmann, I. Popa, F. Jelezko, J. Rabeau, A. Greentree, S. Prawer, E. Trajkov, P. Hemmer, and J. Wrachtrup. *Photochromism in single nitrogen-vacancy defect in diamond*. Applied Physics B **82** (2006).
URL http://dx.doi.org/10.1007/s00340-005-2056-2

[99] K. Han, S. Kim, C. Eggeling, and S. Hell. *Metastable Dark States Enable Ground State Depletion Microscopy of Nitrogen Vacancy Centers in Diamond with Diffraction-Unlimited Resolution*. Nano Letters **10**(8) (2010).
URL http://dx.doi.org/10.1021/nl102156m

[100] R. Epstein, F. Mendoza, Y. Kato, and D. Awschalom. *Anisotropic interactions of a single spin and dark-spin spectroscopy in diamond*. Nature Physics **1**(2) (2005).
URL http://dx.doi.org/10.1038/nphys141

[101] S. Felton, A. Edmonds, M. Newton, P. Martineau, D. Fisher, D. Twitchen, and J. Baker. *Hyperfine interaction in the ground state of the negatively charged nitrogen vacancy center in diamond*. Physical Review B **79**(7), 075203 (2009).
URL http://dx.doi.org/10.1103/PhysRevB.79.075203

[102] G. Fuchs, V. Dobrovitski, R. Hanson, A. Batra, C. Weis, T. Schenkel, and D. Awschalom. *Excited-state spectroscopy using single spin manipulation in diamond*. Physical Review Letters **101**(11), 117601 (2008).
URL http://dx.doi.org/10.1103/PhysRevLett.101.117601

[103] K. Beha, A. Batalov, N. Manson, R. Bratschitsch, and A. Leitenstorfer. *Optimum Photoluminescence Excitation and Recharging Cycle of Single Nitrogen-Vacancy Centers in Ultrapure Diamond*. Physical Review Letters **109**, 097404 (2012).
URL http://dx.doi.org/10.1103/PhysRevLett.109.097404

[104] P. Siyushev, H. Pinto, M. Voros, A. Gali, F. Jelezko, and J. Wrachtrup. *Optically Controlled Switching of the Charge State of a Single Nitrogen-Vacancy Center in Diamond at Cryogenic Temperatures*. Physical Review Letters **110**(16), 167402 (April 2013).
URL http://dx.doi.org/10.1103/PhysRevLett.110.167402

[105] A. Draebenstedt, L. Fleury, C. Tietz, F. Jelezko, S. Kilin, A. Nizovtzev, and J. Wrachtrup. *Low-temperature microscopy and spectroscopy on single defect centers in diamond*. Physical Review B **60**(16), 11503–11508 (October 1999).
URL http://dx.doi.org/10.1103/PhysRevB.60.11503

[106] P. Delaney, J. C. Greer, and J. A. Larsson. *Spin-Polarization Mechanisms of the Nitrogen-Vacancy Center in Diamond.* Nano Letters **10**(2), 610–614 (February 2010). ISSN 1530-6984.
URL http://dx.doi.org/10.1021/nl903646p

[107] M. J. Rust, M. Bates, and X. Zhuang. *Sub-diffraction-limit imaging by stochastic optical reconstruction microscopy (STORM).* Nature Methods **3**(10), 793–796 (October 2006). ISSN 1548-7091.
URL http://dx.doi.org/10.1038/nmeth929

[108] E. Betzig, G. H. Patterson, R. Sougrat, O. W. Lindwasser, S. Olenych, J. S. Bonifacino, M. W. Davidson, J. Lippincott-Schwartz, and H. F. Hess. *Imaging Intracellular Fluorescent Proteins at Nanometer Resolution.* Science **313**(5793), 1642–1645 (September 2006). ISSN 0036-8075, 1095-9203. PMID: 16902090.
URL http://dx.doi.org/10.1126/science.1127344

[109] A. Beveratos, R. Brouri, J.-P. Poizat, and P. Grangier. *Bunching and antibunching from single NV color centers in diamond.* arXiv e-print quant-ph/0010044 (October 2000).
URL http://arxiv.org/abs/quant-ph/0010044

[110] R. Brouri, A. Beveratos, J.-P. Poizat, and P. Grangier. *Photon antibunching in the fluorescence of individual color centers in diamond.* Optics Letters **25**(17), 1294–1296 (September 2000).
URL http://dx.doi.org/10.1364/OL.25.001294

[111] A. Einstein, B. Podolsky, and N. Rosen. *Can Quantum-Mechanical Description of Physical Reality Be Considered Complete?* Physical Review **47**(10), 777–780 (May 1935).
URL http://dx.doi.org/10.1103/PhysRev.47.777

[112] J. S. Bell. *On the Einstein Podolsky Rosen Paradox.* Physics **I**, 195–200 (1964).

[113] E. Schroedinger. *Die gegenwaertige Situation in der Quantenmechanik.* Naturwissenschaften **23**(48), 807–812 (November 1935). ISSN 0028-1042, 1432-1904.
URL http://dx.doi.org/10.1007/BF01491891

[114] J. F. Clauser, M. A. Horne, A. Shimony, and R. A. Holt. *Proposed Experiment to Test Local Hidden-Variable Theories.* Physical Review Letters **23**(15), 880–884 (October 1969).
URL http://dx.doi.org/10.1103/PhysRevLett.23.880

[115] A. Aspect, P. Grangier, and G. Roger. *Experimental Realization of Einstein-Podolsky-Rosen-Bohm Gedankenexperiment: A New Violation of Bells Inequalities.* Physical Review Letters **49**(2), 91–94 (July 1982).
URL http://dx.doi.org/10.1103/PhysRevLett.49.91

[116] D. M. Greenberger, M. A. Horne, A. Shimony, and A. Zeilinger. *Bells theorem without inequalities.* American Journal of Physics **58**(12), 1131 (1990). ISSN 00029505.
URL http://dx.doi.org/10.1119/1.16243

[117] A. J. Leggett and A. Garg. *Quantum mechanics versus macroscopic realism: Is the flux there when nobody looks?* Physical Review Letters **54**(9), 857–860 (March 1985).
URL http://dx.doi.org/10.1103/PhysRevLett.54.857

[118] C. D. Tesche. *Can a noninvasive measurement of magnetic flux be performed with superconducting circuits?* Physical Review Letters **64**(20), 2358–2361 (May 1990).
URL http://dx.doi.org/10.1103/PhysRevLett.64.2358

[119] J. P. Paz and G. Mahler. *Proposed test for temporal Bell inequalities.* Physical Review Letters **71**(20), 3235–3239 (November 1993).
URL http://dx.doi.org/10.1103/PhysRevLett.71.3235

[120] S. F. Huelga, T. W. Marshall, and E. Santos. *Proposed test for realist theories using Rydberg atoms coupled to a high-Q resonator.* Physical Review A **52**(4), R2497–R2500 (October 1995).
URL http://dx.doi.org/10.1103/PhysRevA.52.R2497

[121] S. F. Huelga, T. W. Marshall, and E. Santos. *Temporal Bell-type inequalities for two-level Rydberg atoms coupled to a high-Q resonator.* Physical Review A **54**(3), 1798 (1996).
URL http://pra.aps.org/abstract/PRA/v54/i3/p1798_1

[122] F. De Zela. *Single-qubit tests of Bell-like inequalities.* Physical Review A **76**(4) (October 2007). ISSN 1050-2947, 1094-1622.
URL http://dx.doi.org/10.1103/PhysRevA.76.042119

[123] A. Palacios-Laloy, F. Mallet, F. Nguyen, P. Bertet, D. Vion, D. Esteve, and A. N. Korotkov. *Experimental violation of a Bells inequality in time with weak measurement.* Nature Physics **6**(6), 442–447 (April 2010). ISSN 1745-2473, 1745-2481.
URL http://dx.doi.org/10.1038/nphys1641

[124] M. E. Goggin, M. P. Almeida, M. Barbieri, B. P. Lanyon, J. L. O'Brien, A. G. White, and G. J. Pryde. *Violation of the Leggett-Garg inequality with weak measurements of photons.* Proceedings of the National Academy of Sciences **108**(4), 1256–1261 (January 2011). ISSN 0027-8424, 1091-6490.
URL http://dx.doi.org/10.1073/pnas.1005774108

[125] R. Ruskov, A. N. Korotkov, and A. Mizel. *Signatures of Quantum Behavior in Single-Qubit Weak Measurements.* Physical Review Letters **96**(20), 200404 (May

2006).
URL http://dx.doi.org/10.1103/PhysRevLett.96.200404

[126] C. Cohen-Tannoudji, B. Diu, and F. Laloe. *Quantum mechanics. 1 (1991) 1 (1991)*. Wiley [u.a.], New York [u.a.] (1991). ISBN 0471164321 9780471164326 047116433X 9780471164333 2705658335 9782705658335.

[127] S. M. Barnett and S. Croke. *Quantum state discrimination*. Advances in Optics and Photonics **1**(2), 238–278 (April 2009).
URL http://dx.doi.org/10.1364/AOP.1.000238

[128] C. H. Bennett. *Quantum cryptography using any two nonorthogonal states*. Physical Review Letters **68**(21), 3121–3124 (May 1992).
URL http://dx.doi.org/10.1103/PhysRevLett.68.3121

[129] S. J. van Enk. *Unambiguous state discrimination of coherent states with linear optics: Application to quantum cryptography*. Physical Review A **66**(4), 042313 (October 2002).
URL http://dx.doi.org/10.1103/PhysRevA.66.042313

[130] A. Delgado, L. Roa, J. C. Retamal, and C. Saavedra. *Entanglement swapping via quantum state discrimination*. Physical Review A **71**(1), 012303 (January 2005).
URL http://dx.doi.org/10.1103/PhysRevA.71.012303

[131] L. Roa, A. Delgado, and I. Fuentes-Guridi. *Optimal conclusive teleportation of quantum states*. Physical Review A **68**(2), 022310 (August 2003).
URL http://dx.doi.org/10.1103/PhysRevA.68.022310

[132] C. W. Helstrom. *Quantum detection and estimation theory*. Academic Press (January 1976). ISBN 0124110118.

[133] I. Ivanovic. *How to differentiate between non-orthogonal states*. Physics Letters A **123**(6), 257–259 (August 1987). ISSN 0375-9601.
URL http://dx.doi.org/10.1016/0375-9601(87)90222-2

[134] D. Dieks. *Overlap and distinguishability of quantum states*. Physics Letters A **126**(5-6), 303–306 (January 1988). ISSN 0375-9601.
URL http://dx.doi.org/10.1016/0375-9601(88)90840-7

[135] A. Peres. *How to differentiate between non-orthogonal states*. Physics Letters A **128**(1-2), 19 (March 1988). ISSN 0375-9601.
URL http://dx.doi.org/10.1016/0375-9601(88)91034-1

[136] S. Franke-Arnold, E. Andersson, S. M. Barnett, and S. Stenholm. *Generalized measurements of atomic qubits*. Physical Review A **63**(5), 052301 (April 2001).
URL http://dx.doi.org/10.1103/PhysRevA.63.052301

[137] M. Reck, A. Zeilinger, H. J. Bernstein, and P. Bertani. *Experimental realization of any discrete unitary operator*. Physical Review Letters **73**(1), 58–61 (July 1994). URL http://dx.doi.org/10.1103/PhysRevLett.73.58

[138] R. B. M. Clarke, A. Chefles, S. M. Barnett, and E. Riis. *Experimental demonstration of optimal unambiguous state discrimination*. Physical Review A **63**(4), 040305 (March 2001). URL http://dx.doi.org/10.1103/PhysRevA.63.040305

[139] A. C. Dada, E. Andersson, M. L. Jones, V. M. Kendon, and M. S. Everitt. *Quantum measurements of atoms using cavity QED*. Physical Review A **83**(4), 042339 (April 2011). URL http://dx.doi.org/10.1103/PhysRevA.83.042339

[140] N. M. Nusran, M. U. Momeen, and M. V. G. Dutt. *High-dynamic-range magnetometry with a single electronic spin in diamond*. Nature Nanotechnology **7**(2), 109–113 (February 2012). ISSN 1748-3387. URL http://dx.doi.org/10.1038/nnano.2011.225

[141] B. Higgins, D. Berry, S. Bartlett, H. Wiseman, and G. Pryde. *Entanglement-free heisenberg-limited phase estimation*. Nature **450**(7168), 393 (2007). URL http://dx.doi.org/10.1038/nature06257

[142] B. L. Higgins, D. W. Berry, S. D. Bartlett, M. W. Mitchell, H. M. Wiseman, and G. J. Pryde. *Demonstrating Heisenberg-limited unambiguous phase estimation without adaptive measurements*. New Journal of Physics **11**(7), 073023 (July 2009). ISSN 1367-2630. URL http://dx.doi.org/10.1088/1367-2630/11/7/073023

[143] D. W. Berry, B. L. Higgins, S. D. Bartlett, M. W. Mitchell, G. J. Pryde, and H. M. Wiseman. *How to perform the most accurate possible phase measurements*. Physical Review A **80**(5) (November 2009). ISSN 1050-2947, 1094-1622. URL http://dx.doi.org/10.1103/PhysRevA.80.052114

[144] R. Said, D. Berry, and J. Twamley. *Nanoscale magnetometry using a single-spin system in diamond*. Physical Review B **83**, 125410 (2011). URL http://dx.doi.org/10.1103/PhysRevB.83.125410

[145] T. Haeberle, D. Schmid-Lorch, K. Karrai, F. Reinhard, and J. Wrachtrup. *High-Dynamic-Range Imaging of Nanoscale Magnetic Fields Using Optimal Control of a Single Qubit*. Physical Review Letters **111**(17), 170801 (October 2013). URL http://dx.doi.org/10.1103/PhysRevLett.111.170801

[146] L. Robledo, L. Childress, H. Bernien, B. Hensen, P. Alkemade, and R. Hanson. *High-fidelity projective read-out of a solid-state spin quantum register*. Nature

477(7366), 574–578 (September 2011). ISSN 0028-0836.
URL http://dx.doi.org/10.1038/nature10401

[147] T. van der Sar, Z. H. Wang, M. S. Blok, H. Bernien, T. H. Taminiau, D. M. Toyli, D. A. Lidar, D. D. Awschalom, R. Hanson, and V. V. Dobrovitski. *Decoherence-protected quantum gates for a hybrid solid-state spin register*. Nature **484**(7392), 82–86 (April 2012). ISSN 0028-0836.
URL http://dx.doi.org/10.1038/nature10900

[148] V. Filidou, S. Simmons, S. D. Karlen, F. Giustino, H. L. Anderson, and J. J. L. Morton. *Ultrafast entangling gates between nuclear spins using photoexcited triplet states*. Nature Physics **8**(8), 596–600 (August 2012). ISSN 1745-2473.
URL http://dx.doi.org/10.1038/nphys2353

[149] N. D. Mermin. *Extreme quantum entanglement in a superposition of macroscopically distinct states*. Physical Review Letters **65**(15), 1838–1840 (October 1990). ISSN 0031-9007.
URL http://dx.doi.org/10.1103/PhysRevLett.65.1838

[150] D. G. Cory, M. D. Price, W. Maas, E. Knill, R. Laflamme, W. H. Zurek, T. F. Havel, and S. S. Somaroo. *Experimental quantum error correction*. Physical Review Letters **81**(10), 2152–2155 (1998).
URL http://link.aps.org/doi/10.1103/PhysRevLett.81.2152

[151] J. Chiaverini, D. Leibfried, T. Schaetz, M. D. Barrett, R. B. Blakestad, J. Britton, W. M. Itano, J. D. Jost, E. Knill, C. Langer, R. Ozeri, and D. J. Wineland. *Realization of quantum error correction*. Nature **432**(7017), 602–605 (December 2004). ISSN 0028-0836, 1476-4679.
URL http://dx.doi.org/10.1038/nature03074

[152] E. Knill, R. Laflamme, R. Martinez, and C. Negrevergne. *Benchmarking Quantum Computers: The Five-Qubit Error Correcting Code*. Physical Review Letters **86**(25), 5811–5814 (June 2001). ISSN 0031-9007, 1079-7114.
URL http://dx.doi.org/10.1103/PhysRevLett.86.5811

[153] N. Boulant, L. Viola, E. Fortunato, and D. Cory. *Experimental Implementation of a Concatenated Quantum Error-Correcting Code*. Physical Review Letters **94**(13) (April 2005). ISSN 0031-9007, 1079-7114.
URL http://dx.doi.org/10.1103/PhysRevLett.94.130501

[154] O. Moussa, J. Baugh, C. A. Ryan, and R. Laflamme. *Demonstration of Sufficient Control for Two Rounds of Quantum Error Correction in a Solid State Ensemble Quantum Information Processor*. Physical Review Letters **107**(16) (October 2011). ISSN 0031-9007, 1079-7114.
URL http://dx.doi.org/10.1103/PhysRevLett.107.160501

[155] N. Mizuochi, P. Neumann, F. Rempp, J. Beck, V. Jacques, P. Siyushev, K. Nakamura, D. J. Twitchen, H. Watanabe, S. Yamasaki, F. Jelezko, and J. Wrachtrup. *Coherence of single spins coupled to a nuclear spin bath of varying density*. Physical Review B **80**(4), 041201 (July 2009).
URL http://dx.doi.org/10.1103/PhysRevB.80.041201

[156] N. Zhao, J. Honert, B. Schmid, M. Klas, J. Isoya, M. Markham, D. Twitchen, F. Jelezko, R.-B. Liu, H. Fedder, and J. Wrachtrup. *Sensing single remote nuclear spins*. Nature Nanotechnology **7**(10), 657–662 (September 2012). ISSN 1748-3387, 1748-3395.
URL http://dx.doi.org/10.1038/nnano.2012.152

[157] T. Taminiau, J. Wagenaar, T. van der Sar, F. Jelezko, V. Dobrovitski, and R. Hanson. *Detection and Control of Individual Nuclear Spins Using a Weakly Coupled Electron Spin*. Physical Review Letters **109**, 137602 (2012).
URL http://dx.doi.org/10.1103/PhysRevLett.109.137602

[158] S. Kolkowitz, Q. Unterreithmeier, S. Bennett, and M. Lukin. *Sensing Distant Nuclear Spins with a Single Electron Spin*. Physical Review Letters **109**, 137601 (2012).
URL http://dx.doi.org/10.1103/PhysRevLett.109.137601

[159] T. H. Taminiau, J. Cramer, T. v. d. Sar, V. V. Dobrovitski, and R. Hanson. *Universal control and error correction in multi-qubit spin registers in diamond*. Nature Nanotechnology **advance online publication** (February 2014). ISSN 1748-3387.
URL http://dx.doi.org/10.1038/nnano.2014.2

[160] P. C. Maurer, G. Kucsko, C. Latta, L. Jiang, N. Y. Yao, S. D. Bennett, F. Pastawski, D. Hunger, N. Chisholm, M. Markham, D. J. Twitchen, J. I. Cirac, and M. D. Lukin. *Room-Temperature Quantum Bit Memory Exceeding One Second*. Science **336**(6086), 1283–1286 (August 2012). ISSN 0036-8075, 1095-9203. PMID: 22679092.
URL http://dx.doi.org/10.1126/science.1220513